Title
Laser Generated Shockwave Therapy of Bacterial Biofilms: From Benchtop to Pre-Clinical Studies

Author
Yao, William

Publication Date
2017

Peer reviewed|Thesis/dissertation

University of California
Los Angeles

Laser Generated Shockwave Therapy of Bacterial Biofilms: From Benchtop to Pre-Clinical Studies

A dissertation submitted in partial satisfaction
of the requirements for the degree
Doctor of Philosophy in Bioengineering

by

William Yao

2017

Abstract of the Dissertation

Laser Generated Shockwave Therapy of Bacterial Biofilms: From Benchtop to Pre-Clinical Studies

by

William Yao

Doctor of Philosophy in Bioengineering

University of California, Los Angeles, 2017

Professor Warren Grundfest, Chair

The presence of bacterial biofilms in wounds presents a major complication in wound treatments, significantly increasing morbidity and mortality. Biofilms delay wound healing, promote the growth of bacteria, and are a persistent source of pathogens that can infect other wounds. They are natively resistant to surfactants, antibiotics, and antiseptics, causing many current anti-bacterial treatments to remain ineffective at improving patient outcomes. Alternative methods for wound management often remove healthy tissue, along with the biofilm, resulting in unacceptable injuries to the patient. This work investigated a novel method of mechanically disrupting and removing persistent biofilms with laser generated shockwaves (LGS). We have demonstrated that LGS therapy can eliminate bacterial biofilms at energy levels well tolerated by tissue.

This study further developed practical and effective methods of delivering LGS in patients. We have developed a portable raster scanner, capable of delivering LGS at a rate of 5 shockwaves per second, with peak pressures of $> 200\,\mathrm{MPa}$, computer-aided targeting, and a treatment area of $4 \times 6\,\mathrm{cm}^2$. Using this system, we have demonstrated that LGS can remove 99.4% of biofilm matrix and 97.7% of surface CFUs.

This study also investigated the ability of LGS therapy to facilitate antibiotic delivery through biofilms. We have shown that LGS can increase the effectiveness of gentamicin by 21.4%, when used against *Staphylococcus epidermidis* biofilm grown *in vitro*, indicating

that LGS can help restore the effectiveness of treatments that were hindered by the presence of biofilms. When used against *S. epidermidis* biofilm grown on *ex vivo* tissue, LGS removed 69% of CFUs and caused a 52% reduction in biofilm coverage, without damaging the underlying tissue.

In bringing this technology forward, we have demonstrated that LGS is safe and well-tolerated when used on intact skin in rodents. When used at the maximal therapeutic window of 295.6 MPa, no hemorrhages nor damage to the dermis were seen after treatment. The only damage observed were minor injuries to the epidermis that resolve within three days. Preliminary followup results in rodents showed that these minor injuries cause no statistical differences in healing times between LGS-treated excisional wounds and controls.

The dissertation of William Yao is approved.

Daniel B. Ennis

Oscar M. Stafsudd

Maie A.R. St. John

Zachary Deis Taylor

Warren Grundfest, Committee Chair

University of California, Los Angeles

2017

To my family and fiancée ...

whose love and support helped get me

to where I am today

Table of Contents

List of Figures

List of Tables

Acknowledgments

First, I would like to express my sincere gratitude to my academic advisers and mentors: Professor Warren Grundfest and Zachary Taylor, for giving me the academic freedom and support to fully pursue my interests. You continued to always challenge me to work outside of my expertise and as a result, I have become a more well-rounded individual and academic.

I deeply thank my mentors, who have guided me through this project. Professor Stafsudd was instrumental in our understanding of laser generated shockwaves and helped guide us in our interferometry measurements and designs. Professors Ennis and Yang provided numerous inputs in the bacterial disruption project. Professor St. John has given critical feedback and criticism, as a medical scientist and clinician. Professor Fishbein was critical in our investigations on the safety of laser generated shockwaves in animal models.

I gratefully acknowledge the members of the bacterial disruption team. Dr. Nathan C Francis was my first graduate mentor and, more importantly, my close collaborator in many of the projects for bacterial disruption. In Chapter 3, equal effort was put in for the preparation of samples, imagining, and false coloring. We spent many long hours and headache, getting the false coloring finished. In Chapter 4, the raster scanner cart and scanning head was his brain child. In chapter 11, equal effort was put in for the animal work and data analysis. Dr. Edward Kuan has been a continuous support for much of the project. Your knowledge and contributions to grant and paper writing have been invaluable. I have also worked with many phenomenal undergraduate students throughout this project: Sam, Marian, Marisol, Valory, and Eric. I would not have been able to accomplish so much without your time and efforts.

I am fortunate to have worked with so many amazing researchers and students at the Center for Advanced Surgical and Interventional Technologies. George, Shijun, Ashkan, Neha, Jason, and Yong provided me with many advice on graduate work and life. I enjoyed our long conversations about our current gripes. Thank you for making graduate work so much more enjoyable.

All these years, there have been unwavering support from my friends: Nolan, Erica, Julie,

Henry, Noel, Yin Tao, Ke, Jia, Yi Chang, and many more.

I wish to dedicate this work to my mother, father, and brother. My parents came here to the U.S. as immigrants and worked hard to create an environment for my brother and I to learn and grow. While things were never easy, I am glad we were able to have made it to where we are today. My brother has been my constant companion in life, who stuck by me through thick and thin.

Finally, I also dedicate this work to my beautiful fiancée, Tiffany. Your love and support has been a constant pillar for me, and for that I am forever grateful. I cannot wait to spend my life with you.

Vita

2009–2012	Undergraduate Research Assistant, Allen F. Ryan Lab, University of California: San Diego, La Jolla, CA.
2012	Teaching Assistant, Division of Biological Sciences, University of California: San Diego. Cell Biology under direction of Dr. Douglass Forbes
2012	B.S. (Biology with Specialization in Bioinformatics), University of California: San Diego.
2012	Summer Research Intern, Shao-En Peng lab, National Museum of Marine Biology and Aquarium, Checheng Township, Pingtung County, Taiwan.
2014	M.S. (Bioengineering in Biomedical Instrumentation), UCLA.
2014–2015	Teaching Assistant, Life Science Department, UCLA. Introduction to Laboratory and Scientific Methodology under direction of Dr. Gaston Pfluegl.
2015–2016	Teaching Associate, Life Science Department, UCLA. Introduction to Laboratory and Scientific Methodology under direction of Dr. Gaston Pfluegl.
2016	Co-recipient of the 2016 American Society for Laser Medicine & Surgery, Inc, Outstanding Early Career Abstract Award.
2016	Teaching Associate, Bioengineering Department, UCLA. Basic Bioinstrumentation Circuits under direction of Dr. George Saddik and Bioengineering Capstone Design I under direction of Dr. Stephanie Seidlits.
2016	Recipient of the 2016 American Society for Laser Medicine & Surgery, Inc, Student Research Grant.
2017	Teaching Fellow, Bioengineering Department, UCLA. Bioengineering Capstone Design II under direction of Dr. Stephanie Seidlits, Basic Bioinstrumentation Circuits under direction of Dr. George Saddik, and Introduction to Bioengineering under direction of Dr. Zachary D. Taylor.

2013–2017 Graduate Student Researcher, Warren S. Grundfest Lab. Bioengineering Department, UCLA, Los Angeles, CA.

Publications

Yao W, Frie M, Pan J, et al. C-Jun N-terminal kinase (JNK) isoforms play differing roles in otitis media. BMC Immunology. 2014;15:46. doi:10.1186/s12865-014-0046-z.

Francis NC, Yao W, Grundfest WS, Taylor ZD. Laser generated shockwaves as a treatment to reduce bacterial load and disrupt biofilm. IEEE Trans Bio-Med Eng 2016.

Kuan, E. C., Yao, W., Francis, N. C.. Marton S., Banh M., Castellanos M., Banashek V., St. John M., Grundfest, W. S., and Taylor, Z. D. (2016), Laser generated shockwaves enhance antibacterial activity against biofilms in vitro. American Society of Laser Medicine and Surgery Annual Conference 2016. Lasers Surg. Med.. doi 10.1002/lsm.22485

Yao, W., Kuan, E. C., Francis, N. C., St. John, M. A., Grundfest, W. S. and Taylor, Z. D. (2017), Laser-generated shockwaves enhance antibacterial activity against biofilms in vitro. Lasers Surg. Med.. doi:10.1002/lsm.22627

Yao W, Francis NC, Kuan EC, et al. Safety of Laser Generated Shockwave Treatment of Cutaneous Bacterial Biofilms Infections. American Society of Laser Medicine and Surgery Annual Conference 2017. Lasers Surg. Med.. doi: 10.1002/lsm.22650

CHAPTER 1

Introduction

From the birth of the field of microbiology to current times, one of the main microbiology procedure has been culturing bacteria in a free-floating (planktonic) state, using high nutrient broth[1]. Many advances in the treatment of bacterial infections, with the most important being the discovery of antibiotics, have used planktonic cells as the model, due to the ease of the procedure[1]. However, in the last three decades, the field has come to recognize that bacteria are more commonly found in nature in an immobile, protected (biofilm) state [2] and can often be seen in diseases with chronic infections, such as pneumonia in cystic fibrosis patients, chronic wounds, and implant- and catheter-associated infections[3]. These biofilms allows normally antibiotic-susceptible bacteria to resist antibiotic and other chemical treatments.

Therefore, mechanical treatments may become a new standard methodology to treat biofilm-related infections in the future. Mechanical treatments work on the physical properties of bacteria and therefore can be non-specific and difficult for bacteria to develop resistance against. However, in order for mechanical treatments to become a standard treatment, it would need to give the selectivity of antibiotics, only eliminating bacteria cells and biofilm, while causing little to no harm to the patient. Laser generated shockwave (LGS) treatment has the potential as a novel therapy, due to its effectiveness of removing bacterial biofilm *in vitro*[4], while not damaging the structures of *ex vivo* porcine skin using similar energy levels[4, 5].

1.1 Motivation of Present Study

Preliminary work preformed by Narravo demonstrated that LGS can be used to measure the adhesion strength of bacterial biofilms and as a consequence may be used as a novel methodology for the removal of bacterial biofilm from infected wounds[4]. However, many more steps are required to transition this technology from a "proof-of-concept" to demonstrating efficacy of LGS in a pre-clinical setting, where the effects of LGS on skin tissue and bacterial cells and biofilm are understood. To accomplish this, more complex relationships involving LGS and bacterial biofilm will need to be investigated to understand the effects LGS may have in a clinical setting. This will include increasing the system's treatment areas to more closely match what is needed in a clinical setting, combinatory effects of LGS with standard antibiotic therapy, effectiveness of LGS against biofilm grown on organic substrates, and the effects of LGS against healthy skin tissue.

1.2 Objectives of Present Study

The objectives of this study were:

1. Investigate the effects of laser generated shockwaves (LGS) on the elimination of bacterial biofilm and bacterial cells off *ex vivo* pig skin and when combined with antibiotic therapy.

2. Translate LGS technology to pre-clinical studies through:

   (a) Development of a portable system capable of raster scanning the shockwave over the side of a small animal ($3\times5\,\mathrm{cm}^2$).

   (b) Tabulate the variations in LGS energies, due to inherent variabilities in a pre-clinical setup.

3. Investigate the safety of LGS in a small animal model.

1.3 Document Organization

To help the reader with the layout of this work, a summary of each chapter is provided below:

Chapter 2 will be dedicated to the understanding of biofilms and the background and theory behind laser generated shockwave (LGS) therapy.

Chapter 3 will verify the presence and removal of biofilm from *ex vivo* porcine skin tissue with LGS therapy.

Chapter 4 will cover the design of the portable raster scanner, which was needed to transition the LGS technology from a single-shot bench top system to a pre-clinical one capable of raster scanning the laser over a $4\times6\,\mathrm{cm}^2$ area.

Chapter 5 will investigate LGS as a combinatory therapy to gentamicin in an *in vitro* biofilm model and will also investigate in greater detail the effects of LGS therapy on the biofilm matrix.

Chapter 6 will tabulate how peak pressures generated with LGS changes in regards to different Nd:YAG laser spot sizes and how it decays through different thicknesses in ultrasound gel. Both are parameters that are expected to see an increase in variability when moving from a bench top system to a pre-clinical one.

Chapter 7 will follow up on the study presented in Chapter 5 and look at the effects of LGS and gentamicin against planktonic *S. epidermidis* cells.

Chapter 8 will look at how LGS affects *S. epidermidis* at the cellular level by investigating if LGS is capable of damaging and permeabilizing the bacterial cell walls and membranes.

Chapter 9 will present the findings on the safety of LGS treatment on healthy tissue in a rodent model and establish a therapeutic window for LGS therapy by establishing safe operating parameters.

Chapter 10 will cover the preliminary results on the efficacy of LGS therapy and topical gentamicin against *S. epidermidis* wound infections in a rodent model and the problem with a *S. epidermidis* biofilm wound model.

Chapter 11 will conclude this work with the final conclusions and recommendations for future topics.

CHAPTER 2

Background

2.1 Introduction

This chapter will provide the reader with the necessary background to understand the body of the work. It will start with an overview of bacterial biofilm and it's prevalence in the medical field. This chapter will then cover existing methodologies currently in research or in use to combat biofilm in a medical setting setting and will go over the benefits and drawbacks for each methodology. Finally, the chapter will end with a discussion of the history and background of laser generated shockwave (LGS) therapy as a novel tissue-sparing modality for the treatment of bacterial biofilms.

2.2 What are Biofilms?

The history of bacterial biofilm research is relatively young in the field of microbiology. For much of its history, microbiology research has predominately been focused on studying bacteria in their free-floating, i.e. planktonic, state, due to the ease of culturing and analysis. However, in the last three decades, the field has recognized that naturally occurring bacteria are most often found adhered to surfaces and surrounded by extra-cellular matrices that protect the bacteria from chemical and biological agents. This extra-cellular matrix is known as biofilm and is an adaptation by many species to adhere to surfaces and is an often observed behavior for bacteria in the wild[2, 6, 7, 8]. As the mechanism for adherence is non-specific, biofilms can be found on a wide array of surfaces: 1. household: sponges, dishrags, cutting boards, and fresh produce like tomatoes and carrots[9], 2. industrial: pipes and filters in water

treatment plants[10], and 3. medical: catheters, artificial heart valves, titanium implants, and biological tissues like cutaneous wounds[11].

Biofilms are comprised of complex, three-dimensional polysaccharide and protein matrices that provides a nurturing and protective microniche environment that allows for further proliferation of bacteria. They are composed of thick networks of polysaccharides and proteins[12, 13]. Once biofilm is established, it provides the bacteria resistance against antibiotic concentrations up to 100-1000 times the minimum inhibitory concentration (MIC), or the concentration needed to inhibit bacterial growth while suspended in solution [14, 2], and up to 500-5,000 times the minimum bactericidal concentration (MBC)[2], or the concentration to kill bacteria while suspended in solution. Several pathogenic bacterial genera, including Staphylococci and Pseudomonas, are known to be biofilm formers, and these organisms often develop resistance to antiseptics and antibiotics through the formation of biofilms[14, 15, 16, 17, 18].

Biofilms are formed in three main stages: 1. attachment, which can be subdivided into reversible and irreversible, 2. proliferation/growth, and 3. maturation and detachment. At the beginning of the first stage, the bacterium lands on the surface and reversibly binds with it. During this stage the bacterium walks along the surface, using its Type IV pili [19], until a favorable environment is found, such as an open wound. The bacterium then binds to the surface irrevesibly and begins to divide and proliferate. At this point no biofilm has been formed and the bacteria are still susceptible to antibiotics, as they were back in their planktonic state. During the second stage, the bacteria continue to proliferate and once they sense the bacterial population has reached sufficient levels, through a process called quorum-sensing, production of biofilm begins. In the final stage, the biofilm matures and thickens. The increase in thickness affects diffusion of nutrients and oxygen into the deeper parts of the biofilm[7]. This results in a gradient in available nutrients within the biofilm and causes stratification. At the outside edge of the biofilm, where nutrients and oxygen concentrations are the highest, the bacteria here are the most active and continue to proliferate. Some will detach from the biofilm and colonize new surfaces, starting the cycle anew[6]. On the other hand, deeper in the biofilm where nutrients and oxygen concentrations are low, the

bacteria are slower growing and some go into a dormant spore-like state. As slow-growing bacteria are less susceptible to antibiotics[20] and they extra protection from being deeper in the biofilm, this allows them to act like a reservoir of bacteria that can quickly re-establish the biofilm after duress. The combination of these three properties (1. protection against chemical and physical stresses, 2. ability to continuously release new bacteria to colonize new surfaces, and 3. ability to replenish bacteria within the biofilm), makes it extremely difficult to successfully eradicate an established biofilm. Therefore, often times the last resort is to replace the entire surface, which can be expensive and very painful, in the case where the surface is an open wound.

2.3 Biofilms in Cutaneous Wounds

One area of active research on biofilms and is the focus of this study is the improvement on treatments of bacterial biofilm infections in cutaneous wounds. The surface of the skin houses a wide variety of bacteria, while many are harmless, some are known opportunistic biofilm-forming pathogens: *Pseudomonas aeruginosa*, *Staphylococcus auerus*, and *Staphylococcus epidermidis*[21]. As the skin is an excellent barrier against these bacteria, they normally do not cause problems in normal healthy individuals. However, once the skin is compromised, in the case of a wound, these bacteria can readily colonize the wound bed. After hemostasis has been achieved, the wound bed will continue to leak wound exudate, which can contain: glucose, proteins, ions, and immune and bacterial cells[22]. This creates a nutrient rich and warm environment that is favorable for bacterial growth. If the body is unable able to quickly eliminate the invading bacteria, biofilm can form and cause a significant increase in wound healing times, as the biofilm hinders the body's immune cells' ability to reach the bacteria cells and hinders or prevents the diffusion of antibodies and antibiotics into the biofilm[23]. This is especially the case for individuals who have poor blood circulation, such as diabetic patients with peripheral artery disease or patients who develop bed sores or pressure sores, as the body already has a difficult time bringing immune cells to the injury site[24, 25].

One of the main purported contributors to persistence of chronically infected wounds is

the formation of bacterial biofilms. Chronically infected wounds are classified as wounds that remain open and incompletely healed longer than 6 weeks. These can be caused by a variety of etiologies (i.e., infectious, traumatic, inflammatory, iatrogenic)[26]. Due to prolonged morbidity and need for repeated therapy, such wounds impose a significant burden to the healthcare system worldwide [27]. For instance, it is estimated that $15.6 billion was spent on wound care in 2014 [28], of which $8.6 billion was spent on equipment for wound care in 2013 [29].

An important distinction needs to be made here between antibiotic resistance acquired from biofilm vs from phenotype. Antibiotic resistance acquired from biofilms works at the bacterial community level, as the mechanism of resistance usually relies on the slow-growth induced by the biofilm and/or physical/chemical structure of the biofilm matrix[30, 31]. The individual cells can still be sensitive to the antibiotic. Conversely, in the case of antibiotic resistance originating from the bacteria phenotype, the antibiotic is not effective at the individual cell level, as the cells have either modified the antibiotic target (lower affinity to the antibiotic) or produces inactivating enzymes that destroys the antibiotic, both have been observed as a mechanism for beta-lactam antibiotic resistance[32]. Therefore, when considering treatment for biofilm infections, it is also important to consider the treatment mechanism and types of resistance present. This is what makes Methillicin Resistant Staphylococcus Auerus (MRSA) so difficult to treat, as both mechanisms are in play.

This study will focus primarily on antibiotic resistance acquired from biofilm. The bacterial species used as the biofilm model for this work is *Staphylococcal Epidermidis* (*S. epidermidis*) (ATCC 35984). It is a Gram-positive cocci (spherical-shaped), coagulase-negative, organism that is part of the Staphylococcus genus that readily forms biofilm. Previously, it has been considered a harmless bacteria, as it is commonly found on human skin. However, recently it has been recognized as a opportunistic pathogen that causes nosocomial ("hopital-acquired") infections[33].

2.4 Existing Methodologies

Current methodologies to treat biofilm infections in cutaneous wounds can be divided into two broad categories: chemical and mechanical and the mechanisms for each can focus on either: 1. the elimination of the bacteria and/or biofilm, or 2. the improvement of the body's ability to fight the infection.

Chemical Methodologies

Chemical treatments are those that the uses the chemistry of bacterial cells and biofilm, either through polarity, affinity, or some other chemical/biochemical process, to eliminate or weaken the cells or biofilm. Chemical treatments, in particular antibiotics and antiseptics, are the most common wound care treatment methodology, especially in the initial stages of treatment, as they are generally the cheapest and easiest to use. These can include topical and systemic antibiotics[34, 35, 36], antiseptics, surfactants[37], and quorum-sensing-inhibitors[38, 39]. Systemic antibiotics delivers the drug throughout the body and are generally administered either orally or intravenously. System-wide administration of the antibiotic ensures that the entire wound receives the drug, even in the deep crevices, which is difficult in topical therapies. However, this method has some serious drawbacks, as the entire body is expose to the antibiotic serious side effects can occur, such as nephrotoxicity at high levels of gentamicin[40]. This limits the maximal dosage that can be safely administered and, as antibiotics already have a difficult time diffusing into biofilm, this reduces the final antibiotic concentration to sub-lethal levels once it reaches the bacteria cells. Topical antibiotics and antiseptics work by a similar mechanism, as they also focus on the elimination of the bacteria cells itself. However, these drugs are delivered topically and as a result is generally localized to the treatment area. Some diffusion of the drug into the patient circulatory system, but at a final blood serum levels are lower than systemic antibiotics[41]. This allows higher concentrations of antibiotics to be used. However, the trade off for higher localized concentrations is the loss of easily treating the entire wound, especially deep crevices. In general, antibiotic and antiseptic treatments are not effective at removing biofilm, as biofilms are adapted as

barriers of diffusion. Furthermore, they focus solely on the elimination of the bacterial cells, leaving the biofilm matrix intact, which may allow the pathogen to easily recolonize the wound.

The next two categories of chemical treatments, quorum-sensing inhibitors and surfactants, focus on addressing this issue of biofilm as a breeding site for future infections. For quorum-sensing inhibitors, these attack the bacterial communication system (quorum-sensing), preventing the formation of biofilm[42, 39]. As a result, the bacteria will remain susceptible to antibiotic treatment and gives the body's immune system more time to respond. However, the major limitation for these inhibitors is that they are more effective at the beginning of the infection, before mature biofilm has formed. On the other hand surfactants, such as ionic liquids[37], act as dispersants that dissolve/disperse mature biofilm. Due to the flexibility in the chemistry of ionic liquids, it may be possible design compounds that acts as a biofilm dispersant and a bactericide[37]. However, due to the heterogeneity within a biofilm and similarities between bacterial biofilm and tissue, the vast majority of ionic liquids are still considered as toxins according to the Globally Harmonized System of Classification and Labelling of Chemicals[37]. Therefore, more research is needed before this is technology can be safely and effectively used in a clinical setting.

Therapeutic Ultrasound Methodologies

Therapeutics based on ultrasound can be divided into two camps: low intensity and high intensity ultrasounds. In low intensity ultrasound (LIU) therapeutics uses acoustic intensities less than $500\,\mathrm{mW/cm^2}$. Studies have shown that these power densities causes non-thermal cellular effects, such as cavitation and microstreaming[43]. Cavitation occurs when microbubbles expand and contract due to changes in pressure from the acoustic waves, while microstreaming occurs when the pressure gradient causes localized fluid flow. These effects have been shown to cause angiogenesis[44], mast cell degranulation[45, 46], and increases in collagen deposition[47]. Furthermore, this increased fluid flow has been shown to improve the effects of aminoglycosides *in vivo*. Work by Rediske *et al.* shown an increased in gentamicin

activity against *Escherichia coli* biofilm in a rabbit model, albeit the energies needed to have this effect caused significant injuries to the animal[48]. While LIU can have many positive effects in wound healing, it has been shown, when used alone, to cause an increase in biofilm growth. Work by Pitt *et al.*, demonstrated that *Staphylococcus epidermidis*, *Pseudomonas aeruginosa* and *Escherichia coli* biofilms when exposed to low frequency ultrasound (70 kHz) at less than $2\,\mathrm{W/cm^2}$ resulted in increased growth rates of the cells [49]. This may be attributed to increased transportation of nutrients and oxygen to the cells and wastes away from the cells.

High intensity ultrasound (HIU), also referred as extracorporeal shock wave therapy (ESWT), uses strong acoustic waves to mechanically disrupt the biofilm from the surface of the wound. The acoustic pressure needed to achieve this achieve this effect are up to 100 MPa in peak compressive stress and $5 - 10\,\mathrm{MPa}$ in peak tensile stress. Work by Kuo *et al.* showed that ESWT can have a positive effect in accelerating healing of slow healing wounds in streptozotocin-induced diabetic rats. In their study, the rodents were treated up to three ESWT sessions, with each session comprising of 800 impulses at $0.09\,\mathrm{mJ/mm^2}$. The animals treated with ESWT showed an increase in wound healing rates, cellular proliferation, and angiogenesis and a decrease in inflammatory response[50]. However bacterial biofilm was not studied in this work, so it remains to be seen if this technology can be used treat biofilm infected wounds. Many studies have demonstrated that ESWT is effective in removing bacterial biofilms from hard surfaces, such as from enamel to treat periodontitis[51], and implants[52, 53]. However one of the limitations of ESWT that has prevented it from treating bacterial biofilm wounds, is the generation of cavitation bubbles due to the large tensile stress, which is needed to remove biofilm. These cavitation bubbles have been shown to cause significant damage to tissue[54, 55, 56].

Debridement

Debridement is the removal of necrotic and devitalised tissue from the wound bed. This can be accomplished in a variety of ways: enzymatic[57], autolytic[58], and with maggots[59].

However the ones, that will be focused on are surgical, or also known as sharps, debridement and wet to dry debridement. Both are mechanical methods that can quickly and effectively remove necrotic tissue [60], however both carry high risk of damaging underlying normal tissue. In the case of surgical debridement, the use of sharp instruments, such as scapels and scissors, are used to remove devitalized tissue. This allows quick and effective removal of bacterial biofilm and impaired tissue. However, there is inadvertent removal of viable tissue, as there is a lack of biological/molecular marker that can objectively differentiate between healthy and impaired tissue[61] to define extend of tissue removal. This usually results in removal of healthy tissue and poor pain tolerance from the patient[62].

In the case of wet to dry debridement involves packing the wound with wet gauze. As the dressing dries, it pulls wound exudate and bacteria into the dressing, removing it from the wound. Furthermore, during the drying process the dressing adheres to the underlying tissue. When the dried dressing is removed from the wound, the adhered tissue is also removed in the process. However, as the dressing is not selective in the tissue it adheres to, it is inadvertent that healthy and newly formed tissue can be removed in the process. Thus causing patient pain and damage to the tissue[63]. Furthermore, as evaporation causes colding of the wound, often up to 10 °C lower than surrounding tissue[64], this leads to vasoconstriction, in a time where increased blood flow is desired.

2.5 Laser Generated Shockwave (LGS)

The technology presented in this work for the treatment of bacterial biofilms in wounds is laser generated shockwave (LGS) therapy. LGS is analogous to extracorporeal shock waves generated with a lithotriptors. Both shockwave profile exhibit short rise times (< 10 ns) and high peak pressures (MPa). However, the key difference between the two is the lack of a tensile component in laser generated shockwaves, fig. 2.1. As tensile waves have been demonstrated to cause significant vascular damage and other soft tissue damage [65, 66], LGS therapy is hypothesized to be better tolerated by the tissue than EWST.

The design for the laser generated shockwave technology, described in fig. 2.2, was de-

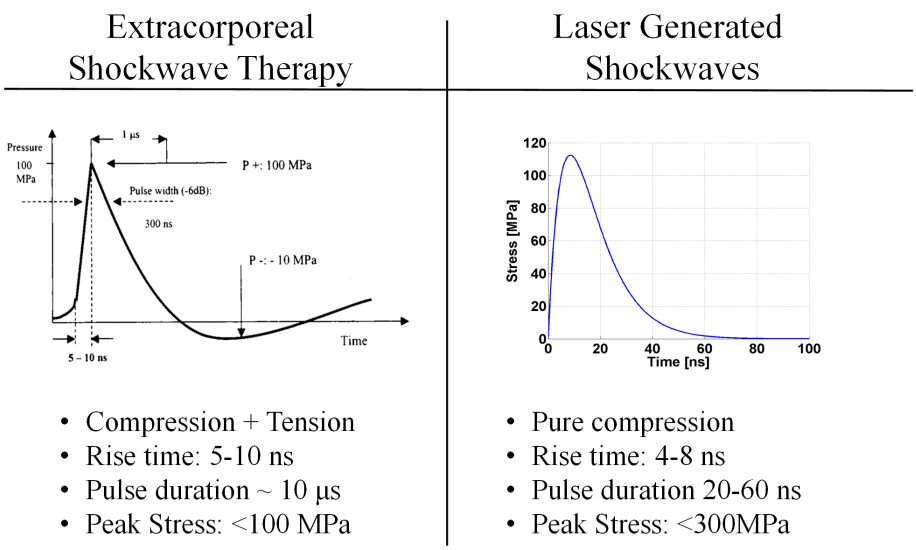

Figure 2.1: Comparison between extracorporeal shockwave and laser generated shockwave acoustic profiles. Adapted from Navarro [4].

veloped in a collaboration between Drs. Vijay Gupta and Warren S. Grundfest, and is first described in Navarro's work[4]. This was a modification in the previous laser spallation technique, first developed by Gupta, to measure tensile strength of thin film interfaces (paints, multilayer electronics, etc), through precise laser generated stress wave profiles[67, 68, 69, 70, 71]. The main purpose of the technology was to investigate interficial strengths of engineering systems, involving metal and polymeric coatings on metal, plastics, and ceramic substrates. To accomplish this, a test substrate composed of the substrate disc with a film, in question, coating one of the disc. On the other side is a 0.5 µm aluminum (Al) film sandwiched between the substrate and $\sim$ 100 µm waterglass (SiO_2) film. A shockwave is then generated through 1064 nm Nd:YAG laser ablation of the aluminum, causing a rapid expansion of the confined Al. This generates a compressive shock wave that travels through the substrate and reflects off the coating's free surface, as a tensile wave, causing spallation of the film. In the design for the use of laser generated shockwaves against bacterial biofilm, a metal film (0.5 µm titanium Ti) is similarly Nd:YAG laser ablated, while under confinement of a supportive substrate and the waterglass. The key difference is the biofilm here lies on top of the wound and not the LGS substrate. A coupling gel is used to carry the shockwave generated from LGS substrate to the biofilm. When the shockwave reaches the

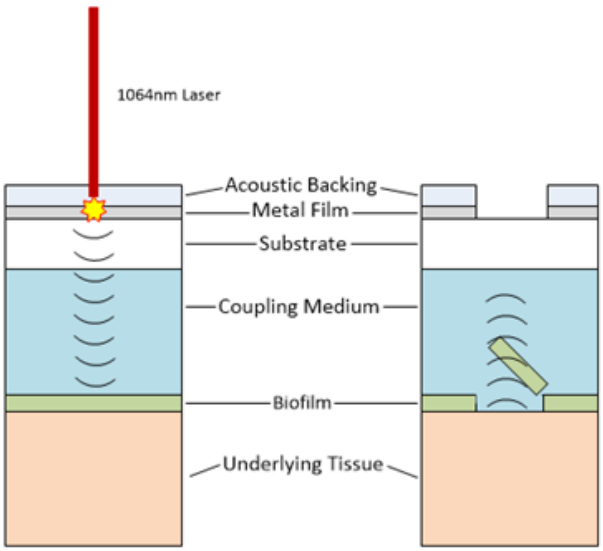

Figure 2.2: Diagram of generation of LGS for bacterial biofilm removal from a wound. Left: LGS generating substrate, composed of a thin metal film sandwich between an acoustic backing layer and a supportive substrate. A short 1064 nm Nd:YAG pulse is used to ablate the metal film, causing vaporization of the metal. As the metal is confined, the expansion of the metal generates internal stress in the form of a compressive wave. The compressive wave travels through the coupling medium and until it hits the biofilm-underlying tissue interface. Right: Due to the acoustic impedance mismatch between the biofilm and tissue, the compressive wave reflects back through the biofilm as a tensile wave, disrupting the biofilm

biofilm-tissue interface, the compressive similarly reflects back as a tensile wave through the biofilm, causing disruption and delamination of the biofilm, fig. 2.2, while any unreflected energy continues through the tissue as a compressive wave causing little damage. Therefore, LGS therapy is a tissue-sparing and mechanical method for the removal of bacterial biofilms.

2.6 Current State of LGS Therapy against Bacterial Biofilm

Laser generated shockwaves (LGS), or otherwise known as photomechanical waves, have been previously investigated as a potential therapy against bacterial biofilm. In 2001, work by Nigiri *et al.* shown that shockwaves generated through the ruby laser ablation (wavelength 694 nm, spot size 6 mm, and energy fluence 2486 mJ) of a 1 mm thick black polystyrene, when combined with Vancomycin, was able to significantly reduce *Staphylococcus epidermidis* and

Staphylococcus aureus biofilm on Dacron prosthetic vascular grafts. However they were limited to treating samples the same size as their spot size (6 mm), saw little reduction in samples treated with LGS alone, and achieved a peak pressure ~ 60 MPa[72].

In 2008, Krespi *et al.* developed a handheld, LGS probe with an output shockwave pressure reported to be $800 - 1000$ MPa. This was accomplished with a fiber-based Q-switched Nd:YAG using an energy fluence of 12 mJ and fiber diameter of 300 µm to ablate a Ti disc, generating the shockwave. In his investigations, he demonstrates that this probe can be used to remove *Pseudomonas aeruginosa* biofilm from commonly used prosthetic materials used in otolaryngology, such as sutures, screws, and tympanostomy tubes, using $10 - 20$ shockwaves pulses[73]. However, they were limited to treating samples in a water bath and variability in shockwaves delivered, due to changes in the distance of the probe from the biofilm, while holding the device. These cause this design to be unsuitable for the treatment of biofilms in wounds.

In 2010, work by Taylor, Navarro, *et al.* demonstrated that a single shockwave generated by the LGS design described in sec. 2.5, is able to disrupt *Stapyhlococcus epidermidis* biofilm grown on agar and cause an immediate 55% reduction in colony-forming unit (CFU) counts. This was accomplished through the ablation of 0.5 µm Ti film confined between waterglass and polycarbonate, using a 1064 nm Nd:YAG laser with a 3.0 mm spot size and laser fluence of 1500 mJ. This was reported to generate > 50 MPa shockwave[74]. Further investigations by Navarro, demonstrated that as little as 22.75 ± 0.16 MPa is needed to remove *S. epidermidis* biofilm from polysterene[75].

Finally in 2015, Francis *et al.* demonstrated that thin (0.254 mm) flexible plastics, such as polycarbonate, PVC, and acetate, can be used to replace the inflexible borosilicate glass, previously used as the supportive substrate in the LGS substrate[76]. This was an important first step in translating the LGS technology towards clinical, as wound morphology and patient anatomy are rarely perfectly flat. Thus, the LGS substrate would need to be able to contour to the surface of the wound.

This body of work strives to bring the LGS technology closure to the clinical application of

the treatment of biofilm infected wounds. Past work has predominately focus on the removal of bacterial biofilm from the surfaces of non-biological surfaces (prosthetic materials, plastics, and agar) and has been limited in treatment area size and deliverance accuracy. Therefore the work presented here strove to address these issues.

CHAPTER 3

Visualizing Effects of LGS on Biofilm in a *Ex Vivo* Pig Skin Model

3.1 Introduction

In this chapter, the first steps to investigate the efficacy of LGS against bacterial biofilm in a more clinically-relevant modal will be taken. Previous studies have demonstrated that *Staphylococcus epidermidis* (*S. epidermidis*) biofilm grown *in vitro* on polystyrene can be removed with laser generated shockwaves (LGS) using laser energies as low as $46\,\mathrm{mJ/mm^2}$[4]. However, in comparison to polystyrene, cutaneous wounds have more complex topographies, both chemically and physically. Open wounds contain a wide range of polypeptides and polysaccarides that bacteria can adhere to. Two proteins commonly found in the skin, collagen and hyaluronan, have been shown to increase methicillin-resistant *Staphylococcus aureus* and *Pseudomonas aeruginosa* biofilm biomass, when compared to uncoated controls[77]. On the physical side, skin tissue is inherently more tortuous than flat polystyrene; these folds may shield the biofilm from the effects of LGS treatment. To investigate the effectiveness of LGS against biofilm infected skin tissue, scanning electron microscopy (SEM) images were used to image the biofilm grown on *ex vivo* porcine skin tissue. SEM microscopy was used over fluorescent microscopy, due to two limitations. Fluorescent microscopy requires thin sections of the sample, which would require sectioning of the sample, making it difficult to locate the treated area. Furthermore sectioning introduces artifacts that include the separation of the biofilm from the skin surface, confounding the results. Furthermore, standard live/dead staining would stain both the bacterial and porcine cells, producing too high of a background signal to segment out the biofilm from the underlying tissue. SEM also has the

advantage where the sample, does not need to be sectioned and gives enough resolution to differentiate the bacterial cells from the porcine cells. Porcine skin was used in this study, as it shares many similar characteristics with human skin, in both physical structure and common proteins [78]. Furthermore preliminary work by Ramaprasad *et al.* shown that *ex vivo* porcine skin tissue exposed up to 70.5 mJ/mm^2 exhibited, under histology, no statistical difference to tissues not exposed to LGS treatment, when assessed based on the overall appearance and tissue structure [5]. SEM images of the underlying porcine skin after LGS treatment will help further verify this result.

To assess the efficacy of LGS against biofilm infected skin, the three criteria were assessed: reduction in biofilm biomass/coverage, state of remnant biofilm left, and if there were damages to the underlying skin. Finally, we also investigated the size of the remaining biofilm clusters on the skin after LGS treatment. A reduction in biofilm size, would result in an increase in the surface area to volume ratio. This may led to an increase in antibiotic effectiveness due to better antibiotic diffusion.

3.2 Methods

3.2.1 Preparation of *S. epidermidis* culture

24 h *Staphylococcus epidermidis* (ATCC 35984) cultures, incubated at 37 °C on tryptic soy agar (TSA), were inoculated into 10 ml tryptic soy broth (TSB). This was further incubated at 37 °C, 200 rpm, for 18 h. The culture was centrifuged at 3,000 rpm for 5 min at 4 °C. The supernatant was discarded and the pellet was resuspended in 5 ml of TSB. A working *S. epidermidis* was prepared by dilution of the resuspended solution with fresh TSB, until an optical density of 0.2 at 600 nm (OD_{600}) was achieved. This correlated to a CFU density of 4×10^7 cells/mL.

3.2.2 Preparation of biofilm infected porcine skin samples

Healthy skin samples from the abdomen were obtained from a single pig from the UCLA tissue-sharing protocol and excised before euthanasia. Fat and muscle were removed from the sample, keeping only the epidermis and dermis. Any hair on the surface was shaved off with a razor. The epidermal layer was removed with a razor dermatome to simulate wounding of the skin and to facilitate the colonization of the sample by the bacteria. Eighteen samples at $\sim 1\,\text{cm} \times 1\,\text{cm}$ in area were cut from the wounded skin sample and washed with phosphate buffered saline (PBS). The cut samples were place in individual wells in a 24 well plate and covered with 2 ml of the working *S. epidermidis* solution. The samples were then incubated at 37 °C for 24 h.

2 more samples were prepared, but were placed in PBS to act as negative control.

3.2.3 Preparation of LGS substrate

The LGS substrate used in this study was Titanium (Ti) coated polycarbonate. In a class 100 clean room, 0.127 mm thick polycarbonate was first washed with acetone to remove any oil and debris and dried with dry N_2 gas. The cleaned polycarbonate was then RF sputtered coated with 500 nm layer thick titanium (Ti), using the Discovery Denton Sputterer (Denton Vacuum, Moorestown, NJ). Afterwards, the Ti coated polycarbonate was wrapped in a clean room tissue and kept in a sealed bag until ready for use. In this state, the Ti coated polycarbonate is stable for months. Before usage of the LGS substrate, the substrate was cut to size ($15\,\text{mm} \times 15\,\text{mm}$) and a thin layer ($\sim 200\,\mu\text{m}$) of waterglass was manually applied to the LGS substrate and allowed to dry.

3.2.4 LGS treatment of biofilm infected porcine skin

Prior to LGS treatment, nine 24 h biofilm infected porcine skin samples were removed from the 24 well plate and washed with PBS to remove any non-adherent bacteria. The samples were then placed on top of a 1 cm thick layer of ballistic gel in a six well plate. The gel absorbs

the shockwave energy passing through the skin, preventing reflection of the shockwave back through the sample as a tensile wave. The well is then filled with PBS, which acts as a coupling medium, until the surface of the sample is submerged under 1 mm of PBS.

The waterglass coated LGS substrate was then placed on top of the PBS above the skin sample. A single pulse of 1064 nm Nd:YAG laser, at energy density, 93 mJ/mm^2, and spot size,3 mm, was used to ablate the Ti and create a single shockwave. The shockwave passes through the polycarbonate, through the coupling medium, and through the biofilm, where it gets reflected off the biofilm-skin interface as a tensile wave, which delaminates the biofilm from skin. The shockwave at the biofilm-skin interface has been measured to be ~ 200 MPa [76]. The samples were then washed again with PBS to remove any dislodged biofilm.

The remaining 9 samples were served as positive control and were washed twice with PBS as was done with the treated samples, but were not treated with LGS.

3.2.5 Collection of Bacterial Cells off Porcine Skin and Colony Counting

7 samples from each group were used for CFU counting to determine number of viable *S. epidermidis* cells on the surface of the skin sample. For the LGS treated samples, a sterile 2 mm cotton swab was placed vertically on the center of the treated area, and twisted ten times to collect surface biofilm and bacteria. The swab was then placed in a 14 ml culture tube with 2 ml of PBS. The tube was capped and vortexed for 15 s to dislodge the bacteria from the swab. The swab was removed and the tube was vortexed again to homogenize the suspended bacteria solution. This was repeated for the positive control, with the swab placed at the center of the skin sample.

Each suspended bacteria solution was then serially diluted to 10^{-7}, and 100 µl of dilutions: 10^{-5}, 10^{-6}, and 10^{-7} were each plated on TSA in triplicate. The agar plates were incubated at 37 °C for 24 h. Plates with distinct, separate colonies were counted by two individuals and their counts were averaged. The final CFU concentrations for the two groups were calculated from the average.

3.2.6 Tissue preparation and SEM imaging

The remaining two samples from each group was used for SEM imaging to verify the presence and removal of bacterial biofilm from the surface of the skin sample. Both samples were fixed with 2.5 % glutaraldehyde in 0.1 M sodium cacodylate buffer at pH 7.4 for 24 h. After fixation, the samples were washed three times with 0.1 M sodium cacodylate buffer for 5 min each. To improve structural integrity of the bacteria cells and biofilm, a secondary fixation with osmium tetroxide was performed. Three drops of osmium tetroxide was added to the surface of each sample and allowed to sit for 20 min. The samples were then dehydrated in two stages. The first stage removes the majority of the water through ethanol dehydration. The samples were submersed in 30%, 50%, 70%, 85%, 95%, and 3× 100% ethanol solutions, for 10 min each. The second stage removes the remaining water. This was done by washing the ethanol dried samples with 1.5 ml hexamethyldisilazane for 20 min and allowed to air dry in a fume hood overnight. The dried samples were then sputter-coated with 5 nm layer thick of gold to improve image contrast and prevent charge buildup from the SEM.

The samples were imaged under SEM (JSM-6700F, JEOL, Japan) with 10.0 kV accelerating voltage and a working distance of 7.9 mm. Several representative images were taken of each sample: positive control, negative control, and treated samples, at different magnifications (200×, 600×, and 5000×) to verify biofilm presence and to capture changes in biofilm structure.

3.2.7 False coloring and image analysis

As the field of view needed to capture the treated area is many orders of magnitude larger than the size of a *S. epidermidis* cell, (3 mm vs. 1 µm), a single SEM image that captures the treated area, does not give enough resolution to discern the biofilm from the underlying pig skin. Therefore, in order to visualize the extent of biofilm removal from the treated sample and discern biofilm from the underlying skin, a panorama of 48 high magnification SEM images were stitched together, using Photoshop(Adobe Systems Inc., USA) to create, after processing and stitching, a final 3.756 mm × 2.347 mm FOV image, with a resolution of

2130 pixels/mm (8000 × 5000 pixels image, pixel size = 0.469 µm × 0.469 µm). The image was then manually (painstakingly) false colored, with green representing the bacterial biofilm and bacterial cells and with red representing the underlying skin. Percentage of biofilm coverage was calculated, using MATLAB (Mathworks, MA, USA), by measuring the hue, saturation, and brightness (HSV) value for each pixel, and calculating the percentage of pixels within the green hue range (0.27451 to 0.39216). This was performed with the one representative positive control and one representative LGS-treated sample.

3.2.8 Biofilm Fragmentation Analysis

As mentioned previously, biofilm as a physical and chemical barrier that protects the underlying bacteria from anti-microbial agents, such as antibiotics and disinfectants, by hindering the diffusion or inactivating of the agents. Therefore, fragmentation of the biofilm may improve the diffusion of anti-microbial agents, by increasing the surface area of the biofilm. To evaluate the extent of fragmentation for the non-treated positive control and the LGS treated samples, the false-colored positive control and LGS-treated stitched images were first converted to binary maps, using the same isolation of HSV values. A connected components image analysis was applied to the binary maps, using MATLAB, to obtain a list of pixel area of each separate biofilm piece (hereafter known as cluster). All clusters less than 10 pixels, size of a single bacterium, were excluded. Pixels were then converted to area, (μm^2), to produce the final biofilm cluster size list. The distributions of clusters from each sample were compared and the differences between the mean cluster sizes, median cluster sizes, and skewness were also noted. Histogram of cluster sizes from each sample were created to visualize the distribution. Cumulative cluster graphs was also created to visualize how much biofilm cluster bin contribute to the over biofilm coverage.

3.2.9 Statistics

The comparison of mean bacterial colony counts between the positive and treated samples was analyzed, using the unpaired two-way Student's t-test, assuming equal variance (Orig-

inPro, v8.02, OriginLab Corporation, USA). The comparison of the median biofilm cluster size between the two sample composite images was completed, using a Wilcoxon rank-sum test (MATLAB, USA), due to the non-parametric distribution of cluster sizes. Significance was established with p values 0.05 for both tests.

3.3 Results

High resolution images presented here can be seen in the published IEEE paper [79].

3.3.1 Bacterial CFU Count

Seven samples from both the LGS-treated and positive control samples were swabbed and plated for CFU counting. The mean CFU/ml for the positive control sample was 5.58×10^7, with a standard deviation of 3.00×10^7, and the mean for the treated was 1.71×10^7, with a standard deviation of 1.20×10^7. This demonstrates a significant reduction of 69% in bioburden immediately after LGS treatment ($p = 0.008$).

3.3.2 Verification of Biofilm Removal through SEM Imaging

As seen in fig. 3.1(a,b), pig skin that had not been inoculated with *S. epidermidis* (negative control) still had some bacteria present on the surface of the skin, as the sample was not sterilized before inoculation. However, there is no biofilm present on the surface. In contrast, pig skin inoculated with *S. epidermidis*, but not treated (positive control) is densely populated with bacterial biofilm giving the surface a rough texture, as seen in fig. 3.2(c). At higher magnification of 5000×, fig. 3.1(d), the cocci shape of *Staphylococcus* is evident. Furthermore, at the higher magnification, the layers of bacteria within the biofilm can be seen in the fracture of the biofilm.

In contrast to the positive control, the LGS treated samples showed a different surface topology. At the edge of the treated area, there is a sharp divide between the surface roughness, fig. 3.2(a). To the right of the arrows, the surface looks rough, similar to the

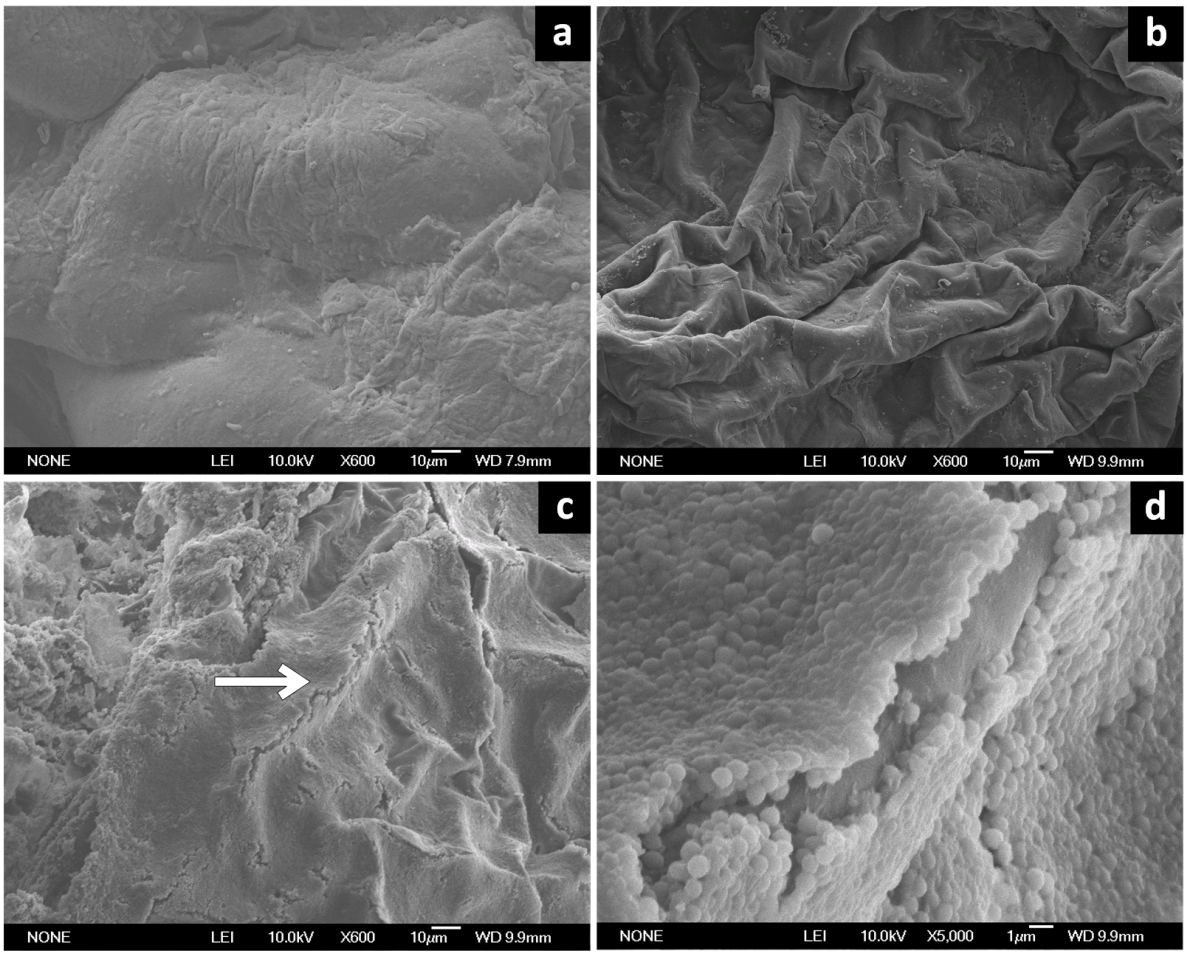

Figure 3.1: SEM Images of *S. epidermidis* Biofilm Controls on Pig Skin. (a) Negative control at 600× magnification. The smooth surface of the skin can be seen in the absence of biofilm. (b) Negative Control at 600× magnification. Some native bacteria can be seen, but no biofilm is present. (c) Positive control at 600×. The entire surface of the skin is covered by a layer of biofilm causing the surface to appear rough. Small fractures in the biofilm can be seen along the ridges (arrow), as a result of tissue shrinkage during the drying process. (d) 5,000× magnification at the arrow in fig. 3.1(c). The 1 µm cocci shape of *S. epidermidis* bacterium can be seen at this magnification. The layers of the biofilm can be seen in the newly exposed edge, along the underlying smooth surface of the skin.

surface seen in the positive control, signifying there is still a dense population of bacteria. However, to the left of the arrows, the surface looks smooth , similar to the surface seen in the negative control, signifying that there was a significant reduction of the *Staphylococci*, revealing the smooth pig skin underneath. At higher magnification, 600×, the treatment area reveals that there were still small pockets of biofilm clusters scattered across the surface, as can be seen in fig. 3.2(b), while there are still single bacterial cells scattered across the

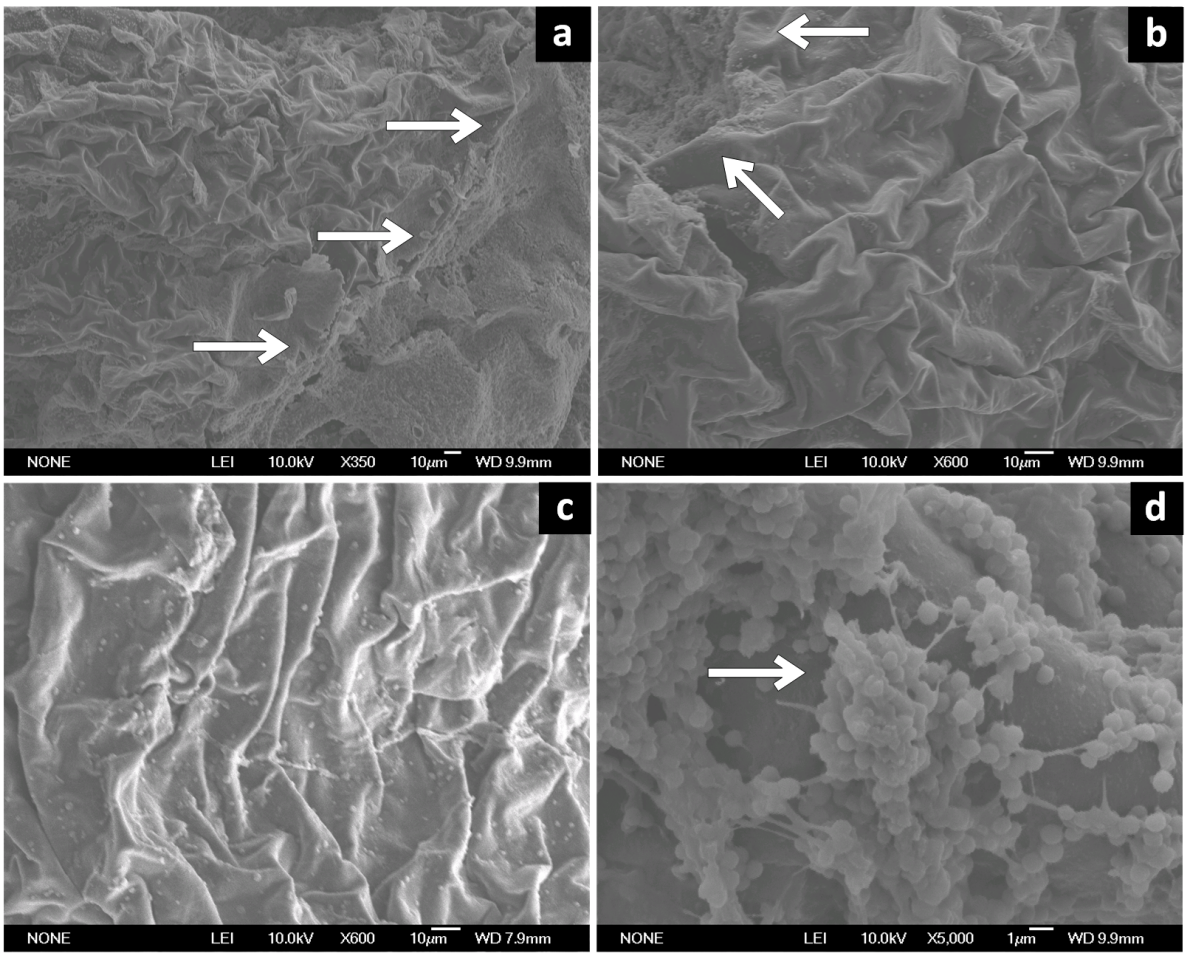

Figure 3.2: SEM Images of *S. epidermidis* Biofilm on Pig Skin after LGS Treatment. (a) Edge of LGS treated area at 350× magnification. A sharp break in biofilm coverage can be seen along the edge of the LGS treated and non-treated area (arrows). (b) LGS treated area at 600×. Significant biofilm coverage has been removed, exposing the smooth underlying skin. Some remnant biofilm can be seen in the upper left corner. (c) LGS treated area at 600×. Much of treated area has very little biofilm present with some bacteria present. (d) Remnant biofilm in LGS treated area at 5,000×. Biofilm cluster size is significantly reduced compared to positive control. Biofilm matrix can also be seen (arrow).

surface, fig 3.2(c). At the highest magnification of 5000× on one of the biofilm cluster, as seen in fig. 3.2(d), the cocci shape can once again be seen. Furthermore, thin strands can be seen extending out from the clusters, suggesting that polymeric matrices were present. This verifies that the *S. epidermidis* was able to colonize the surface and produce biofilm. The smooth surface seen in both fig. 3.2(b,c) suggests that the underlying skin was not damaged by the shockwaves.

3.3.3 False-Colored Stitched Images

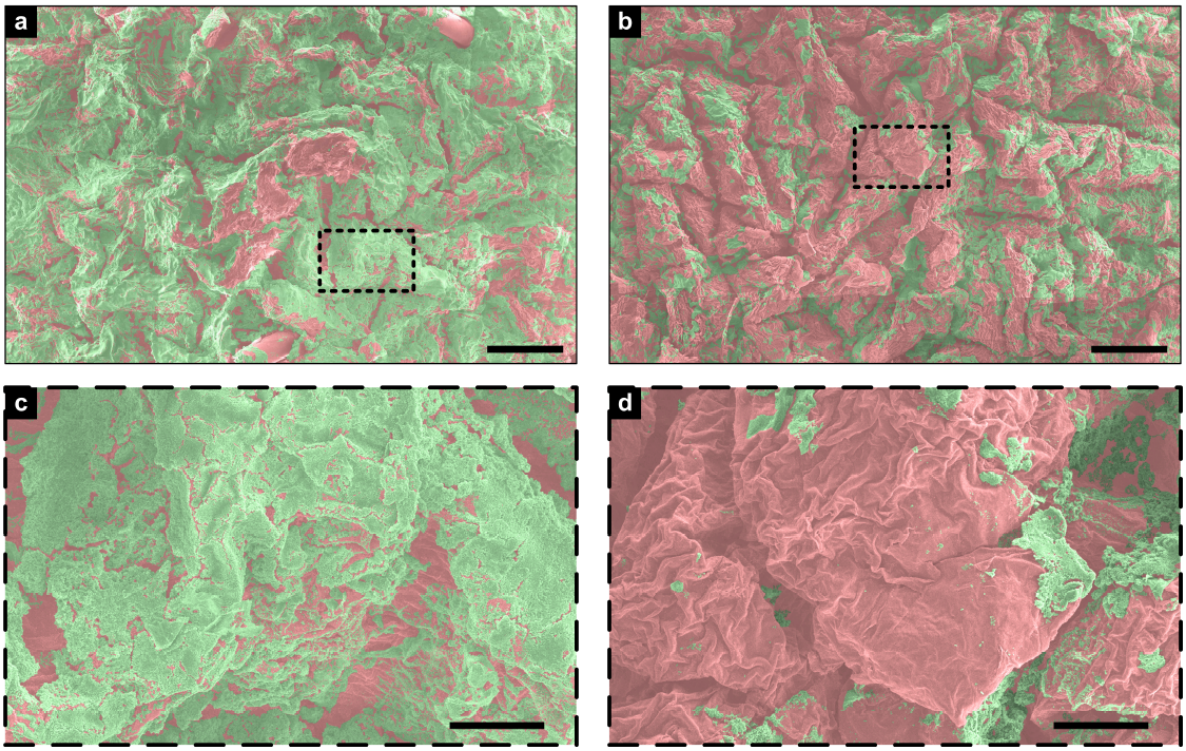

Figure 3.3: False-Colored SEM Images of Positive Control and LGS-Treated Biofilm on Porcine Skin. (a) Positive control. (b) LGS-treated. (c) Close up of positive control. (d) Close up of LGS-treated.

For one representative positive control and one LGS-treated sample, fifty-six images, at 200× magnification, from each sample were stitched together to create two high resolution panoramas. The panoramas were manually false-colored and can be seen in fig. 3.3. Green was used to represent the biofilm and red was used to represent the underlying pig skin. Total biofilm coverage was calculated using MATLAB by calculating percentage of pixels in the green hue range (0.27451 to 0.39216). The positive control had a 68.53% biofilm coverage, while the LGS-treated had a 33.01% biofilm coverage, representing a 52% reduction in biofilm coverage after LGS-treatment. Damage on the positive control, resulting in unintentional removal of biofilm from the surface, lowered the positive control biofilm coverage and percent reduction.

3.3.4 Biofilm Fragmentation Analysis

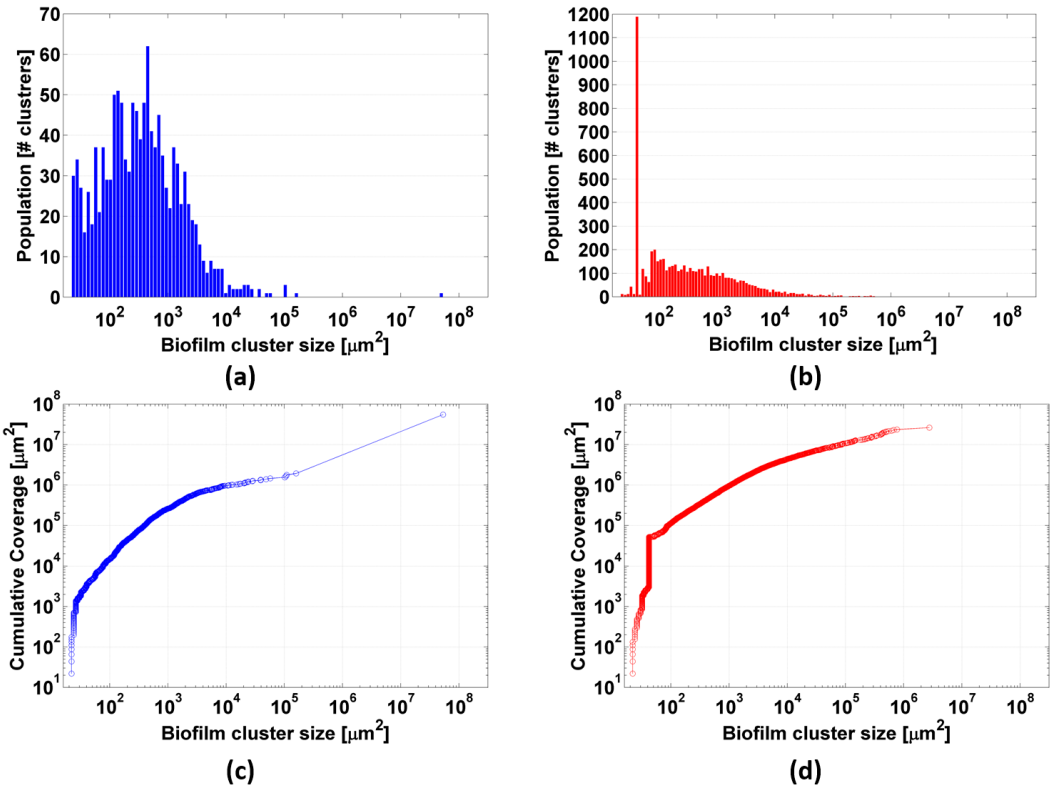

Figure 3.4: Biofilm Cluster Statistic. (a) Positive control biofilm cluster size distribution. (b) LGS-treated biofilm cluster size distribution. (c) Positive control biofilm cluster cumulative area distribution. (d) LGS-treated biofilm cluster cumulative area distribution.

As mentioned previously, fragmentation of the biofilm may improve the effectiveness of anti-microbial agents (e.g. antibiotics), by increasing the available surface area for the diffusion of these agents through the biofilm. The distribution of the cluster sizes for the positive control and LGS-treated samples can be seen in Fig. 3.4(a) and (b), respectively, where the x-axis and y-axis are in log scale, in order to help visualize the spread of cluster sizes. In the positive control sample, the clusters are more normally distributed with some skewness to the right. In contrast, the LGS-treated sample, the clusters are much more heavily skewed to the right and the overall population shifted to the left, representing a very significant increase in the number of clusters under 100 µm. The mean biofilm cluster area for the positive control sample was 4931.2 μm^2, with a standard deviation of 167 366.7 μm^2, while the mean biofilm cluster area for the LGS-treated sample was 474.0 μm^2, with a standard

deviation of 5285.7 µm^2. The median biofilm cluster area for positive control sample was 34.6 µm^2, while LGS-treated sample had a median of 20.5 µm^2. This large difference in the means and medians is due to a small number of clusters contributing a significant percentage of the overall biofilm area. In the most extreme case, a single biofilm cluster in the positive control contributed to over 95% of the total biofilm area.

To better visualize the significance of these few outliers to overall biofilm area, a cumulative area distribution plot was created for the positive control and LGS-treated samples, Fig. 3.4(c) and (d), respectively. Using the same bins used in the distribution plot, the graph was re-plotted with the following equation:

$$C[x] = \sum_{i=1}^{x} N[i]A[i]$$

Where $C[x]$ is the cumulative area at bin x, $A[i]$ is the biofilm cluster size at bin i, and $N[i]$ is the number of samples in bin i. As seen in Fig. 3.4(c), the cumulative coverage for the positive control increases slowly with each additional bin, until the last bin is reached, where the cumulative coverage jumps sharply. The single cluster in the last bin contributes to 96.5% overall biofilm coverage. In contrast, the cumulative coverage for the LGS-treated sample has a large jump in beginning, followed by a slower, but steady increase in cumulative coverage with each additional bin, with the final bin only contributing to 11.3% of the overall biofilm coverage. Finally, the percentage of population in the smaller cluster size bins is quite pronounced in the LGS-treated sample, with cumulative coverage at 100 µm^2 already contributing to 1.92% of the overall biofilm coverage. In contrast, the cumulative coverage of the positive control sample at 1000 µm^2 only contributes to 0.22% overall biofilm coverage. This further illustrates the population shift of the LGS-treated sample to the small cluster sizes (i.e. significant fragmentation of biofilm was observed following LGS treatment).

As the data were non-parametric, a Wilcoxon rank-sum test confirms the difference between the medians of the two samples to be significant ($p < 10^{-4}$).

3.4 Discussion

The results shown here demonstrate that LGS can still effectively remove biofilm grown on a skin model. There was a 69% reduction in CFUs between the LGS treated samples and the untreated controls. This value is higher than the previous cited study performed by Taylor *et al*, where they reported a 55% reduction in CFUs for LGS treated biofilm grown on agar [74]. However, as they included the washes in their CFU measurements, they were measuring the bactericidal effect of LGS, rather than the efficacy of LGS in eliminating bacteria from the surface, which would be higher. Regardless, the results suggest that LGS is not significantly hindered by the chemical and structural properties of skin tissue and may be effective at removing *S. epidermidis* biofilm from cutaneous wounds. However, one important limitation in this design study was that the biofilm grown here was in a nutrient rich tryptic soy broth, which may cause the biofilm to grow more loosely, as the nutrients can readily diffuse from the solution into the biofilm. A model closer to clinical conditions would need to change the nutrient dynamics, where the bacterial nutrients are predominantly provided by the skin tissue itself. This may produce a stiffer and more tightly bonded biofilm.

In this study, LGS' ability to remove biofilm was also quantified, which was also missing in the previous studies[74, 4, 72]. As biofilm provides a suitable growing environment for a wide host of bacteria, not just for the biofilm-producing species [80], removal of biofilm matrix is an important metric to consider to prevent recolonization of the wound. The results shown here demonstrates a 52% reduction in biofilm coverage in the LGS treated sample vs the untreated control, and no damage was observed in the newly reveled underlying porcine skin tissue. This verifies the initial hypothesis on the mechanism of LGS, i.e. shockwaves can delaminate the biofilm without damaging the underlying tissue. However, this value is an underestimation, due to two issues. The first is the untreated control was damaged in the processing, as seen in fig. 3.3a, with the red streaks in the center, where the biofilm was accidentally removed. The second issue was that only a single 3 mm spot was used to treat the $1 \times 1\,\mathrm{cm}^2$ skin sample. This correlates to an effective treated area of $\sim 7\%$ of the total area. However, even this is not fully accurate, as the drying process curls the edges of skin

away from the imaging plane, changing the ratio of treated area vs untreated area seen in the image.

Despite these limitations, the results demonstrate a preliminary step in demonstrating that LGS can be effective in removing bacteria cells and biofilm from a tissue surface and may be effective in treating bacterial biofilm infections.

CHAPTER 4

Development of Nd:YAG Raster Scanner

4.1 Introduction

In this chapter, we will cover the development and design in a portable Nd:YAG raster scanner system. As seen in the previous chapter, one of the major limitations in the study was the inability to treat the entire surface, leading to significant biofilm present in untreated areas. This is currently an unaddressed issue, as seen in the sec. 2.6. Many published works on LGS therapy on biofilm, were limited to samples that were the same size as the laser spot size[74, 72]. Since the ultimate goal of this technology is to treat biofilm infected wounds in a clinical setting and wounds that require medical attention are not smaller in area than the 3 mm Nd:YAG spot nor do they follow a standard shape, a raster scanner capable of quickly scanning the Nd:YAG laser over any shape is needed. Finally, the raster scanner system will also need to be portable, as the experiments performed in this study will be carried out in different facilities and the system will need to be moved. This will also help address a future aim, as the therapy is envisioned to be perform in a clinician's office. Therefore, the system will need to able be transportable between rooms.

4.2 Design Considerations

The portable raster scanner will be used in our investigations in the efficacy of LGS against *in vitro* bacterial biofilm and the safety of LGS in a rodent model. Therefore, the scanning head will need to deliver LGS to an area of at least $2 \times 4\,\mathrm{cm}^2$, with a spot size of 2.2 to 4.2 , energy fluence of 248.0 to 777.9 mJ, and maximum scanning time of less than 1 min. Finally,

the scanning head will also need to be compact in order to increase portability.

To address the need for a compact scanning head, the design of the head will be based on a set of revolving mirrors, instead of a classic XY stage. This allows the scanning head to treat an area that is larger than itself. To achieve a variable spot size, the scanning head needs to be able to move closer and farther from the target, while maintaining sufficient working distance. The treatment area will shrink, as the scanning head moves closer. To ensure that the maximum scanning time is less than 1 min to deliver the maximum number of spots needed in a treatment is 221 spots when a 2.2 mm spot size is used over a $2 \times 4\,\mathrm{cm}^2$ area, a minimum firing rate of 3.7 Hz is required. Finally, the system should be as automated as possible to minimize down time during set up.

4.3 Nd:YAG Raster Scanning Head

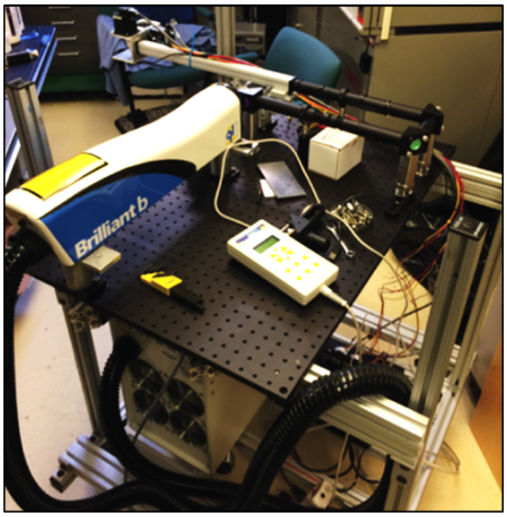

Figure 4.1: Photograph of LGS system on a cart. In the foreground, the Nd:YAG laser head can be seen on the top of the cart, with optical tubes and mirrors to direct the laser to the scanning head. The optical breadboard can be moved higher and lower to change the laser spot size on the target.

To make the system portable, the entire setup was adapted to a large cart, fig. 4.1. This allows the system to be transportable between the facilities. The scanning head hangs over the edge of the cart and the spot size of the Nd:YAG laser is determined by the distance between the scanning head and the target. This can be adjusted by manually moving the

optical breadboard higher and lower on the cart.

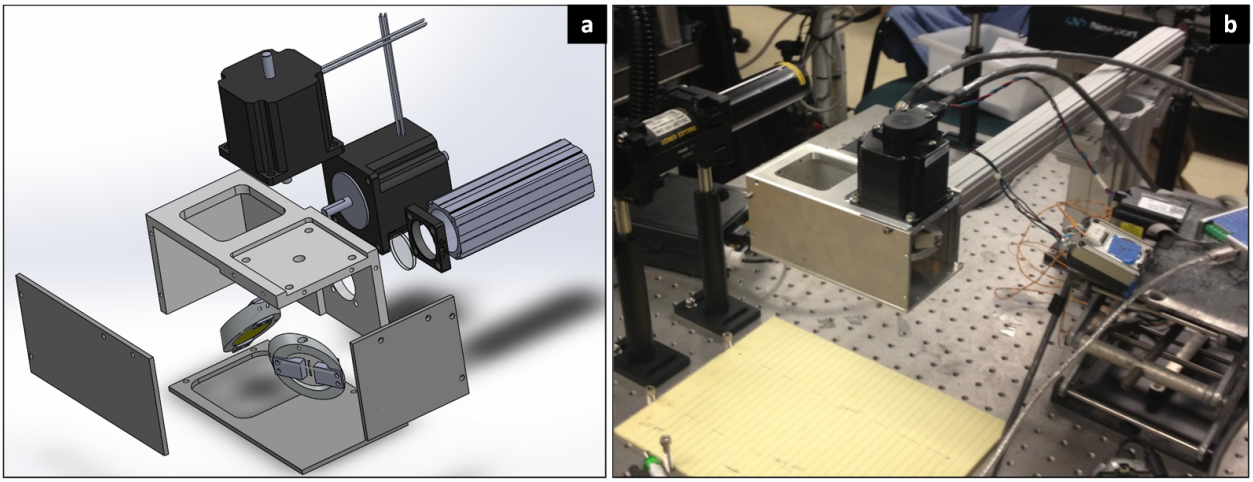

Figure 4.2: Nd:YAG Scanning Head. a) Exploded CAD drawing b) Assembled scanning head.

The Nd:YAG 1064 nm laser used for this work was the BrillantB produced by Quantel Laser^{TM}(France). It is a Q-switch 8 ns pulsed 1064 nm laser, capable of delivering energy fluence of 248.0 to 777.9 mJ at rate of up to 10 Hz. As seen in fig. 4.2, the Nd:YAG laser enters the scanning head from the optical rail and is first focused with a fixed long focal distance lens mounted between the rail and the scanning head. The focused beam is then controlled by two sets of revolving mirrors that connected to high precision DC stepper motors, which are controlled through software to direct the beam.

Focusing Lens

The lens used to focus the Nd:YAG laser is a ⌀1 in Plano-Convex Lens (ThorLabs, NJ, USA), which has been coated with N-BK7 for high power lasers with 532 and 1064 nm wavelengths. As the scanning head needs a working distance of at least 20 cm, a focal length of 750 mm was used. This allows us to focus the 9 mm beam to 3 mm with a working distance of 21.6 cm from the scanning head.

DC Stepper Motor and Controllers

The motors used for this system were Size 23 5704 High Accuracy DC Stepper Motor (Lin Engineering, Morgan Hills, CA), with step size of 0.45 °/step. The motors also contain E2 optical encoders (US Digital, WA, USA), for homing of the motors during start up. The motor controllers used are the MForce MicroDrive Motion Control (Schneider Electric, France). These controllers have built in functions to home the motors using the attached E2 optical encoders. They also allow 51200 microsteps per step, so combined with the high accuracy DC stepper motor, a resolution of $8.9 \times 10^{-6\circ}$ can theoretically be achieved. The high torques and holding torques provided by these motors[81], allows us to not worry about slippage, which may arise when sudden accelerating and decelerating of the revolving mirrors. Therefore, we can operate the motors at the highest speed the motor controllers are capable of, without having to implement additional software to account for slippage.

Nd:YAG Mirrors

The mirrors used to control the XY movement of the Nd:YAG laser were ⌀1 in broadband dielectric mirrors (750 - 1100 nm) (ThorLabs, NJ, USA). These mirrors have high reflectance at 1064 nm and high energy threshold 0.5 J/cm^2 (1064 nm, 10 ns, 10 Hz, ⌀0.433 mm)[82]. The mirrors pictures in fig. 4.2 were 1 in protected gold elliptical mirror(ThorLabs, NJ, USA) used in a previous design. However, they were replaced with the broadband dielectric mirrors, as the gold is not able to withstand repeated firing of the Nd:YAG laser within the time span needed for a 3 Hz minimum scanning system.

Camera for System Vision

As seen in fig. 4.3, a simple off the shelf webcam was mounted to the bottom of the scanning head. The camera had a resolution of 480p and manual focus. The manual focus ensures that the focal plane does not change during the operation of the system, especially during the initial calibrations, where changes can lead to incorrect calibrations. The addition of a camera, further increases the safety of the system, as the user can watch the treatment

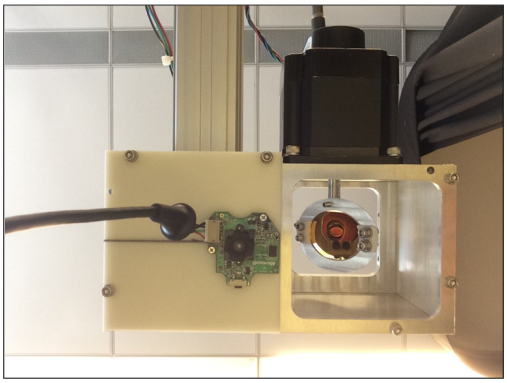

Figure 4.3: Nd:YAG Scanning Head Bottom View. A 480p webcam with manual focus is attached to the bottom of the scanning system to provide computer vision.

process from the camera rather than directly

System Control and Flow

The entire system is controlled by a single laptop running a custom made MatLAB script. The flow of the system is as follows. The webcam provides an image of the treatment area to the script. The user then designates the treatment area, which determines the laser positions needed to treat the surface. How the software determines this will be described in the following section. Once the laser positions are determined, the software tells the motor controllers, via a serial to USB converter, to move the motors to the position needed to achieve the correct X and Y positions. The software then sends a signal to a DG645 ultra-low jitter delay generator (Stanford Research Systems, CA, USA) to trigger the next Nd:YAG laser pulse. The delay generator is set at single shot mode, which takes the flashlamp out signal from the Nd:YAG laser and then triggers the Q-switch after a set delay, dictated by the software. This allows us to have precise control over when the laser fires and the laser energy fluence.

4.4 Software

The movement of the Nd:YAG laser due to the rotation of the mirrors can be determined using the following equation:

$\Delta\theta = tan^{-1}\frac{x+\Delta x}{h} - \theta$

$\Delta\theta$ is the change in motor position in degrees, x is the current x position of the laser, Δx is the change in x position, h is the height of the mirrors from the target, and θ is the current motor position in degrees. However, in practice it is very difficult to determine θ and h, as the exact motor angle relative to the surface is very difficult to determine accurately. Furthermore, this will also change between facilities as each treatment area may be at a different angle relative to the scanning head. The height is difficult to determine similarly, due to the fact that the 2 mirrors do not lie on top of another and will have different distances from the surface. Therefore, we will use the attached camera to allow the system to calibrate itself and learn how to move the motors to direct the beam to the desired location.

Calibrations

Once the laser spot size has been adjusted for the experiment via adjustments in the scanning head height, the system needs to be calibrated, so the relationship between the laser movement in the camera and the motor movements are known. To accomplish this, a sheet of thermal paper is placed in the field of view of the camera at the same distance away as the sample would be. Each motor is homed, so the exact position of the motors are known. The x and y motors are moved so the laser beam would appear on the left middle side of the image. The delay generator is set to 400 µs delay between the flash lamp firing and the Q-switch triggering, to allow tighter packing of the spots. A before image was taken and the laser was fired, producing a $\sim$ 1.5 mm spot. Another image was taken by the camera and using MatLAB, an image subtraction was performed to isolate the spot. Using MatLAB Image Toolbox, the largest object was found in the image and the pixel position of the center of the object was obtained. This was stored in an array, along with the current x motor position. The x motor then moved 250 microsteps, which moved the spot right by $\sim$ 1.5 mm. The process was then repeated until the entire length of the field of view was transversed. This was repeated using the y motor, with the initial spot starting at the top middle of the image and transversed down.

After the two arrays have been obtained, the data from each array was curved fit to a 5th order polynomial using the MatLAB curve fitting toolbox. This resulted in two equations whose input is the desired pixel position in either x or y and the output is the corresponding motor position.

The next calibration needed is to determine the size of each pixel in millimeter, so the software can determine how far apart to position the spots based on the image data. This is accomplished by placing 3 quarters in the imaging field. Then using the 'imfindcircles' function from the MatLAB image processing toolbox, the radii of each circle is obtained. As the U.S. mint manufactures the quarters to a very high tolerance of < 0.01 mm, this allows us to accurately set the pixel dimensions by dividing the radius of a quarter (12.13 mm) by the average radii length in pixels. We assume that the x and y pixel dimensions are equivalent.

Usage of Raster Scanner System

Once the the pixel dimensions and motor position equations have been obtained, the system is fully calibrated. To treat a sample, the sample is first placed in the imaging field at the correct distance from the scanning head. The camera takes an image of the sample and displays it to the user. The user then defines the starting location of the where the LGS scanning will start and then enters the number of spots across and down. The user also sets the spot size of the laser, which was defined previously before the calibration, and sets the power of the laser by inputting the delay between the firing of the flash lamps and the triggering of the Q-switch. A delay of 210 µs resulted in a energy fluence of 777 mJ. Once this has been inputted, the software converts the spot size from mm to pixels and determines a list of motor positions that packs the spot size over the desired treatment area in a hexagonal pattern. This is displayed to the user as the original image with the expected laser positions overlaid on top. Once the user confirms this layout, the system continues on with the laser treatment.

During laser treatment, the system moves the laser spot to the first position listed and triggers the firing of the laser through the delay generator. The system waits for 110 ms,

before moving the mirrors to the next position. As the maximum firing rate of the laser is 10 Hz or once every 100 ms, the delay was introduced to ensure the laser is fired before moving to the next spot. This, however, means that the system does not fire at the maximum possible rate of 10 Hz and instead fire at a rate of $\sim$ 9 Hz, which for our purposes is fast enough.

Finally, the user is not limited to the laser spot pattern defined by the system. A custom laser pattern can be uploaded to the software, by simply providing a list of motor positions in the desired order. This allows flexibility in both the shape of the treated area and the order of the treated spots. The latter may be important if it is found that rapid successive adjacent shots lead to secondary effects, due to shockwaves interacting with each other.

4.5 Design Outcomes

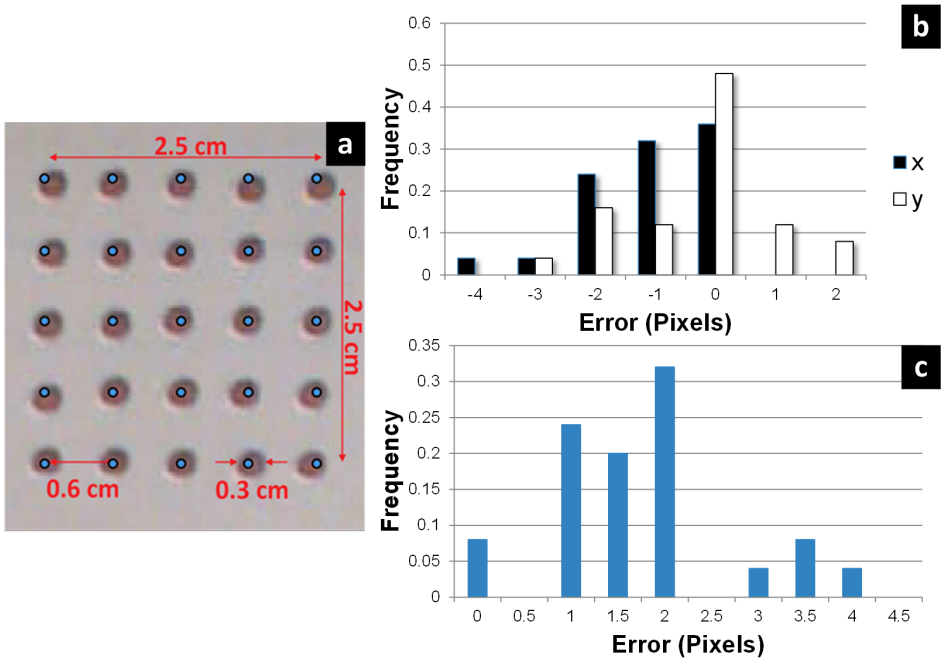

Figure 4.4: Accuracy of the Raster Scanner System on a Flat Surface. a) A grid of 5×5 3 mm spots were created using the raster scanner. A grid of smaller blue dots representing the desired centers of the laser spots. b) Error in x and y for expected vs actual center placement. c) Error in absolute distance for expected vs actual center placement. Pixel dimensions for this image was 0.25 mm/pixel.

As a test for the accuracy of the raster scanning system in the ideal condition, a grid of 5×5 spots were fired onto a flat sheet of thermal paper and a image of the spots was taken afterwards. This was then compared against the desired laser position centers displayed in blue in fig. 4.4a. We first analyzed the x and y errors separately by calculating the two errors in pixels for all spots and graphed in a histogram, seen in fig. 4.4b. A plurality of spots had 0 errors, while the largest error seen was at 4 pixels shifted to the left, which correspond to 1 mm, as the pixel dimensions were 0.25 mm/pixel. Only errors to the left were seen, which may be a result of the camera placement. As seen in fig. 4.2, the camera is offset in the x direction from the mirror axis. As for the errors in the y direction, a plurality of spots also had 0 errors in the y direction. However there is even distribution in the up and down direction. Once again this may be a result of the camera sharing the same y axis as the mirrors. The largest error seen in the y axis was 3 pixels (0.75 mm in the up direction. As for the absolute error, fig. 4.4c, the average error is 2 pixels, with the largest error still contained to within 4 pixels, 1 mm. As the errors are within the radius of a spot size, the system was deemed to be sufficiently precise to be used for our experiments.

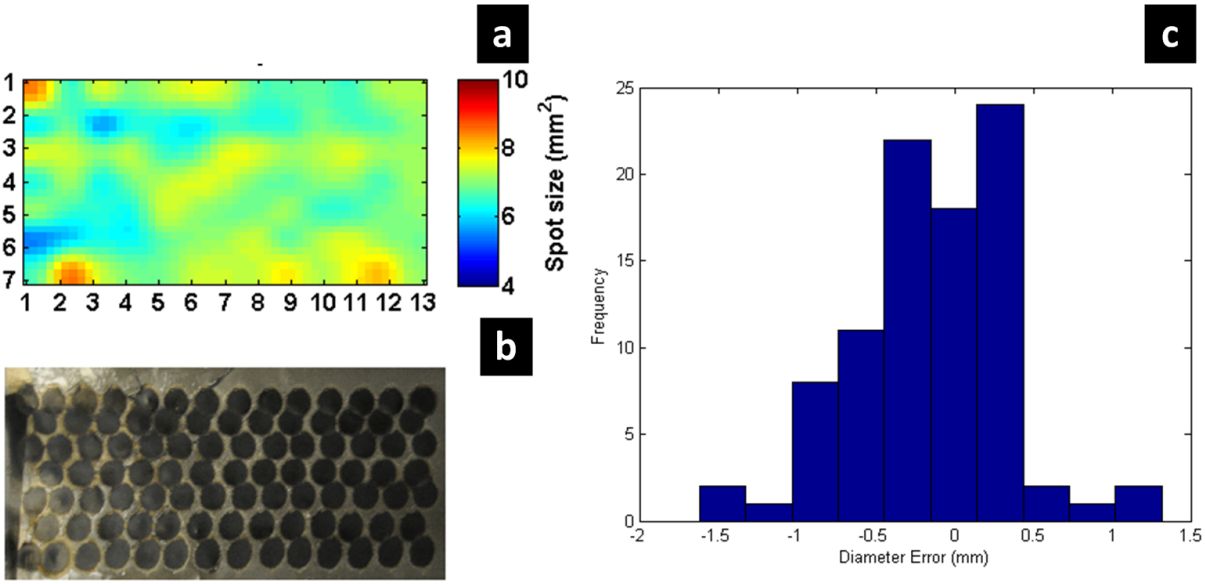

Figure 4.5: Changes in Spot Size during Raster Scanned LGS Treatment of a Rodent in the Safety Study. a) Heat map of the actual spot sizes over the entire treated area, with 7.1 mm^2 corresponding to a 3.0 mm spot size. b) Image of the actual spot sizes. c) Histogram of the error in diameter of the spot sizes.

In the second investigation, the LGS raster scanner was used to treat a $2 \times 4\,\mathrm{cm}^2$ area on the left lateral side of a Sprague-Dawley rat, as part of the safety study presented in ch. 9. In the *in vivo* setting, the animal has curvature to its anatomy and their is movement due to breathing. Therefore, there will be changes in the z axis, which would affect the final spot size of the Nd:YAG laser. The final laser placements can be seen in fig. 4.5b. A heat map of the size of each spot was created with a 3.0 mm spot size ($7.1\,\mathrm{mm}^2$) represented in green, while the error in diameters of the spot sizes can be seen as a histogram in fig. 4.5c. The histogram is centered around 0 mm, with the largest error up to 1.5 mm, but the majority of the spots were within 0.5 mm of the desired 3.0 mm. The largest deviations were found on the edges of the treatment area where the curvature was the greatest. However, in practice, the treatment area will be slightly bigger than the sample, so deviations in the edge spots are acceptable. The deviations in size for the center spots are negligible. The low deviations can be attributed to the long focal length used in the raster scanner.

4.6 Conclusion

We have built a raster scanner system that can easily and quickly treat a sample of at least $2 \times 4\,\mathrm{cm}^2$ in area and in any given shape. This greatly increases the previous possible treatment area size and allows us to investigate more closely the effects of LGS and its effects on bacterial biofilm and cells. Previously, measurements in biofilm removal were underestimating the true effects of LGS, as much of the sample is untreated. Therefore, in the next chapter we will investigate the true efficacy of LGS against biofilm *in vitro*.

Furthermore the development of the raster scanner system is a major transition from a bench top only system to one capable of pre-clinical studies. This is a major step towards bringing the technology to clinical. The speed and accuracy shown here allows future experiments to be performed significantly faster and more consistently over the previous method of manually scanning the beam over the target surface. Finally on the clinical side, the speed obtained here is highly desirable, as it takes less than 20 s to treat an area of $2 \times 4\,\mathrm{cm}^2$, minimizing the amount of down time for the clinician.

CHAPTER 5

Laser Generated Shockwaves Potentates Effects of Gentamicin on Biofilm

5.1 Introduction

In this chapter, the activity of laser generated shockwaves to enhance antibacterial activity against biofilms *in vitro* is investigated. Currently, little work has been published to quantify the extent of biofilm removal and the long-term effects of LGS therapy on antibiotic treatment. Improved understanding of this relationship is key to clinical translation, as studies have shown that the biofilm matrix itself can inhibit the effectiveness of antibiotics[83]. Disruption of the biofilm may also allow antibiotics to penetrate the biofilm and permit lower concentrations to become effective. Furthermore, as high concentrations of antibiotics can lead to serious side effects, such as nephrotoxicity and ototoxicity for aminoglycoside class antibiotics [84, 85], increased effectiveness of low antibiotic concentration is highly desirable. The antibiotic used in this study is gentamicin, in the form of gentamicin sulfate, as it is a common antibiotic that can be used against a wide range of bacteria, including *Staphylococcus* and *Pseudomonas*[86].

Gentamicin is an aminoglycoside, which works by irreversibly binding with the 30s subunit in bacterial ribosomes, stopping protein production. For activity of gentamicin against *S. epidermidis*, the minimum inhibitory concentration (MIC), i.e. minimum concentration needed to stop planktonic bacterial growth, has been measured to be 31.25 µg/ml, while the minimum bactericidal concentration (MBC), i.e. minimum concentration needed to kill bacteria in, has been measured to be 62.5 µg/ml[87]. Finally, the minimum biofilm elimination concentration (MBEC), i.e. minimum concentration needed to remove all the bacteria

from the biofilm, is not clearly defined as it is $> 1000\,\mu g/ml$[87]. Therefore, gentamicin can be considered to have low efficacy against mature biofilms. Furthermore, due to its toxicity, blood serum levels of gentamicin has been limited to $4\,\mu g/ml$. Therefore, increased effectiveness of gentamicin at low concentrations, would greatly improve the effectiveness of gentamicin against cutaneous wounds.

This study has a secondary aim. Previous studies, such as the study presented in chapter 3, have been limited to a single shot, when studying the effects of LGS against *S. epidermidis* cells and biofilm. However, this inflates the actual effectiveness of LGS. As the LGS supportive substrate used in this study is transparent to 1064 nm light, the circular beam has to be raster scanned in a way to prevent spot overlap, which would cause laser bleed-through, resulting in thermal injury. Therefore, a hexagonal pattern was used to raster scan the laser, which gives a 90.7% packing efficiency. As this was the first time the raster scanner was used against a biofilm area much bigger than the spot size ($> 50\times$), the efficacy of the hexagonal packing pattern will also be analyzed.

5.2 Methods

A significance level of 0.05 was used for all statistical testing.

5.2.1 Biofilm Preparation

Preparation of static biofilm samples on glass coverslips was adapted from Bakkiyaraj *et al.* [88]. 24 h *Staphylococcus epidermidis* (ATCC 35984) cultures, incubated at 37 °C on mannitol salt agar, were inoculated into 45 ml tryptic soy broth (TSB). This was then further incubated at 37 °C for 18 h. Next, the cultures were centrifuged at 3,000 rpm for 5 min at 4 °C. The supernatant was discarded and the pellet was resuspended in 45 ml of fresh TSB. A working *S. epidermidis* solution was prepared by further diluting with TSB, until an optical density at 600 nm (OD_{600}) of 0.2 was achieved, correlating to a cell density of 10^6 cells/mL.

22 mm diameter glass coverslips (Schott D263M) were cleaned with deionized water,

methanol, and acetone to remove residual oils and debris. The coverslips were then sterilized in an autoclave at 121 °C for 15 min. The sterilized coverslips were individually placed in each well of a six-well culture plate, and 2 ml of the working S. epidermidis solution was added to submerge the coverslips. The culture plates were incubated at 37 °C for 72 h, with the media changed with fresh TSB every 24 h to form mature *S. epidermidis* biofilms.

Mature biofilm growth is visible and manifests as an opaque layer over the entire surface of the coverslip. The mature biofilms were washed three times with 4 °C phosphate buffered saline (PBS) to remove any planktonic bacteria and transferred to a new six-well plate containing 2 ml of 4 °C PBS in each well to keep samples hydrated. The plates were kept on ice until ready for treatment.

5.2.2 Preparation of LGS Substrate

A 0.5 µm layer of titanium was deposited onto a 0.1 mm thick polycarbonate plastic via RF sputtering, as described previously for plastics sample preparation [76]. A 15 µm layer of waterglass was manually applied to the titanium side of the polycarbonate and allowed to dry for 20 min. To ensure that the distance between the LGS substrate and coverslips were consistently 1 mm apart, a round 1 mm thick acrylic spacer was attached to the plastic side of the polycarbonate with double-sided tape.

5.2.3 LGS Treatment

The samples were divided into positive controls immediately post-treatment (0 h^+, n=6) and 24 hours post-treatment (24 h^+, n=11), gentamicin therapy alone at three different concentrations (G[31 µg/ml], n=6; G[62 µg/ml], n=6; G[124 µg/ml], n=6), LGS therapy alone immediately post-treatment (0 h^+ LGS, n=6) and 24 hours post-treatment (24 h LGS, n=9), and LGS with gentamicin combination therapy (LGS + G[31 µg/ml, MIC], n=6; LGS + G[62 µg/ml, MBC], n=6; LGS + G[124 µg/ml], n=6). Following treatment, three samples from each group were used for CFU count analysis to determine viable cell concentration. The remaining samples from each group were used in the biofilm assay to determine biofilm

density.

Prior to LGS treatment, 1 ml of PBS was removed from the prepared samples to lower the height of remaining solution to 1 mm. The prepared LGS substrate was placed spacer side down, thereby covering the biofilm surface of the coverslips. LGS treatment was administered across the entire sample for the following treatment groups: LGS 0 h, LGS 24 h, LGS + G[31 µg/ml], LGS + G[62 µg/ml], and LGS + G[124 µg/ml]. This was accomplished by focusing a 1064 nm Nd:YAG laser (Brilliant B, Quantel, France; fluence 110.1 mJ/mm^2, pulse duration 5 ns, spot size 9 mm), to a 3 mm spot size with a long working distance lens. Using a camera attached to the scanning head, an image of the 13 cm × 10 cm scanning area was imported into an in-house controller software, programmed in Matlab (Mathworks, Natick, MA). The software actuates a pair of mirrors close to the lens to raster scan the focused beam over the sample, based on the location of the sample in the image. This allowed for flexibility in the treatment for sample size (not needed for this study) and for sample placement. For each individual treatment, the laser ablates the thin titanium film confined between waterglass and the polycarbonate. The waterglass directs the resultant shockwave from the metal ablation down into the biofilm, while the polycarbonate provides structural integrity to the titanium film and is opaque to the laser wavelength, to prevent laser bleed-through to the sample.

After the treatment, the samples were washed three times with 4 °C PBS and transferred to a new six-well plate with 2 ml of fresh 4 °C PBS. LGS 0 h was immediately analyzed for CFU counts and biofilm burden. PBS was removed from LGS 24 h, LGS + G[31 µg/ml], LGS + G[62 µg/ml], and LGS + G[124 µg/ml] samples and 2 ml of TSB containing 0, 32, 64, 124 µg/ml gentamicin (Sigma-Aldrich, St. Louis, MO) was added to each well. The samples were then incubated at 37 °C for 24 h. Afterwards, the samples were washed three times with 4 °C PBS and transferred to new wells. 2 ml of 4 °C PBS was added to each well and the samples were kept on ice until ready to be analyzed via CFU counts and biofilm assay.

Non-LGS-treated samples (0 h$^+$, 24 h$^+$, G[31 µg/ml], G[62 µg/ml], G[124 µg/ml]) were treated similarly, with the exception that no prior LGS treatment was performed.

5.2.4 Biofilm Bioburden Assay

Bacterial biofilm burden was measured based a protocol previously described by Merritt *et al.* [89]. PBS was first removed from each well of the sample. The samples were then stained with 2 ml of 0.1% crystal violet for 10 min. The excess staining solution was removed and the samples were washed three times with 2 ml of PBS. The plates were allowed to air dry overnight in a fume hood. 2 ml of 30% acetic acid were added to each well to resolubilize the dye. The OD_{600} of the solutions was then measured with a spectrophotometer (GE Healthcare BioSciences AB, Uppsala, Sweden).

A negative control ($0\,h^{-}$) was prepared to confirm that TSB and PBS used do not adhere to the glass coverslip to produce a false positive. Three similarly cleaned and sterilized coverslips were placed in separate wells in a six-well plate. Sterile TSB was added to each well and the samples were incubated at 37 °C for 72 h. The coverslips were then washed 3 times with PBS and transferred to a new six-well plate and the biofilm assay was repeated.

The absorbance readings of the solutions were normalized by the area of the coverslip. Statistical significance was determined by a two-tailed Students t-test.

5.2.5 CFU Densities Analysis

CFU counts were determined based on the Miles and Mirsa method [90]. Samples submerged in 2 ml of PBS from the well were broken into small pieces in solution. The sample, along with the solution, was transferred to a 14 ml culture tube. Samples were vortexed for 20 s to completely remove the biofilm from the glass coverslip and suspend the bacteria in solution. The glass shards from the broken coverslips acted as glass beads to scrape the biofilm off the glass. After vortexing, the originally turbid glass pieces were transparent, indicating the biofilm has been successfully suspended into solution. The solutions were then serially diluted to $1{:}10^{-7}$ with PBS. Using a micropipette, 3 drops (each 20 µL) of the $1{:}10^{-7}$ dilutions were placed on one quadrant of a mannitol salt agar plate and the droplets were allowed to be absorbed into the agar. This was repeated for the $1{:}10^{-4}$, $1{:}10^{-5}$, and $1{:}10^{-6}$ dilutions, and the process was repeated in triplicate. The plates were then incubated at 37 °C for 24 h

or until visible colonies were observed. The colonies were counted manually and the CFU densities of the samples were calculated by first determining the total CFUs in the 2 ml of solution and then dividing by the surface area of the coverslip. Statistical significance was determined by a 2-tailed Students t-test, using MATLAB (Mathworks, Natick, MA).

5.2.6 Analysis of LGS Therapys Effect on Gentamicin Therapy

To analyze how the addition of LGS therapy may potentiate gentamicin therapy, biofilm bioburden and CFU densities data sets: 24 h^+, G[31 µg/ml], G[62 µg/ml], G[124 µg/ml] and LGS 24 h, LGS + G[31 µg/ml], LGS + G[62 µg/ml], LGS + G[124 µg/ml] were fitted against an exponential decay without offset, $y = Ae^{-x/t}$, and exponential decay with offset, $y = Ae^{-x/t} + y_0$ (Origin Pro 8, OriginLab, Northampton, MA), where y is the CFU density in CFU/mm^2 and x is the gentamicin concentration in µg/ml. Furthermore, comparisons of A and $A + y_0$, gives insight to the effects of LGS alone and when compared in conjunction with t, provides insight to if LGS treatment can increase the susceptibility of the *S. epidermidis* to gentamicin.

The two data sets coefficients were compared by computing a z-score. The equation for computing the z-score for y_0 is given below:

$$Z = (y_{0,1} - y_{0,2})/\sqrt{SE_1^2 + SE_2^2}, \textit{ where SE represents standard error}$$

The same was done for A and t. The p-value was calculated with Matlab for a two-tailed z-test:

$$P = 2(normcdf(-|Z|, 0, 1))$$

5.3 Results

5.3.1 Biofilm Bioburden Assay

Fig. 5.1 illustrates the biofilm densities following different treatment parameters. When compared to 0 h^+, all concentrations of gentamicin-treated samples demonstrated statisti-

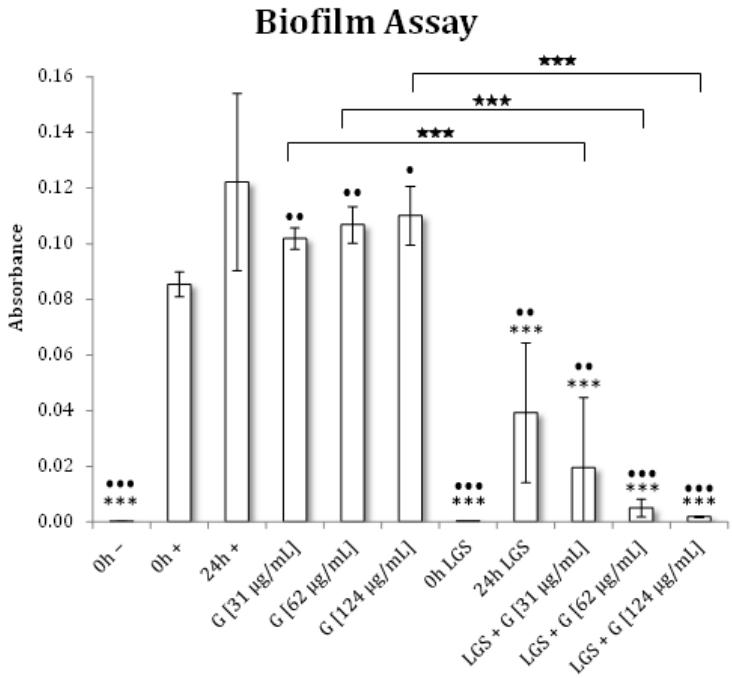

Figure 5.1: Biofilm burden (OD_{600}) as calculated by biofilm assay for *S. epidermidis* with LGS and gentamicin. Statistical significance was found using a 2-tailed t-test that compared each group to $0\,h^+$ ($*$) and $24\,h^+$ ($\bullet$). Pairwise comparisons were also made for gentamicin treatment with and without prior LGS treatment ($\bigstar$). Levels of significance are designated as follows: $> 5\%$ ($*$), $> 3\%$ ($**$), $> 1\%$ ($***$).

cally increased growth after 24 h($P < 0.05$). This supports previous findings that, even at the highest concentration of gentamicin, antibiotics did not stop the growth of *S. epidermidis* [87, 91]. For samples treated with LGS, when compared to LGS 24 h, gentamicin prevented the regrowth of biofilm by 50.3% at 31 µg/ml ($P = 0.36$), 87.2% at 62 µg/ml ($P = 0.08$), and 95.3% at 124 µg/ml ($P = 0.06$). However, when compared against their respective non-LGS-treated samples, the effects are more pronounced, with 80.8% ($P = 0.01$), 95.3% ($P < 0.001$), and 98.3% ($P = 0.0001$) reductions for antibiotic concentrations of 31, 62, and 124 µg/ml, respectively.

The 0 h negative control ($0\,h^-$, $n = 3$) had an absorbance of $0.0003 \pm 0.0002\,/mm^2$. Therefore, proteins in TSB did not adhere to the glass in sufficient quantities to confound the assay.

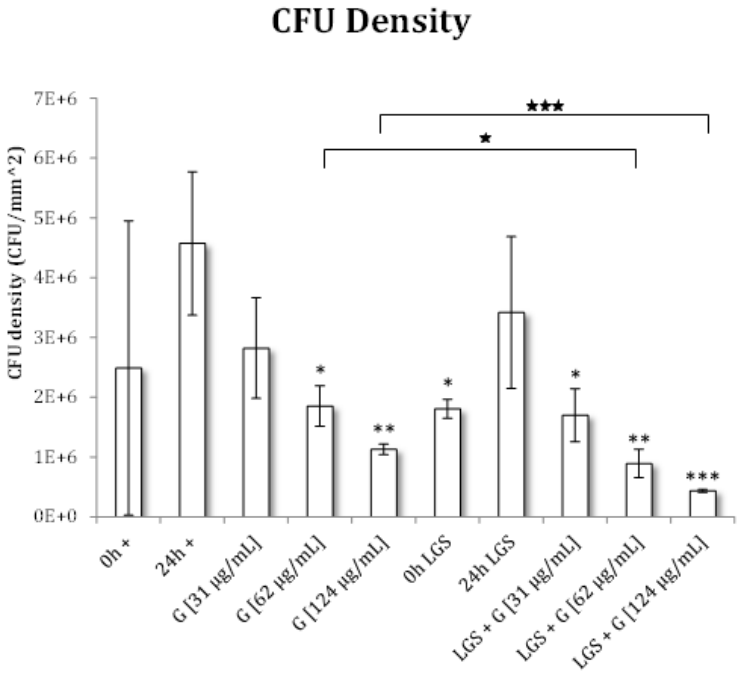

Figure 5.2: CFU density for *S. epidermidis* with LGS and gentamicin. Statistical significance was found using a 2-tailed t-test that compared each group to $0\,h^+$ ($*$) and $24\,h^+$ ($\bullet$). Pairwise comparisons were also made for gentamicin treatment with and without prior LGS treatment ($\bigstar$). Levels of significance are designated as follows: $> 5\%$ ($*$), $> 3\%$ ($**$), $> 1\%$ ($***$).

5.3.2 CFU Densities

Fig. 5.2 summarizes the CFU densities of the various treatments. With gentamicin therapy only, as compared to $24\,h^+$, we found a 38.3% ($P = 0.17$), 59.5% ($P = 0.037$), and 75.3% ($P = 0.02$) reduction in CFU density for gentamicin concentrations of 31, 62, 124 µg/ml, respectively. Conversely, LGS-treated samples, when compared to $24\,h^+$, saw a reduction in CFU density of 25.3% ($P = 0.40$), 62.9% ($P = 0.03$), 80.5% ($P = 0.01$), and 90.5% ($P = 0.008$), for LGS-treated samples: $24\,h^+$ LGS, LGS+G[31 µg/ml], LGS+G[62 µg/ml], LGS+G[124 µg/ml], respectively. Furthermore, in LGS-treated samples, when compared against their respective non-LGS-treated samples, we found reductions in CFU density of 39.8% ($P = 0.17$), 51.9% ($P = 0.03$), and 61.6% ($P = 0.0004$) for gentamicin concentrations of 31, 62, and 124 µg/ml, respectively.

5.3.3 Analysis of LGS Therapy Effect on Gentamicin Therapy

Biofilm bioburden

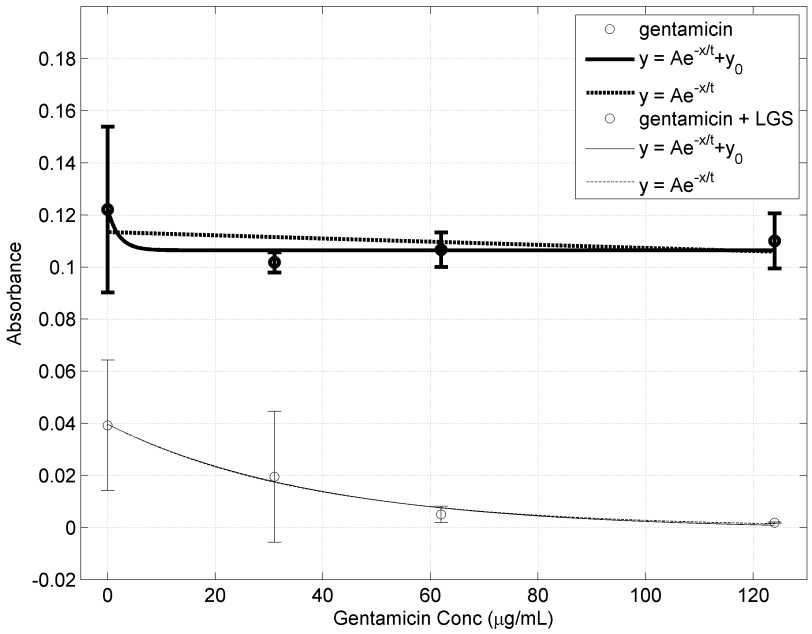

Figure 5.3: Biofilm burden (OD_{600}) at different gentamicin concentration with (unbold) and without (bold) prior LGS treatment. Bars represent sample standard deviation of the group. Both data sets were fitted to the exponential equation with offset: $y = Ae^{-x/t} + y_0$ and without offset: $y = Ae^{-x/t}$.

When the non-LGS-treated biofilm bioburden data were fitted to an exponential decay without offset, the coefficients with their corresponding standard errors were found to be:

$A : 0.1135 \pm 0.0077$

$t : 1806.6426 \pm 3225.6152\,\mathrm{ml/\mu g}$

$AdjR^2 = 0.30225$

Similarly, the coefficients with standard error for the LGS-treated biofilm bioburden data

set were found to be:

$A : 0.0397 \pm 0.0024$

$t : 37.5427 \pm 5.0318\,\mathrm{ml/\mu g}$

$AdjR^2 = 0.98003$

When the LGS-treated fit was compared to the non-LGS-treated fit, it was found that A, which represents the initial biofilm bioburden, decreased by 65.1% ($P < 0.0001$) and t decreased by 97.9% ($P > 0.05$), where t represents the effectiveness of increasing gentamicin concentration to lower the bioburden to a steady state, represented as 0 in this fit. The exponential fits here suggest that LGS significantly lowers the initial biofilm bioburden enough that subsequent gentamicin therapy can prevent further proliferation of the biofilm (Fig. 5.3).

When the non-LGS biofilm bioburden data were fitted to an exponential decay with offset, the coefficients were found to be:

$y_0 : 0.1078 \pm 0.0049$

$A : 0.0120 \pm 0.0085$

$t : 0.6559 \times 10^{18} \pm 3.286\,38 \times 10^{18}\,\mathrm{ml/\mu g}$

$A + y_0 : 0.1198$

$AdjR^2 : 0.36386$

Similarly, the coefficients for the LGS data were found to be:

$y_0 : -9 \times 10^{-4} \pm 0.0048$

$A : 0.0405 \pm 0.0055$

$t : 39.4830 \pm 13.2294\,\mathrm{ml/\mu g}$

$A + y_0 : 0.0396$

$AdjR^2 : 0.96156$

When the biofilm bioburdens of LGS-treated samples were compared to those of the non-LGS-treated samples, it was found that y_0, which signifies the offset or the steady state of the curve, decreased by 100.8% ($P > 0.0001$), A increased by 238.1% ($P < 0.005$), t increased by 592.0% ($P > 0.05$),where t represents the effectiveness of increasing gentamicin concentration to lower the bioburden to the steady state, represented by y_0 in this fit. The initial biofilm bioburden, represented by $A + y_0$, saw a decrease by 66.9%, which suggests that LGS is able to remove a significant portion of biofilm before gentamicin treatment. Furthermore, the large decrease in y_0, to the point where, the coefficient for LGS data was very close to 0, shows that the combination of LGS with gentamicin therapy can significantly lower the bioburden, whereas the gentamicin therapy alone had little effect on the bioburden. The low t in the non-LGS fit does not represent better antibiotic effectiveness, but rather in the context of a relatively high y_0, demonstrates a poor effectiveness of gentamicin to remove the biofilm, as increasing gentamicin concentration had little effect on the biofilm.

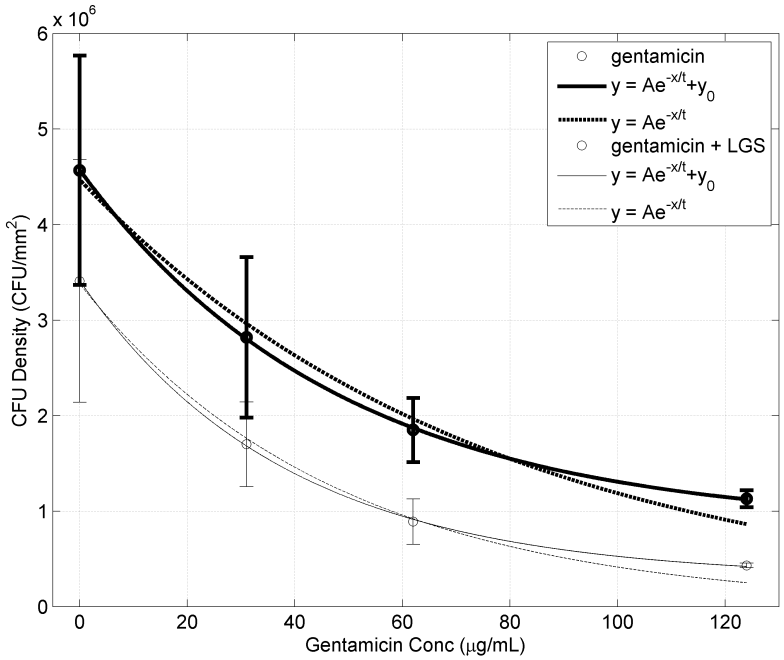

Figure 5.4: CFU density at different gentamicin concentration with (unbold) and without (bold) prior LGS treatment. Bars represent sample standard deviation of the group. Both data sets were fitted to the exponential equation with offset: $y = Ae^{-x/t} + y_0$ and without offset: $y = Ae^{-x/t}$.

CFU Densities

The coefficients with standard error when fitted to exponential decay without offset for non-LGS-treated CFU density data were found to be:

$A : 4.4706 \times 10^6 \pm 0.2236 \times 10^6\,\mathrm{CFU/mm^2}$

$t : 75.6084 \pm 8.8429\,\mathrm{ml/\mu g}$

$AdjR^2 : 0.97421$

Coefficients with standard error for LGS-treated set were found to be:

$A : 3.3824 \times 10^6 \pm 0.1379 \times 10^6\,\mathrm{CFU/mm^2}$

$t : 47.7258 \pm 4.2931\,\mathrm{ml/\mu g}$

$AdjR^2 : 0.98835$

When the LGS-treated fit was compared to the non-LGS-treated fit, it was found that A decreased by 24.3% ($P < 0.0001$), and t decreased by 36.9% ($P < 0.005$). As A signifies the initial concentration of bacteria, a decrease in A suggests that LGS treatment reduces the initial concentration of bacteria prior to gentamicin treatment. This can be seen in Fig. 5.4. Furthermore, as t represents the effectiveness of gentamicin, with lower values indicating less gentamicin is needed, that is, better effectiveness.

When the non-LGS-treated set was fitted to an exponential decay with offset, the coefficients were found to be:

$$y_0 : 8.3598 \times 10^5 \pm 0.4877 \times 10^5 \,\mathrm{CFU/mm^2}$$
$$A : 3.7384 \times 10^6 \pm 0.0512 \times 10^6 \,\mathrm{CFU/mm^2}$$
$$t : 48.2373 \pm 1.5998 \,\mathrm{ml/\mu g}$$
$$A + y_0 : 4.5744 \times 10^6 \,\mathrm{CFU/mm^2}$$
$$AdjR^2 : 0.99967$$

Similarly, the coefficients for the LGS-treated set was found to be:

$$y_0 : 3.0624 \times 10^5 \pm 0.4218 \times 10^5 \,\mathrm{CFU/mm^2}$$
$$A : 3.1112 \times 10^6 \pm 0.0490 \times 10^6 \,\mathrm{CFU/mm^2}$$
$$t : 37.9213 \pm 1.4898 \,\mathrm{ml/\mu g}$$
$$A + y_0 : 3.4175 \times 10^6 \,\mathrm{CFU/mm^2}$$
$$AdjR^2 : 0.99945$$

When the LGS-treated fit was compared to the non- LGS-treated fit, it was found that y_0 decreased by 63.4%, A decreased by 16.8%, t decreased by 21.4%, and $A + y_0$ decreased by 25.3% (all $P < 0.0001$). For exponential decay with offset, the initial concentration of bacteria is represented by $A + y_0$. Similarly the decrease in its value for the LGS-treated group, suggests that LGS treatment reduces the initial concentration of bacteria prior to gentamicin treatment. This can be seen in Fig. 5.4. As before, a decrease in t signifies an

increase in the effectiveness of gentamicin. As seen in both mathematical models, there was a decrease in initial bacterial counts and an increase in susceptibility to gentamicin.

5.4 Discussion

The results shown here demonstrate that LGS is effective at removing biofilm *in vitro* and can help improve the effectiveness of gentamicin activity against *S. epidermidis* biofilm. In ch 7, we will explore if this increase in effectiveness is simply due to the fracturing of the biofilm seen in ch. 3, or there is a secondary mechanism causing the cells to be more susceptible to gentamicin.

The results further gives emphasis that gentamicin alone cannot remove biofilm from a surface. A mechanical treatment, such as LGS, is needed first to remove the biofilm, and a follow up therapy with gentamicin can slow or even halt the regrowth of biofilm. As for CFU density, the results are not as striking. This suggests that there is still a large population of *S. epidermidis* cells adhered to the surface. This may be a limitation in the technology, where the shockwave is not breaking the biofilm at the biofilm-glass interface, but rather further into the biofilm, leaving a thin film. It may also be that one treatment of LGS may not be enough to remove the surface bacteria and another scan is needed. Clinically, this is not a problem, as it takes $< 20\,\mathrm{s}$ to scan the beam over a $3 \times 5\,\mathrm{cm}^2$ area. This may also be a limitation in the study, as only one side of the glass coverslip is treated with LGS. As the glass coverslip and the bottom of the well are optically flat, good contact was made between the two and no biofilm visible, even after the 3 day growing period. However, it may be possible that bacteria is still able colonize the surface in large quantities without producing visible biofilm. Therefore, a revised study would need to address this issue, either by treating the opposite with LGS, or develop a method to localize the analysis to only one side of the coverslip.

CHAPTER 6

Effect of Nd:YAG Spot Size and Coupling Gel Thickness on LGS Peak Pressure

6.1 Introduction

In this chapter, we will tabulate the changes in peak pressures when two important parameters are varied: thickness of the coupling gel (ultrasound gel) and spot size of the Nd:YAG laser. In a clinical and pre-clinical setting, the ultrasound gel will be applied manually and this will generate variances in the amount of gel applied. Furthermore, this is complicated by the fact that the treatment area and wounds are contoured, either due to crevices in the wounds or simply the morphology of the patient anatomy. Therefore, it is not inconceivable that the thicknesses can vary from 0.5 to as much as 3 mm. As the speed of sound through ultrasound gel is $\sim 1500\,\mathrm{m/s}$ [92, 93, 94] and the frequency of our shockwaves is in the 100 MHz - 1 GHz range, the wavelength of our shockwaves is in the low micron range. Therefore, small increases in the thicknesses of the ultrasound gel can greatly affect the peak pressures of the transmitted shockwaves. In the second half of the chapter, we will investigate how the spot size can affect the peak pressures of the generated shockwaves. This provides two benefits, first it allows us to reach higher energy densities than was previously tested, and if a lower energy density is desired, a larger spot size can be used, which would help speed up raster scanning times. The second benefit is this keeps the pulse width the same, as previously Francis *et al.* have shown that the pulse width of the Nd:YAG laser increases as the laser fluence is decreased [76].

6.2 Methods

Peak pressures of the shockwaves were measured using the displacement interferometer described in Navarro's work[4]. The procedures are summarized below.

6.2.1 Displacement Interferometer Setup

A frequency-stabilized 632.8 nm HeNe laser (Melles Griot, Carlsbad, CA) was split into 2 beams using a 50/50 beam splitter. One beam was used as a reference beam and was reflected back using a fixed mirror. The other beam was used as the sample beam and was reflected back using the mirrored surface of the sample. The reflected beams were recombined using the same 50/50 beam splitter and focused onto a high-speed (30 ps rise time) 9 V reverse-biased photodiode. The signal from the photodiode was passed through a bias tee, filtering out the 9 V bias and any other DC components. The signal was then amplified through two 20 dB low noise amplifiers and captured on a 2.25 GHz digital oscilloscope (WaveSurfer, Teledyne LeCroy, NY, USA). The captured waveform was then uploaded to MatLAB (Mathworks, MA, USA) for further analysis. The interferometer setup can be seen in fig. 6.1.

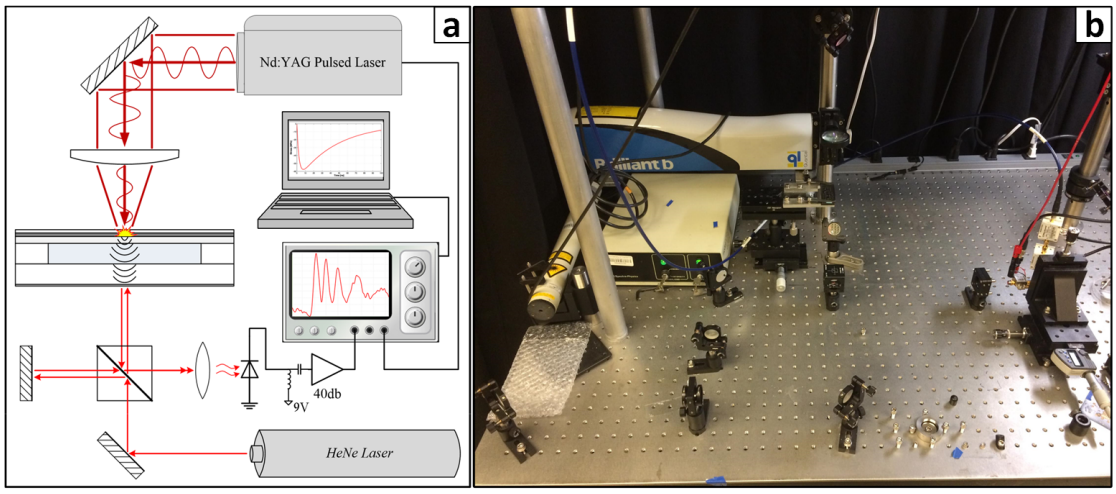

Figure 6.1: Setup of Displacement Interferometer based on the Michelson Interferometer. a)Diagram of interferometer and sample setup. b) Actual interferometer setup.

6.2.2 LGS Sample Setup for Interferometry Measurements

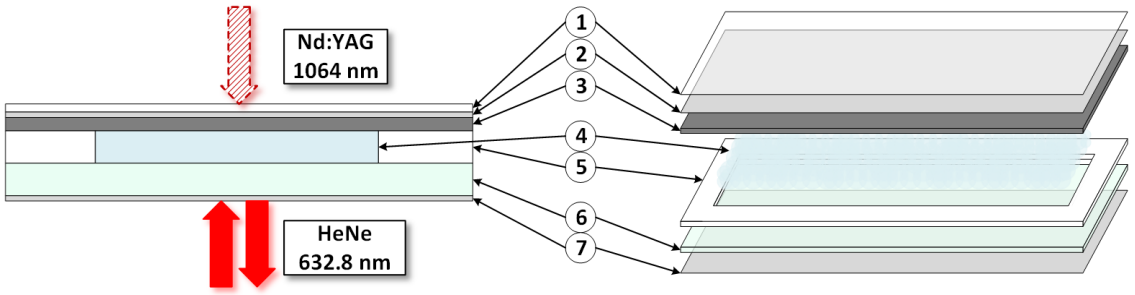

Figure 6.2: Setup of LGS sample for peak pressure measurement (not to scale). **1.** 0.5 µm thick waterglass. **2.** 500 nm thick sputtered titanium. **3.** 0.0254 mm thick polyimide for Nd:YAG spot size or 1 mm soda lime microscope glass for coupling gel thickness. **4.** Ultrasound gel (thickness set by acrylic spacer). **5.** Acrylic spacer (1.0 mm for Nd:YAG spot size. 0.57, 1.10, 1.61, 2.14, and 3.22 mm for coupling gel thickness). **6.** 1 mm soda lime microscope glass. **7.** 50 nm sputtered aluminum.

Due to the need of a flat reflective surface on the sample to reflect the sampling arm of the interferometer, it is not possible to take direct measurements on biological samples. Therefore, a mechanical model was used in this study, which has been reproduced in fig. 6.2. A 1 mm soda lime microscope glass slide (6) was used to measure the stress that would be experienced by the sample under LGS treatment. Soda lime glass was used due to its material properties (i.e. speed of sound and material stiffness) being well-documented and its ability to withstand RF-sputtering, which is needed to create a reflective surface. One side of the glass was RF-sputter coated with 50 nm of Aluminum (7). This thickness is sufficient to reflect the HeNe, without affecting the shockwave, as the thickness is smaller than the expected wavelength of the shockwave[4].

An acrylic spacer (5) is placed on top of the non-metalized side of the microscope glass side to ensure the ultrasound gel (4) thickness is consistent between experiments. The thicknesses used were 1 mm for measurements of peak pressure with different Nd:YAG spot sizes. As for measurements at different ultrasound gel thicknesses, the thicknesses used were 0.57, 1.10, 1.61, 2.14, and 3.22 mm.

After applying the ultrasound gel to the space left by the spacer and ensuring there were no trapped air bubbles, the LGS substrate was placed on top, once again ensuring no air

bubbles were trapped. The LGS substrate composed of three layers. The bottom layer is a supportive material (3) that provides rigidity to the LGS substrate. The middle layer is an ablative material,500 nm thick layer titanium (Ti) (2), that was RF-sputter coated to one side of the supportive material. This is the layer that gets ablated during the generation shockwave. Immediately before the experiment, the final layer, 0.5 µm thick layer of waterglass (1), was manually applied to the Ti. This layer causes the generated shockwave to reflect back into the LGS substrate, increasing the peak pressure that is delivered to the sample.

As the goal of the study was to understand the relative trends of ultrasound gel thickness and Nd:YAG spot size on peak pressure, 1 mm soda lime glass microscope slides was chosen as the supportive material since it has been shown that the pressures generated on this material are more uniform from shockwave to shockwave [76]. This is especially important for ultrasound gel thickness, as the flexible nature of the 0.0254 mm polyimide, makes it very difficult to ensure high precision of the thickness of the ultrasound gel.

6.2.3 Generation of Laser Generated Shockwaves and Data Capture

The HeNe and Nd:YAG lasers were positioned, so that they will be co-linear, but anti-parallel, upon reaching the LGS substrate. The oscilloscope was used in single shot mode and set to trigger 200 ns after the Q-switch trigger is fired.

Ultrasound Gel Thickness

In order to investigate the effects of coupling gel thickness, a single 1064 nm Nd:YAG pulse, at 777.9 mJ with pulse width of 8 ns and spot size diameter of 3 mm, was used to ablate the confined Ti layer. After the shockwave passes through a 0.57 mm layer thick ultrasound gel, the resultant displacement of the mirrored glass slide generates a signal in the interferometer that is captured by the oscilloscope. This was repeated five more times with unablated portions of the LGS sample for a total of six waveforms. The Nd:YAG Q-switch delay was then raised to 275, 300, 325, 350, and 400 µs, which correspond to laser energies: 660.9,

588.1, 455.9, and 318.1 mJ, respectively, and the measurements were repeated. This was then repeated with 1.10, 1.61 2.135, and 3.22 mm thick layer ultrasound gel, for a total of 36 waveforms per ultrasound gel thickness.

Nd:YAG Spot Size

In order to investigate the effects of Nd:YAG spot sizes and the resultant laser energy densities on the peak pressures, a single 1064 nm Nd:YAG pulse, at 777.9 mJ, pulse width of 8 ns, and spot size diameter of 1.6 mm was used to generate a shockwave. After the shockwave passes through a 1.0 mm layer thick ultrasound gel, the resultant displacement of the mirrored glass surface was once again measured as before. This was repeated five more times, using unablated portions of the LGS samples each time. The laser energy was then changed to: 660.9, 588.1, 455.9, and 318.1 mJ and the measurements were repeated.

Two additional experiments were performed regarding Nd:YAG spot sizes. In the first experiment, the thickness of the Ti layer was increased from 500 nm to 1 µm. This was because in the initial results, it was found that peak pressure decreases as spot size diameter decreases from 3.0 mm to 2.2 mm, despite the laser energy density doubling. Therefore, to investigate if this decrease was a result of insufficient ablative material causing there to be unused laser energy, the peak pressures were measured for Nd:YAG spot sizes with diameters of 3.0 and 2.2 mm using the highest laser energy of 771.9 mJ. Finally, as a follow up for future animal studies, the peak pressures were measured using the same setup, but the supportive material was switched with 0.0254 mm black polyimide, as this will be the supportive material that will be ultimately used for pre-clinical work for its flexibility. Measurements were made using spot sizes with 4.2, 3.0, and 2.2 mm, all using the a laser energy of 771.9 mJ.

6.2.4 MatLAB Calculation of Peak Pressure from Displacement Interferograms

The work previously done by Gupta, demonstrated that shockwaves produced through laser ablation of metal under confinement produced a purely compressive wave, which causes the surface opposite to the shockwave generation site to deform plastically in the direction of the

compressive wave[4]. This is represented in the interferometry waveform as a down-chirped waveform, as the surface accelerates and decelerates from the deformation. Each peak to trough correlates to a movement of a quarter of a wavelength of the 632.8 nm HeNe laser, which corresponds to a complete transition from constructive to destructive interference of the HeNe laser on the photodiode. This chirped signal can be modeled by the chirped signal equation below, as a function of free surface displacement, $u_0(t)$:

$$A_0(t) = \frac{A_{max}+A_{min}}{2} + \frac{A_{max}-A_{min}}{2} sin(\frac{4\pi}{\lambda} u_0(t) + \delta)$$

A_{max} and A_{min} are the global maximum and minimum fringe amplitudes, respectively. λ is the wavelength of the frequency stabilized HeNe laser (632.8 nm) and δ is the phase angle in radians. By measuring the time between each peak and valley, we can graph the displacement as a function of time and calculate the velocity of the surface deformation. As the time points are discrete, a fitting algorithm is used to define the displacement and velocity profile over the period of surface acceleration and deceleration. Previously, Gupta *et al.* [69, 67] have shown that this displacement, $u_0(t)$, and velocity, $v_0(t)$, of the free surfaces can be expressed as the following equations:

$$u_0(t) = \gamma\Big\{ -\alpha\Big[e^{-t/\alpha} - 1\Big] + \beta\Big[e^{-t/\beta} - 1\Big]\Big\}$$
$$v_0(t) = \gamma\Big\{\alpha e^{-t/\alpha} + \beta e^{-t/\beta}\Big\}$$

where u_0 and v_0 represent the free surface displacement and velocity, respectively, t is time, and α, β, and γ are scaling coefficients to fit the function to the measured displacement vs time data. Fitting was accomplished using the damped least-squares method in OriginPro software. Once the fitting coefficients have been obtained, $v_0(t)$ can be found by taking the derivative of $u_0(t)$.

$$\sigma = -\frac{1}{2}\rho c v_0(t)$$

where σ is the shockwave stress within the material, c is the speed of sound through the material, and ρ is the material density[69, 67]. Once the stress profile is obtained, we record the peak stress value This procedure is reproduced as a flow diagram in fig. 6.3.

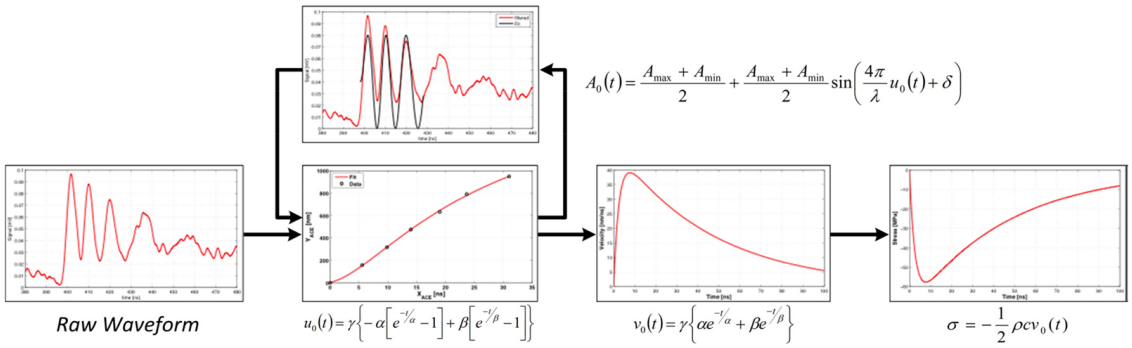

Figure 6.3: Work flow for MatLab script to calculate stress over time from the raw waveform. Adapted from *Francist et al. 2015* [76]

6.3 Results

6.3.1 Coupling thickness

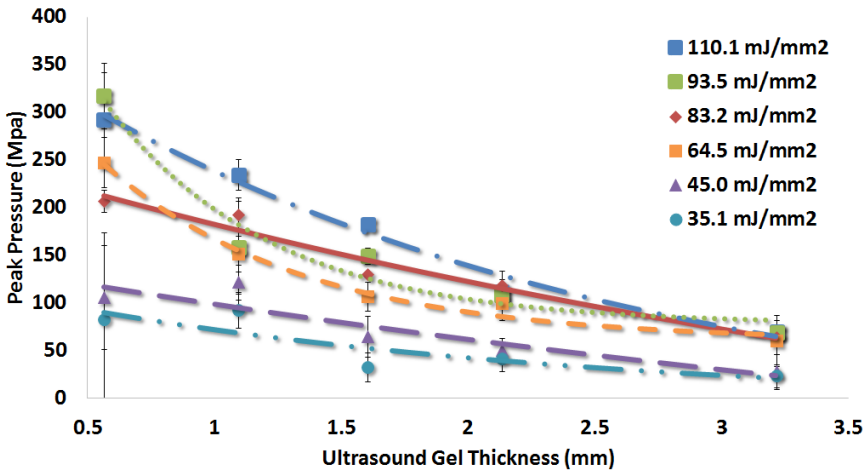

Figure 6.4: Peak pressure at various coupling gel thickness depths. Data fitted to $y = c + be^{-ax}$

For each Nd:YAG energy density, six peak pressures were measured and then averaged for each ultrasound gel thickness: 0.57, 1.10, 1.61, 2.14, and 3.22 mm. This was repeated for all six energy densities: 35.1, 45.0, 64.5, 83.2, 93.5, 110.1 mJ/mm^2. The average peak pressure, along with the sample standard deviation, can be seen in fig. 6.4. In general, we see a decrease in peak pressures, as the thickness of the ultrasound gel increase. This was to be expected as the shockwave disperse and is absorbed by the ultrasound gel as it passes through.

The full data is presented in Table 6.1. We will focus primarily on the peak pressures obtained at an energy density of 110.1 mJ/mm^2, as the future studies will primarily use the same energy fluence of 777.9 mJ. When the thickness of the ultrasound gel was at 1.10 mm, the peak pressure was found to be 234.1 ± 16.0 MPa. However, the thickness was reduced to 0.57 mm the peak pressure increased by 24.8% to 292.2 ± 49.0 MPa. When the thickness was increased to 1.61 mm, the peak pressure decreased by 22.4% to 181.7 ± 6.5 MPa. As it is not unreasonable to assume that the application of the ultrasound gel in the clinical setting can deviate by ± 0.5 mm, it is important to note that peak pressures can differ up to 60%. This will have implications in future safety and efficacy studies. Finally, at a thickness of > 3 mm, it seems that the pressures from the four highest energy densities converge to a single point, while the last two energy density converge to another lower point. This difference may be a result in the pulse width, when the energy fluence is changed, as seen in Francis *et al.*[76]. At this thickness the pressures are assumed to be negligible. This has significant implications. If we assume that tissue has similar acoustic characteristic as ultrasound gel, the shockwave energy will rapidly decay, delivering the most energy at the surface of the wounds, where the most bacteria is found. The low penetration of the shockwaves will actually work to our advantage in this application.

Peak Pressures using a Polyimide-based LGS substrate

The peak pressures from 6 shockwaves, generated from laser ablation of titanium on polyimide, were recorded for each Nd:YAG spot size: 1.6, 2.2, 3.0 and 4.2 mm. Using a laser fluence of 777.9 mJ, we achieved energy densities of: 386.9, 204.6, 110.1, and 56.1 mJ/mm^2, respectively. This corresponded to peak pressures of: $116.7 \pm 21.8, 118.0 \pm 18.3, 295.7 \pm 35.4$, and 227.0 ± 58.0 MPa, respectively. As the peak pressures drop off sharply at spot sizes smaller than 3.0 mm, this suggest that there is a secondary mechanism, on top of the Nd:YAG energy density, present that affects the peak pressures.

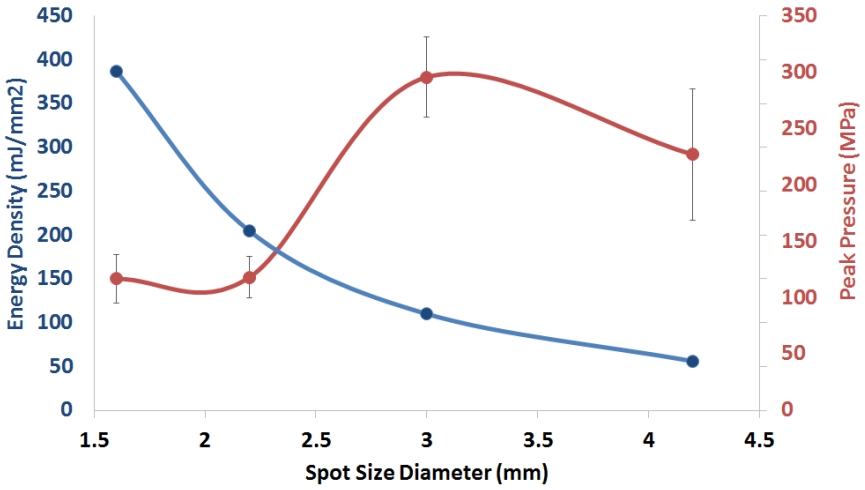

Figure 6.5: Relationship of spot size in regards to peak pressures and energy density with a Nd:YAG laser fluence of 777.9 mJ. Relationship between energy density and Nd:YAG spot size show an exponential decay (blue). Relationship between peak pressure and spot show a different curve (red), with the highest pressure measured at 3 mm and lowest pressures at 1.6 and 2.2 mm.

6.3.2 Nd:YAG Spot Size

Peak Pressures using a Soda Lime Glass-based LGS substrate

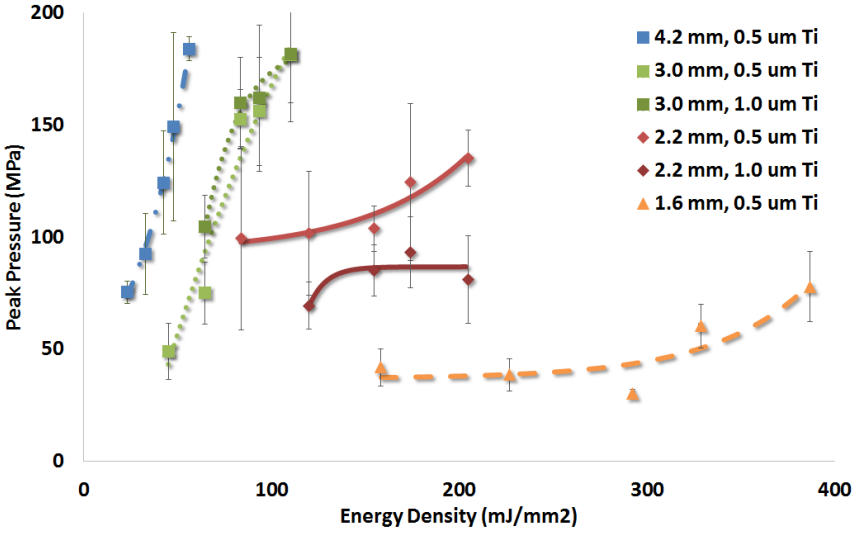

Figure 6.6: Peak pressure at various energy densities from different spot sizes. Data fitted to $y = c + be^{-ax}$

To investigate what is this secondary mechanism, the study was repeated, with a 1 mm borosilicate glass slide replacing the underlying polyimide substrate, as it has been shown

previously that underlying glass supportive substrates produce comparable peak pressures, but with lower variabilities[76]. Using a the same Nd:YAG laser fluence of 777.9 mJ, average peak pressures of $77.9 \pm 15.7, 135.3 \pm 12.6, 181.3 \pm 21.2$, and 184.0 ± 5.4 MPa, for spot sizes 1.6, 2.2. 3.0, and 4.2 mm, respectively. This trend mirrors closely to what was observed with a underlying polyimide supportive substrate, which confirms our initial assumption that the secondary mechanism is not substrate related.

To investigate if at the higher energy densities the titanium is ablating before the full absorption of the laser energy, peak pressures were once again measured at lower energy fluences: $660.9, 588.1, 455.9$, and 318.1 mJ, for each of the spot sizes. The average peak pressures for each is summarized in Table. 6.2. This effect, known as plasma shielding, occurs when the titanium ablates before full absorption of the Nd:YAG laser. Once the metal ablates, it generates a cloud of plasma that is opaque to the 1064 nm light, shielding the remaining titanium from absorbing any laser energy[95, 96]. As seen in fig. 6.6, when the laser fluence is decreased for spot size 2.2 mm, the peak pressure continues to decrease monotonically, despite the laser energy densities beginning to overlap the energy densities used in the 3.0 mm investigations. This would suggest that plasma shielding is not occurring in this situation, as we should be below the threshold once we achieved similar energy densities. This is supported by the peak pressures measured using a 1.6 mm spot size, where peak pressures continued to decrease monotonically with energy fluence.

Finally to investigate if the peak pressures dropped because there was simply less material to ablate at the smaller spot sizes or some of the laser energy is bleeding through, we increased the thickness of the titanium from 500 nm to 1.0 µm and re-measured the peak pressures for the 2.2 and 3.0 mm spot sizes, at laser fluences of $318.1, 455.9, 588.1$, and 777.9 mJ. The peak pressures are summarized in table 6.2. As seen in fig. 6.6, There isn't an increase in peak pressures for either spot sizes. This would suggest that initial hypothesis is false and the primary mechanism may be a result of the spot size itself rather than the laser energy density.

Underlying Substrate	Titanium Thickness	Ultrasound Gel Thickness	Spot Size	Energy Fluence	Peak Pressure
1 mm Borosilicate	0.5 µm	0.57 mm	3.0 mm	248.1 mJ	82.6 ± 91.4 MPa
				318.1 mJ	105.7 ± 54.8 MPa
				455.9 mJ	247.2 ± 26.5 MPa
				588.1 mJ	207.7 ± 11.8 MPa
				660.9 mJ	316.7 ± 34.4 MPa
				777.9 mJ	292.2 ± 49.0 MPa
		1.10 mm	3.0 mm	248.1 mJ	92.3 ± 18.5 MPa
				318.1 mJ	121.5 ± 18.2 MPa
				455.9 mJ	151.1 ± 19.0 MPa
				588.1 mJ	192.8 ± 17.8 MPa
				660.9 mJ	158.1 ± 49.1 MPa
				777.9 mJ	234.1 ± 16.0 MPa
		1.61 mm	3.0 mm	248.1 mJ	32.1 ± 15.2 MPa
				318.1 mJ	65.0 ± 21.5 MPa
				455.9 mJ	106.4 ± 15.4 MPa
				588.1 mJ	129.9 ± 2.5 MPa
				660.9 mJ	148.9 ± 8.7 MPa
				777.9 mJ	181.7 ± 6.5 MPa
		2.14 mm	3.0 mm	248.1 mJ	41.4 ± 13.4 MPa
				318.1 mJ	50.1 ± 12.9 MPa
				455.9 mJ	99.8 ± 13.5 MPa
				588.1 mJ	118.2 ± 1.4 MPa
				660.9 mJ	107.8 ± 26.0 MPa
				777.9 mJ	111.3 ± 13.5 MPa
		3.22 mm	3.0 mm	248.1 mJ	23.2 ± 12.1 MPa
				318.1 mJ	27.7 ± 18.2 MPa
				455.9 mJ	60.3 ± 27.7 MPa
				588.1 mJ	63.7 ± 17.8 MPa
				660.9 mJ	68.7 ± 6.6 MPa
				777.9 mJ	70.0 ± 2.5 MPa

Table 6.1: Table of peak pressures generated from the ablation of Titanium using a 1064 nm Nd:YAG laser for the investigation of the impacts of ultrasound gel thickness on peak pressure.

Underlying Substrate	Titanium Thickness	Ultrasound Gel Thickness	Spot Size	Energy Fluence	Peak Pressure
1 mm Borosilicate	0.5 µm	1.0 mm	1.6 mm	318.1 mJ	41.9 ± 8.2 MPa
				455.9 mJ	226.8 ± 38.6 MPa
				588.1 mJ	292.5 ± 30.4 MPa
				660.9 mJ	328.7 ± 60.4 MPa
				777.9 mJ	387.1 ± 77.9 MPa
			2.2 mm	318.1 mJ	99.5 ± 40.7 MPa
				455.9 mJ	101.6 ± 27.6 MPa
				588.1 mJ	103.8 ± 10.1 MPa
				660.9 mJ	124.7 ± 35.0 MPa
				777.9 mJ	135.3 ± 12.6 MPa
			3.0 mm	318.1 mJ	49.0 ± 12.5 MPa
				455.9 mJ	75.1 ± 13.7 MPa
				588.1 mJ	152.6 ± 13.3 MPa
				660.9 mJ	156.2 ± 24.0 MPa
				777.9 mJ	181.3 ± 21.2 MPa
			4.2 mm	318.1 mJ	75.5 ± 5.0 MPa
				455.9 mJ	92.7 ± 18.1 MPa
				588.1 mJ	124.4 ± 23.0 MPa
				660.9 mJ	149.2 ± 42.0 MPa
				777.9 mJ	184.0 ± 5.4 MPa
	1.0 µm	1.0 mm	2.2 mm	455.9 mJ	69.5 ± 10.4 MPa
				588.1 mJ	85.1 ± 11.5 MPa
				660.9 mJ	93.4 ± 15.9 MPa
				777.9 mJ	81.1 ± 19.6 MPa
			3.0 mm	455.9 mJ	104.6 ± 14.0 MPa
				588.1 mJ	160.0 ± 20.4 MPa
				660.9 mJ	162.0 ± 32.5 MPa
				777.9 mJ	181.6 ± 30.0 MPa
25.4 µm polyimide	0.5 µm	1.0 mm	1.6 mm	318.1 mJ	116.7 ± 21.8 MPa
			2.2 mm	318.1 mJ	118.0 ± 18.3 MPa
			3.0 mm	318.1 mJ	295.7 ± 35.4 MPa
			4.2 mm	318.1 mJ	227.0 ± 58.0 MPa

Table 6.2: Table of peak pressures generated from the ablation of Titanium using a 1064 nm Nd:YAG laser for the investigation of the impacts of ultrasound gel thickness on peak pressure.

6.4 Discussion

As seen from the results, the peak pressure greatly depends not only on the laser fluence, but also the spot size of the Nd:YAG laser and ultrasound gel thickness, as they can have large impacts on the final peak pressures. The drop in peak pressure, due to the ultrasound gel thickness, can be attributed to the attenuation of the shockwave by the gel, through absorption and dispersion. However, it is unknown how much absorption vs dispersion is occurring as it is difficult to measure the dispersal of the our shockwaves. Furthermore, it is difficult to find ultrasound transmitters capable of delivering the same high frequency bandwidth as LGS to study this further.

As for the drop in peak pressure due to the decrease in Nd:YAG spot size, despite a rise in Nd:YAG energy density, is currently unanswered by this work. As it does not seem to be a product of plasma shielding or the overloading of our LGS generating substrate, this may be a result of the spot size itself. One hypothesis is the spot size has become smaller than the effective wavelength of the generated shockwave, causing dispersal of the shockwave. This would mean that we have moved from a system that can be describe by a 1-D wave model to a 2-D one. However, more testing would be needed to be confirm this.

The soda lime glass labeled 7 in fig. 6.2, is our analog to biofilm, as it experiences the peak pressures after passing through the ultrasound gel. The rigidity of the glass allows us to accurately measure the peak pressures it experiences. However, glass doesn't have the same material properties as biological tissue, which causes a lot of the energy to be reflected off the ultrasound gel and glass interface. However, due to the similarities in material properties of biofilm and tissue, much of the reported pressure will not be reflected at the biofilm-tissue interface. Therefore, the goal is to increase the peak pressure as much as possible to maximize the amount of energy that is reflected. The upper limit will be determined by how well the tissue can tolerate these high pressures.

CHAPTER 7

Laser Generated Shockwaves Effects of Gentamicin on Planktonic Cells

7.1 Introduction

In this chapter, we will follow up on the results obtained in ch.5, by investigating the mechanism behind the increase in effectiveness of gentamicin against *S. epidermidis* cells in its biofilm state. Previously, we have shown that LGS can increase the bactericidal ability of gentamicin against biofilm. However, it is not clear if this increase in effectiveness is simply due to the fracturing of the biofilm, as seen under SEM in ch.3, or the shockwaves may also have an effect on the *S. epidermidis* cells themselves. Previously, it has been shown that a technique, called "sonoporation", can be used to permeabilize the membranes of bacteria cell, through the exposure of ultrasound[97, 98, 99]. If LGS can similarly permeabilize the cells, this may lead to an increase in gentamicin effectiveness, as this antibiotic works through the irreversible binding with the 30S bacterial ribosomal sub-unit. Therefore, gentamicin needs to penetrate the cell, in order to have an effect.

In this chapter, we investigate if the increase in gentamicin effectiveness can be observed in planktonic cells, where there are no biofilm present. This will be accomplished by exposing planktonic *S. epidermidis* cells to a single shockwave generated using Nd:YAG laser parameters: 3.0 mm spot size with energy fluence 777.9 mJ, in the presence of gentamicin. As seen in ch.6, the shockwave rapidly decays after traveling $\sim$ 3 mm through ultrasound gel. Therefore, care needs to be taken to maximize the amount of cells treated, in order to improve our detectable limit. This was accomplished by filling a 1.5 ml micro-centrifuge tube with agar, leaving $\sim$ 3 mm of head space to fill with the bacterial solution. This study will

investigate if LGS therapy can decrease the growth of *S. epidermidis* when combined with gentamicin therapy at concentrations lower than the minimum bactericidal concentration, 62.5 µg/ml[87].

7.2 Methods

7.2.1 *S. epidermidis* Solution Preparation

Staphylococcus epidermidis (ATCC 35984) cultures were streaked on a tryptic soy agar (TSA) plate for single colonies. The plate was then incubated at 37 °C overnight. A single colony was picked from the plate and inoculated into 25 ml sterile tryptic soy broth (TSB) in a 125 ml Erlenmeyer flask. This was further incubated at 37 °C, 200 rpm, for 18 h. The culture was centrifuged at 3.000 rpm for 5 min at 4 °C. The supernatant was discarded and the pellet was resuspended in 25 ml of TSB. A working *S. epidermidis* was prepared by dilution of the resuspended solution in fresh TSB, until an optical density of 0.2 at 600 nm (OD_{600}) was achieved. This correlated to a CFU density of 4×10^7 cells/mL.

7.2.2 Planktonic *S. epidermidis* Preparation

3 ml aliquots of the prepared *S. epidermidis* cells were added to 5×15 ml conical tubes. Each tube was supplemented with one of five gentamicin concentrations: 0, 8, 16, 32, and 64 µg/ml. Care was taken to ensure volume added to each tube was equal to ensure equal dilution of the cells. This was done by diluting the gentamicin first with PBS before adding to the cells.

7.2.3 Planktonic Cell LGS Setup

As seen in section 6.3.1, the pressure of the shockwave rapidly attenuates as it travels through the ultrasound gel. After more than 2 mm, the shockwave is attenuated by over 50%. Therefore simply treating a filled 1.5 ml micro-centrifuge tube will only treat cells in the top 2 mm, resulting in the vast majority cells not being treated. To ensure that the maximum per-

centage of cells are treated by LGS, the micro-centrifuge tube is first filled with 1.5 ml of non-sterile TSA, so that when filled to the top of the tube with ∼300 µL of the prepared *S. epidermidis* solution, the solution thickness is only ∼2 mm. A prepared 1 cm×1 cm polyimide LGS substrate was placed on each tube. Care was taken to ensure proper contact between the solution and the LGS substrate for proper coupling between the substrate and the solution. This was done for 20 tubes, four tubes per gentamicin concentration group, with two tubes from each group to be treated with LGS and gentamicin and two tubes with just gentamicin alone. LGS substrate was still placed on the gentamicin only samples, to ensure that any differences in the two treatment groups are due to LGS alone and not processing differences.

7.2.4 Preparation of Improved LGS Substrate

To protect the sample from the effects of potential laser-bleed through, the underlying plastic in the LGS substrate was switched from 0.1 mm polycarbonate to 0.0254 mm Electrically Conductive Kapton® polyimide film (McMaster-Carr, Chicago, IL), which is capable of fully absorbing 1064 nm Nd:YAG laser at 110.1 mJ/mm^2, preventing any laser bleed-through. Similarly as to how Titanium (Ti) coated polycarbonate was prepared, as described in section 3.2.3, in a Class 100 clean room, the polyimide film was first cleaned with acetone to remove any oil or debris. It was then dried with dry N_2 gas. The cleaned polyimide was then RF sputtered coated with 500 nm layer thick titanium (Ti), using the Discovery Denton Sputterer (Denton Vacuum, Moorestown, NJ). As before, the Ti-coated polyimide was wrapped in a clean room cloth until ready to be used.

Immediately before the LGS treatment, the Ti-coated polyimide was removed from the clean room cloth and cut to the desired size (1×1 cm^2, for this experiment). A thin layer (∼ 200 µm) of waterglass was applied to the Ti side of the polyimide manually and allowed to dry.

7.2.5 LGS Treatment of Planktonic Bacterial Cells

Samples to be treated with LGS were then mounted in a micro-centrifuge rack and a single shockwave was generated for each sample, with the following laser parameters: 1064 nm Nd:YAG laser, 3 mm spot size, and a energy density of 110.1 mJ/mm^2.

7.2.6 Spectrophotometer Analysis of LGS and Gentamicin on Planktonic *S. epidermidis*

Immediately after LGS treatment, 250 µl was removed from each tube and placed in a separate well on a sterile 96 well plate (BioTek, VT, USA), with Lid. Gentamicin only samples were also placed on the same well plate. After all treatments were finished, 100 µl was removed from each well and placed in a new well on the same plate. A TSB blank was also to the plate and the absorbance readings at 600 nm was obtained for each well, using the Synergy H1 Hybrid microplate reader (BioTek, VT, USA), to establish initial cell concentrations.

The plate was then incubated at 37 °C for 24 h and 100 µl was once again removed from the first set of wells and placed in a new well on the same plate. A new TSB blank was added and the absorbance readings at 600 nm was obtained in the same manner, to obtain the new cell concentrations. This was repeated four more times to obtain a sample size of 16 per group.

The data was aggregated on Excel (Microsoft, USA) and the averages and standard deviations of each group at the two time points were calculated and plotted.

7.3 Results

The absorbances for the *S. epidermidis* solutions after gentamicin treatment with and without adjunct LGS treatment are shown in Fig. 7.1, with the exact values listed in Table 7.1. Each treatment group had a sample size of 16. The similar initial absorbances between the treatment groups verifies that the differences observed at 24 h were not due to differences in

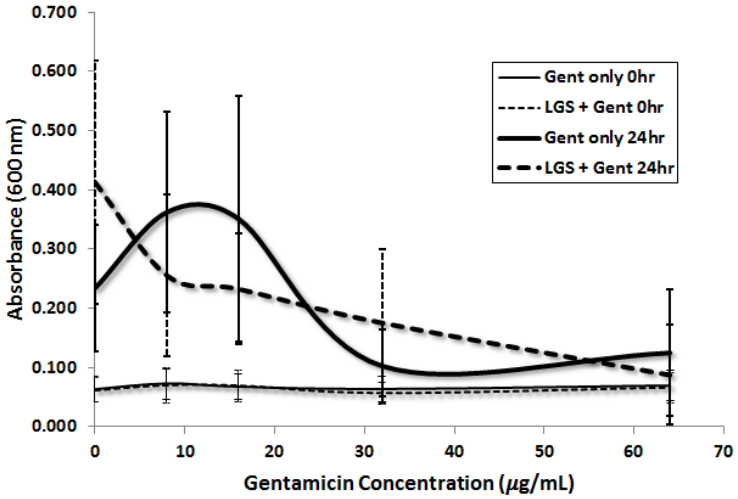

Figure 7.1: Laser generated shockwave treatment's effects on gentamicin against planktonic *S. epidermidis* cells. Absorbances (600 nm) were measured for *S. epidermidis* solutions treated with (dashed) and without (solid) LGS at different gentamicin concentrations. Measurements were taken immediately after LGS treatment (0 hr, unbold) and 24 hr (bold).

initial concentrations.

In general, after 24 h incubation, the samples with low concentrations of gentamicin (0, 8, and 16 µg/ml) had high absorbances, as these concentrations were below the MIC, 31.5 µg/ml, for gentamicin against *S. epidermidis*. It is unknown why 0 µg/ml gentamicin only had lower than expected absorbance values. Otherwise, for the gentamicin only samples, it appears that samples with gentamicin concentrations below the MIC, have consistently higher absorbance values. Once, the gentamicin concentration reached higher than the MIC (31.25 µg/ml), the absorbances dropped sharply, representing little growth of the bacteria. On the other hand, for the samples with adjunct LGS treatment, samples with low concentrations had higher absorbances, with the highest at 0 µl/ml. However, rather than the gentamicin having little effect at concentrations below the MIC, there appears to be a consistent drop with increase of gentamicin concentration. When comparing the gentamicin only absorbances at 24 h with the respective LGS treatment groups (e.g. 0 µg/ml vs. 0 µg/ml + LGS, 8 µg/ml vs 8 µg/ml + LGS, etc.), the percent differences were found to be: 76.4%, -29.5%, -33.6%, 71.2%, and -29.8% (all $p > 0.05$), respectively.

As concentrations of gentamicin above >10 µg/ml are considered to be nephrotoxic[40],

Sample group	0 h	24 h
0 µg/ml	0.063 ± 0.021	0.234 ± 0.107
8 µg/ml	0.072 ± 0.026	0.363 ± 0.169
16 µg/ml	0.067 ± 0.022	0.351 ± 0.208
32 µg/ml	0.063 ± 0.021	0.103 ± 0.061
64 µg/ml	0.069 ± 0.026	0.125 ± 0.108
0 µg/ml + LGS	0.062 ± 0.021	0.125 ± 0.108
8 µg/ml + LGS	0.070 ± 0.029	0.256 ± 0.137
16 µg/ml + LGS	0.069 ± 0.026	0.233 ± 0.094
32 µg/ml + LGS	0.057 ± 0.019	0.176 ± 0.125
64 µg/ml + LGS	0.066 ± 0.025	0.088 ± 0.085

Table 7.1: Absorbance measurements at 600 nm for *S. epidermidis* solutions treated with different concentrations of gentamicin and with and without adjunct LGS treatment.

the ability of LGS to improve the effectiveness of low concentrations of gentamicin may be critical.

7.4 Discussion

From the results, there appear to be a small decrease in bacterial growth at the lower gentamicin concentrations (8 and 16 µg/ml, when combined with LGS treatment. However, the results are not conclusive, as the standard deviations for all groups were very large. This may be a result of the effects being too small, gentamicin effects being too variable, or the technique not precise enough. Therefore in the following chapter, we will explore different techniques to try to directly measure if permeabilization is occurring.

CHAPTER 8

Evidence of LGS Cell Permeabilization to Explain Potentiation of Gentamicin

8.1 Introduction

This chapter will further investigate if there are evidence for permeabilizations of the bacterial cell after LGS treatment. As discussed in ch 5, gentamicin is an aminoglycoside antibiotic, whose mechanism relies on inhibition of protein synthesis, through the irreversible binding of the 30S subunit of bacterial ribosomes. Therefore, an increase in cell permeability would allow more gentamicin to enter the cell and inactive more ribosomes.

In this study, we will try to investigate if LGS can permeabilize *S. epidermids* planktonic cells. As this is the first time we have attempted to measure the direct effects of LGS on bacteria cells, we have tried many different approaches to address this aim. This chapter will cover the three different approaches used to examine if permeabilization of the bacteria cell by LGS was present. In the first, we used spectrophotometry to determine if we could detect protein and DNA leakage, using chemicals. In the second approach, we investigated if fluorescein can be detected in cells that were exposed to LGS in the presence of fluorescein. Ultimately, these two methods were too imprecise to produce reliable results, as they were measuring the average value. These two studies are included in this chapter to document what has been attempted.

In order to improve resolution of what is occurring to the cells, flow cytometry was used in the final approach to directly measure the degree of permeabilization in each cell. Propidium iodide (PI) was used to detect if a cell was permeabilized. PI is a membrane-impermeant

fluorescent dye that only gains fluorescence after binding with DNA. Therefore only cells with compromised membranes will display high fluorescence readings. The flow cytometer will allow us to determine if there is even a small population shift in permeabilized cells, that was previously masked when by measuring the average.

8.2 Methods

8.2.1 Evidence of DNA/Protein Leakage using Spectrophotometer

Overnight *S. epidermidis* cultures were grown as described in section 7.2.1, with the exception that cells were resuspended and diluted with PBS, as the proteins in TSB would've masked any signs of protein leakages. The final OD_{600} was 0.2, which corresponds to a cell density of 10^6 cells/mL (data not shown).

Chemical Permeabilized *S. epidermidis* Preparation

To prepare *S. epidermidis* solutions supplemented with TWEEN® 20 at 0.1%, 0.2%, and 0.4% concentrations, 900 µl of the diluted *S. epidermidis* solution was added to nine wells in a 24 well plate (Corning, USA). 100 µl of 1% TWEEN® 20 in PBS was added to the first three wells and mixed through repeated pipetting. This gave a final concentration of 0.1% TWEEN® 20. This was repeated with 2% and 4% TWEEN® 20 in PBS, for the remaining six wells, for a final concentration of 0.2% and 0.4%, respectively.

For each TWEEN® 20 concentration, the samples were incubated at room temperature. After 15 min, 750 µl was removed from one well in each sample group and placed in separate 2 ml micro-centrifuge tubes and pelleted at 4000 rpm for 10 min. The supernatants were transferred to new micro-centrifuge tubes and the pellets were discarded. This was repeated at 30 and 45 min incubation time points for the remaining two samples in each concentration. Blanks for each TWEEN® 20 concentration were created by diluting TWEEN® 20 in PBS to the same concentrations.

Negative Control Preparation

To prepare the negative control (i.e. *S. epidermidis* samples with no TWEEN® 20 added), 900 µl of the diluted solution, described at the beginning of this section, was once again added to three wells in a 24 well plate. 100 µl of PBS was added to each well, to ensure that the final *S. epidermidis* concentration is the same as the TWEEN® 20 samples. The samples were mixed through repeated pippetting. The same procedures were repeated on the negative control as the TWEEN® 20 samples. The solutions were incubated at room temperature. At each of the three time points: 15, 30, and 45 min, 750 µl was removed from one well and pelleted. The supernatant was transferred to a clean micro-centrifuge tube.

Spectrophotonic Analysis of DNA/Protein Content

The supernatant of each sample were transferred to a plastic cuvette and the absorbances at 260 and 280 nm were measured using a spectrometer. The results were plotted on a bar graph on Excel (Microsoft, USA).

8.2.2 Evidence of Fluorescein uptake after LGS using Spectrophotometer

Overnight *S. epidermidis* cultures were grown as described in section 7.2.1, with the exception that cells were resuspended and diluted with PBS, to minimize background fluorescence from other compounds. The final OD_{600} was 0.1, which corresponds to a cell density of 0.5×10^6 cells/mL (data not shown).

Sample Preparation

To investigate if LGS can permeabilize cells enough for fluorescein uptake, *S. epidermidis* cells were subjected to LGS in the presence of fluorescein, using laser parameters: 3 mm spot size and 777.9 mJ. This treatment group is designated as LGS + Fluorescein + *S. epidermidis*. Three control groups were also prepared: Fluorescein only, LGS + Fluorescein, and Fluorescein + *S. epidermidis*. Fluorescein only served as the positive control and gives

the maximum fluorescein signal. LGS + Fluorescein served as an indicator to check if the LGS treatment would photobleach the fluorescence of fluorescein. Finally, Fluorescein + *S. epidermidis* served to measure the background fluorescence from residual fluorescein left after washing of the cells. Two blanks were also prepared: LGS + PBS and LGS + *S. epidermidis*, for samples with and without *S. epidermidis*, respectively.

To prepare samples with *S. epidermidis*, LGS + Fluorescein + *S. epidermidis*, Fluorescein + *S. epidermidis*, and LGS + *S. epidermidis*, for each group, 1 ml of the diluted *S. epidermidis* solution was added to 2 separate 2 ml micro-centrifuge tubes. For samples without *S. epidermidis*: Fluorescein only, LGS + Fluorescein, and LGS + PBS, 1 ml of PBS was added to 2 separate 2 ml micro-centrifuge tubes, for each group.

For samples with fluorescein added, 100 µl was removed from each sample and 100 µl of 20% w/v sodium fluorescein in 0.2 µm filter-sterilized deionized water was added and mixed through repeated pipetting. For samples without fluorescein, 100 µl was removed from each sample and 100 µl of filter-sterilized deionized water was added. This was done immediately before the first sample was to be treated with LGS.

LGS Treatment

As discussed previously in section 7.2.3, LGS pressures decreases rapidly after 2 mm, therefore, in order to ensure the maximum percentage of the cells are treated in the sample, a 1.5 ml micro-centrifuge tube is first filled with 1.5 ml of non-sterile tryptic soy agar and filled with 300 µl of the treatment group sample. A modification was made here to use black/opaque micro-centrifuge tubes, to prevent possibilities of photo-bleaching of fluorescein from the Nd:YAG laser and the ablation event.

300 µl of each sample was placed in a separate micro-centrifuge tube that had been prepared as described above and a $1 \times 1\,\mathrm{cm}^2$ of waterglass-Ti-coated polyimide, described in section 7.2.4, was placed on top of the micro-centrifuge tube. Care was taken to ensure there was no air trapped under the polyimide. Once again it is critical to use this black/opaque polyimide to eliminate the chance of laser bleed-through. A single pulse of Nd:YAG laser,

at spot size 3 mm and laser density 110.1 mJ/mm^2, was used to ablate the Ti to generate the shockwave. After treatment, the samples were transferred to new black micro-centrifuge tubes. This was performed on: the control sample (LGS + Fluorescein), the treatment sample (LGS + Fluorescein + *S. epidermidis*), and the blanks (LGS + deionized water and LGS + *S. epidermidis*. Similarly, this procedure was repeated with the non-LGS samples, with the only difference of no laser ablation of the Ti. This is to ensure there were no confounding effects, as a result of contact with the TSA, micro-centrifuge tube, or the polyimide film. This was repeated once more and combined with the previous samples, so that each group had a final volume of ∼600 µl.

Fluorescein Measurement and Analysis

500 µl of each sample was transferred to a new 1.5 ml micro-centrifuge tube. Samples were washed once with PBS and resuspended in fresh PBS. 100 µl of each sample was transferred to a separate well in a non-sterile 96 well plate (BioTek, VT, USA). Using an excitation of 460 nm, the emission of each sample at 515 nm was recorded using Synergy H1 Hybrid microplate reader (BioTek, VT, USA). Samples with *S. epidermidis* cells were blanked with LGS + *S. epidermidis*, while samples without the cells were blanked with LGS + PBS. The data were collected and plotted on Excel (Microsoft, USA).

8.2.3 Evidence of Propidium Iodide uptake after LGS using Flow Cytometry

Overnight *S. epidermidis* cultures were grown, as described in section 7.2.1, with the exception that cells were resuspended and diluted with 0.2 µm filter-sterilized 0.85% NaCl solution (FSNC), as the phosphates in PBS and TSB would've affected the effectiveness of the propidium iodide (PI) and SYTO 9 (S9) dyes. The final OD_{600} was 1.38, which empirically gave ∼1000 events/s on the SORP BD LSRII Analytic flow cytometer.

The following protocol was adapted from the LIVE/DEAD^{TM} BacLight^{TM} Bacterial Viability Kit, for microscopy & quantitative assays (Product # : L7012, ThermoFisher Scientific, USA)[100].

Sample Preparation for LGS Treatment and Flow Cytometry

4×1 ml aliquots were added to 4 separate 1.5 ml micro-centrifuge tubes. 3 were used for live cell preparation, while the last were used for dead cell preparation. The cells were then pelleted using a micro-centrifuge, at 10 000 rpm for 3 min at 4 °C. The supernatants were removed and 1 ml of fresh FSNC was added to the three live cell preparations, and 1 ml 0.2 µm filter-sterilized 70% isopropanol in deionized (DI) water was added to the dead cell preparation. All four tubes were then resuspended using a vortexer and incubated at room temperature for 30 min, vortexing once at 15 min mark to mix suspension. All samples were then washed once with 1 ml of fresh FSNC, and finally resuspended in 1 ml of fresh FSNC.

10 µl of the live cell preparation was added to nine black 1.5 ml micro-centrifuge tubes, containing 987 µl of FSCN. Each tube was used for a different treatment group: live unstained control (no dye added), live PI only control, live S9 only control, live control (both PI and S9 added), LGS-0 (PI and S9 dye added immediately before LGS treatment), and four LGS treated groups, where the PI and S9 dyes were added 10 and 20 min after treatment (LGS-10, and LGS-20, respectively). 10 µl of the dead cell preparation was added to four black 1.5 ml micro-centrifuge tubes, containing 987 µl of FSCN and were used in three separate treatment groups: dead unstained control (no dye added), dead PI only control, dead S9 only control, and dead control (both PI and S9 added).

Samples LGS-0, LGS-10, and LGS-20, were treated by LGS as described by section 7.2.3. However the procedure was modify to use 0.2 ml PCR tubes, instead of the standard 1.5 ml tubes, to maximize the percentage of cells that are treated after a single treatment of LGS. To protect the dye from photo-bleaching from the laser, black electrical tape was used to cover the outside of the tube. 1.5 µl S9 and 1.5 µl PI dyes were added to the 997 µl LGS-0 solution, immediately before LGS treatment and mixed through repeated pipetting. 7× ∼60 µl of the mixed solution was treated with LGS and were combined in a new opaque micro-centrifuge tube for a final volume of 400 µl. For the remaining LGS samples, 7× ∼60 µl of the unstained solutions were first treated with LGS and then combined in a new opaque tube, with a final volume of 400 µl for each treatment group. After incubating at room-temperature for the

requisite time (10 or 20 min), 1.5 µl S9 and 1.5 µl PI dyes were added to the remaining LGS samples. For the live and dead control (both PI and S9 added), 1.5 µl S9 and 1.5 µl PI dyes were added. For the live and dead S9 only control, 1.5 µl S9 dye and 1.5 µl FSNC were added. For the live and dead PI only control, 1.5 µl PI dye and 1.5 µl FSNC were added. Finally, for live unstained control, 3 µl FSNC was added. All tubes were then vortexed.

Experimentally, the time points were done in reverse, so that the addition of the dyes for all samples can be added within a 10 min window, i.e. LGS-20 was performed first followed by LGS-10, etc. This is to prevent problems arising from long/inconsistent incubation times in the dye (e.g. diffusion of dyes, engulfment of dyes by live cell).

Flow Cytometry Analysis

All samples were run through the SORP BD LSRII Analytic Flow Cytometer (BD Bioscience, USA) at the Janis V. Giorgi Flow Cytometry Core Laboratory in UCLA. The filters used to detect the PI and S9 dyes were Yellow-Green Octagon (561 nm) and Blue Trigon (488 nm), respectively. The samples were recorded for 100 000 events at 500-1000 events/s. Samples were gated based on the PI expression of the dead and live controls (both dyes). The percentage of population above this gate for each sample was calculated.

8.3 Results

8.3.1 Evidence of DNA/Protein Leakage using Spectrophotometer

Each sample group consisted of one sample. As seen in fig. 8.1(a), the 260 nm absorbance of the 0% TWEEN® 20 increases with longer incubation times. Meanwhile, at higher concentrations of TWEEN® 20, the absorbances are negative. Similar results were seen for 280 nm absorbances (Fig. 8.1(b)). Since PBS doesn't contain DNA and proteins, the increase over time may be a result of simple diffusion of these molecules out of the cell. As DNA is too large of a molecule to diffuse out, this increase in the 260 nm may be a result of free nucleotides, like ATP. Finally, the negative absorbance value observed for the higher

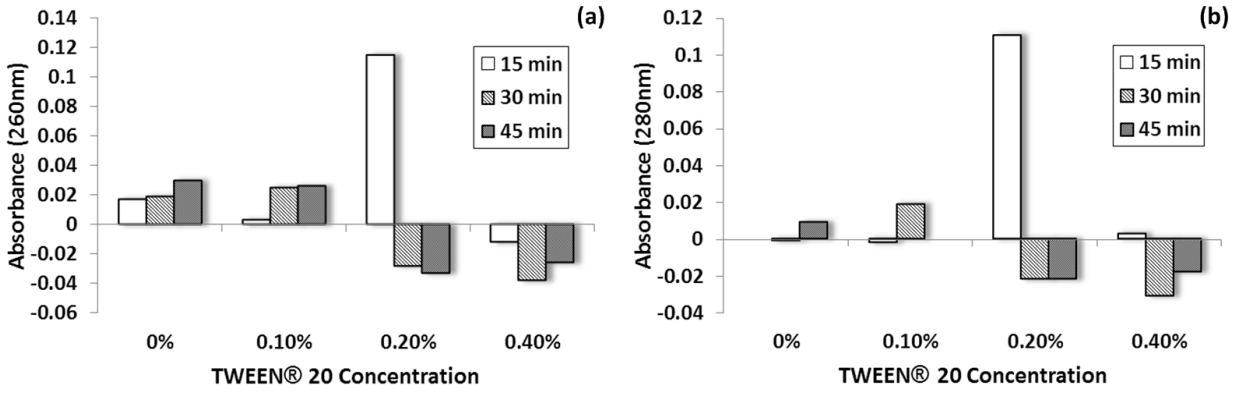

Figure 8.1: Spectrophotometry measurements of *S. epidermidis* supernatant, after permeabilization with TWEEN® 20. DNA and protein absorbances at 260 nm (a) and 280 nm (b), respectively, were measured after cells were incubated in solutions supplemented with 0.1%, 0.2%, and 0.4% TWEEN® 20 for 15, 30, and 45 min. Ultimately deemed too imprecise of a method, as background levels of DNA/protein in the 0% sample were higher than many of the permeabilized samples and the values measured .

concentrations, may be a result of the TWEEN® 20. As the blanks used were PBS supplemented with TWEEN® 20 at same concentration, it may be that at 0.2% and above, the TWEEN® 20 had significant contributions to the absorbances. However, in the treatment groups, the cells bind with TWEEN® 20 and pulls it out of solution when it gets pelleted, lowering the final concentration of TWEEN® 20.

0.2% for 15 min had high absorbance values for both 260 and 280 nm. This may be that this was the ideal concentration and time, but wouldn't explain why the values become negative at longer incubation times. More trials are needed to see if this is repeatable.

While these results are not, by any means, conclusive, due to the low sample size, it does give an idea of the expected range of values. In general, the absorbance values seemed to be constrained to below 0.04, with the floor absorbance set to 0.027, which is determined by the 0% concentration. This gives a very low dynamic range, which would mean that the pipetting and the mixing of the solutions would have to be incredibly precise to accurately pick up any changes in concentrations due to permeabilization. Finally, the last fatal flaw in this methodology is that it only looks at leakage of molecules, when the original objective was to look for signs of influx of molecules.

8.3.2 Evidence of Fluorescein Uptake after LGS using Spectrophotometer

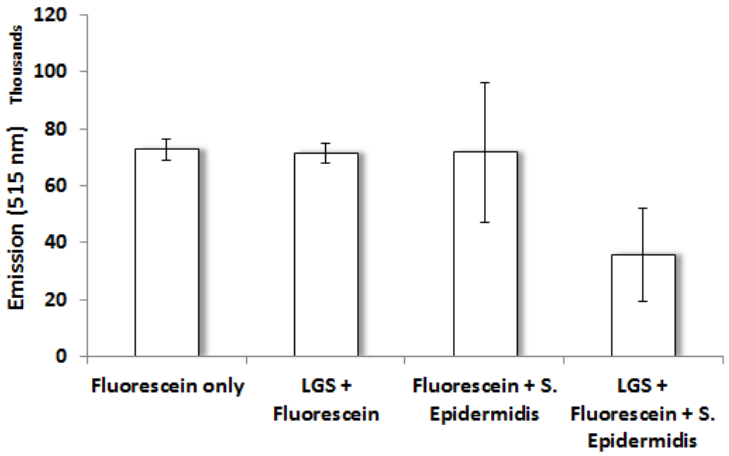

Figure 8.2: Fluorescence measurements of fluorescein uptake in *S. epidermidis* after LGS treatment. The high fluorescence in the fluorescein only and LGS + fluorescein samples demonstrate that remnant fluorescein after washing is too high for this methodology to work.

Each sample group consisted of two samples. As seen in fig. 8.2, fluorescein only, LGS + fluorescein, and fluorescein + *S. Epidermidis* had similarly high fluorescence values. The high emission value for the fluorescein only samples suggest that there is significant quantities of fluorescein adhering to the sides of the tube that are not being removed during the washing step. Since there are no cells to pellet in this sample, no fluorescein should be left after washing. Additional washing with PBS can be performed to reduce the background. However the additional time required may allow too much of the fluorescein to diffuse out of the bacterial cells. Finally, the similar values for LGS + Fluorescein, verifies that the setup with the black micro-centrifuge tube and polyimide is capable of blocking out the laser light, preventing photo-bleaching. This will be useful in the flow cytometer experiments. It is unknown why the LGS + Fluorescein + *S. epidermidis* saw a decrease in fluorescein concentration.

Once again, the results are, by no means, conclusive, due to the low sample size, it does give insight into the limitations of this methodology. Fluorescein sticking to the tube is a major problem, which may be resolved by additional washings, but that can lead to other

problems, namely loss of signal.

8.3.3 Evidence of Propidium Iodide Uptake after LGS using Flow Cytometry

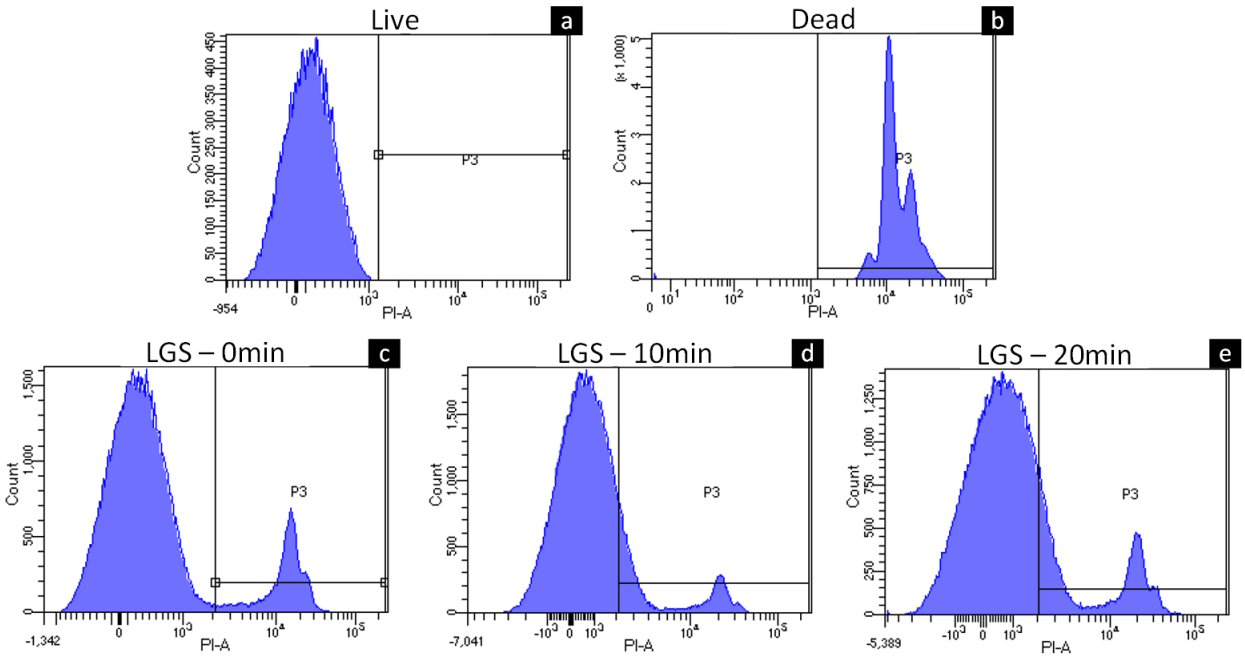

Figure 8.3: Flow cytometry histograms of propidium iodide fluorescence. Cells with no treatment (live control, a) and cells fixed with 70% isopropanol (dead control, b) were used to set the PI threshold, represented by a vertical line, which cells need to be above to be considered permeabilized. Samples treated with LGS showed a small subset of cells that were permeabilized, regardless of when the dye was added, immediately before LGS treatment (LGS-0 min, c), 10 minutes after treatment (LGS-10 min, d), and 20 minutes after treatment (LGS-20 min, e). Exact percentages can be seen in table 8.1.

As seen in fig. 8.3a-b, there is clear separation between the fluorescences from the live control sample and the dead control sample, which allowed us to create a threshold, represented by the vertical line, that cell fluorescence had to be above to be considered permeabilized. This confirmed by the low PI percentage for live control and high PI percentage for dead control as seen in table 8.1. As for samples treated with LGS, all exhibited a small subset of cells that displayed high PI fluorescence (fig. 8.3c-e), with similar PI percentages, table 8.1. As the percentages are relatively similar, the effects of LGS does not appear to diminish with time.

Sample group	PI percentage
Live	0.5%
Dead	99.4%
LGS-0 min	14.7%
LGS-10 min	14.6%
LGS-20 min	19.6%

Table 8.1: Percentage of cells that displayed a propidium iodide fluorescence higher than the threshold set by the Live and Dead controls

8.4 Discussion

As seen in the flow cytometer results, only a low percentage of cells were affected by the LGS shockwave. This may explain why previous studies had mixed results, as the effects were relatively small. However, it is interesting to note that the percent change observed in flow cytometry are similar to the percent changes observed for the effectiveness of gentamicin in ch. 5. While this does not prove that the primary mechanism for the increase in gentamicin effectiveness is cell permeability, it does demonstrate that LGS can have a direct effect on bacteria cells.

It is also important to note that in all LGS treatments only a single shockwave was delivered to each sample. Previous studies on the effects of LGS on bacteria, often used more than 10 shockwaves for each treatment[72, 73]. We expect to see an increased effect with more shockwaves delivered. However, since we were only interested in understanding the direct effects of LGS on the cells, we intentionally kept the number of shockwaves low.

CHAPTER 9

Determining a Therapeutic Window for Laser Generated Shockwave Treatment in a Rodent Skin Model

9.1 Introduction

In this chapter, we investigate the safety of LGS in a live rodent model, and in doing so we take the first step in bringing LGS to the pre-clinical stage. Previously in ch.3, we have shown that LGS does not cause injury in *ex vivo* porcine skin, using a 3 mm spot size with laser fluence, 657.4 mJ. However, only structural damage can be assessed, as *ex vivo* tissue is no longer viable. Cellular responses, such as apoptosis, and inflammation cannot be seen in an *ex vivo* model. Therefore in this study, a greater focus will be placed on the cellular response to LGS treatment. The animals will be treated with LGS and followed over a three day observation period. Previous preliminary studies have suggested that LGS is well-tolerated by tissue[101]. Therefore, we believe that three days is sufficient for a cellular response against damages caused by LGS to fully develop.

The objective of this chapter is to determine the maximum therapeutic threshold that the system can safely be used at in future efficacy studies. Sec. 6.3.1 has shown that peak pressures generated using polyimide film as the supportive substrate, generates the most peak pressure at a Nd:YAG spot size of 3 mm, 295.7 MPa using a laser fluence of 777.9 mJ. As the pulse wideth of the Nd:YAG changes at different energy fluences[76], we will vary the Nd:YAG energy density through the use of two additional spot sizes, 2.2 and 4.2 mm. This will also help verify the peak pressure measurements obtained in sec. 6.3.1, by examining

the extent of damage for each laser parameter.

The LGS substrate used in this study is the waterglass-Ti coated polyimide described in section 7.2.4. The thin polyimide gives the LGS substrate flexibility to fit the contour of the treatment area of the rodent. Furthermore, the polyimide used is opaque to 1064 nm wavelength light. Therefore, any stray laser energy, either due to spot overlap or unused laser energy, will be absorbed by the polyimide, preventing thermal damage of the tissue from laser bleed through.

To assess the safety of LGS treatment on healthy skin, twenty seven rodents were treated with LGS using spot sizes of 2.2, 3.0, and 4.2 mm(9 animals per spot size) and laser fluence of 777.9 mJ. The animals were then observed for three days and the treatment areas were graded for signs of damage under gross observation. Three animals from each group were euthansized for histology at 1 h, 1 d, and 3 d after treatment for analysis of tissue and cellular damages. Furthermore, through histology we investigated the depth of the injuries and if it correlates with the peak pressure fall off seen in shockwave passing through the ultrasound gel in sec. 6.3.1.

9.2 Methods

All animal work was done with ARC approval.

9.2.1 Preparation of Sprague-Dawley Rats for LGS-Treatment

Nine Sprague-Dawley rats were used for the safety study of LGS using a spot size of 4.2 mm. The day before the treatment, the animals were first anesthetized in an induction chamber with 5% isofluorane in pure O_2 with a flow rate of 0.9 L/min. Each animal was then transferred out of the induction chamber and fitted with a nose cone that provided 1.5% isofluorane in pure O_2 with the same flow rate to maintain general anesthesia. A $6\times10\,cm^2$ area was shaved on the left lateral side of the abdomen, using an electric clipper with no guard attached. This left about $\sim$ 2 mm length of fur. To remove the remaining fur, a

$4\times6\,\mathrm{cm}^2$ cold wax strip was applied in the direction of the fur growth and ripped off in the opposite direction. This was repeated with a fresh cold wax strip to remove any remaining fur. The animals were then returned to their cages for at least 24 hours, so that any inflammation from the waxing can be resolved before treatment with LGS.

Twenty-two more rats were similarly shaved, waxed, and allowed to recover. Eighteen rats were used for safety studies looking at spot sizes of 3.0 and 2.2 mm, with nine rats each. The remaining four rats were used as negative control.

9.2.2 LGS Raster Scanner Setup and LGS Treatment

The portable LGS raster scanner described in chapter 4, was used for this safety study. On the day of the LGS treatment, nine shaved and waxed rodents were used for each spot size. The animals were once again first anesthetized in an induction chamber with 5% isofluorane in pure O_2 with a flow rate of 0.9 L/min. Each animal was then transferred out of the induction chamber and mounted on a custom-built platform and fitted with a nose cone that provided 1.5% isofluorane in pure O_2 with the same flow rate to maintain general anesthesia. In all trials, the Nd:YAG laser was set to its maximum laser energy of 777.9 mJ and focused down to the desired spot size. The scanning head was adjusted to be 8.5 in above the treatment area, in order to achieve a spot size of 4.2 mm, which gave a final energy density of $56.2\,\mathrm{mJ/mm}^2$. A distance of 10 in and 14 in were used to achieve a spot size of 3.0 mm and 2.2 mm, respectively. This resulted in a final energy density of $110.1\,\mathrm{mJ/mm}^2$ and $204.7\,\mathrm{mJ/mm}^2$, respectively.

An EF-EOS M Canon camera, with an EF-M22mm f/2 lens, was mounted to the platform and the area to be treated with LGS was imaged. A 1 mm layer thick ultrasound gel was manually applied to the polyimide side of a $2 \times 5\,\mathrm{cm}^2$ waterglass-Ti coated polyimide, as described in section 7.2.4. This was then applied on top of the treatment area, ultrasound gel side down, taking care to minimize the amount of air trapped between the ultrasound gel and the treatment area.

The animal was then position below the scanning head and an image of the animal was

taken, using the camera attached to the scanning head. The user then defined a $3 \times 4\,\mathrm{cm}^2$ treatment area over the LGS substrate on the image in MATLAB. The MATLAB script generated a list of XY motor positions to hexagonally tile the defined treatment area with the desired laser spot size. Using a spot size of 2.2, 3.0, or 4.2 mm, this resulted in ∼220, 120, and 60 spots needed to cover the defined areas. The generated laser tiling was presented to the user as an image for confirmation. Once confirmed the system raster scans the Nd:YAG laser over the pre-defined positions at 8 Hz. This was repeated for all LGS treatment groups, with 9 rats in each treatment group.

After LGS treatment, the LGS substrate was removed and the ultrasound gel was cleaned off with sterile gauze. The treated area was imaged once more with the EF-EOS M Canon camera and the animal was returned to its cage.

9.2.3 Analysis of Tissue Health through Histology and Gross Anatomy

One hour after LGS treatment, 3 rats from each treatment group were euthanized with CO_2, followed by a thoracic puncture as a secondary euthanasia. Three $1 \times 1\,\mathrm{cm}^2$ sections of skin were harvested from the treatment area for each animal and fixed with 10% buffered formalin for at least 24 hours. The remaining animals were imaged again at 24 hours post-LGS treatment and 3 more animals from each group were euthanized and skin samples were harvested and fixed. The final three animals per group were imaged again 48 and 72 hours post-LGS treatment and euthanized after the last images were taken at 72 hours post treatment. Three $1\,\mathrm{cm}^2$ sections of skin were harvested from the treatment areas and fixed with 10% buffered formalin for at least 24 hours.

The negative control animals were euthanized and skin samples were harvested and fixed 24 h after shaving and waxing.

9.2.4 Analysis of Photographic Images

Each image was cropped to be $2 \times 4\,\mathrm{cm}^2$, using the included ruler in each image to calibrate the pixel/cm dimensions in each image. Each image was then graded on hematoma prevalence

and size on a grade from 0 - 3. The grades for the images were then grouped based on Nd:YAG spot size used and time point. A fourth group representing the negative control was also added. Using MATLAB, a Dunn's test was used to test if there was a difference between each treatment group and the negative control. This was performed separately for prevalence and size of hematomas.

9.2.5 Histology of Tissue after LGS treatment

All fixed samples were submitted to the UCLA Translational Pathology Core Laboratory (TPCL) for histology slide preparation. Samples were bisected orthogonal to the epidermis, in order to visualize the different layers and structure of the skin. The samples were embedded in paraffin with the bisected edge facing the side to be cut. Four 4 µm sections were made for each sample and were stained with hematoxylin and eosin (H&E) before mounted on a glass microscope slide. The slides were reviewed by a trained pathologist. Notable features in damages were noted for each animal.

9.3 Results

9.3.1 Gross Analysis of Tissue after LGS Treatment

Photographic images of the treatment area were taken immediately before ($0\,h^-$) and immediately after ($0\,h^+$) treatment with LGS. This was performed for all three Nd:YAG spot sizes for a total of nine animals per spot size. Three animals were euthanized for tissue collections at each time point: 1 h, 1 d, and 3 d after LGS treatment. This resulted in nine images taken for time points: $0\,h^-$ and $0\,h^+$, six images for time point: 1 d, and three images for time points: 2 d and 3 d, for the three spot sizes.

All photographic images were graded based on the standards presented in fig.9.1 and fig.9.2 and grades are presented in table 9.1. All animals exhibited no signs of damage or erythemas in the treatment area, immediately before LGS treatment $0\,h^-$. Following treatment with a 2.2 mm spot size, 4 out of 9 animals exhibited no damage to the skin.

		Erythema Size				Erythema Prevalence				
Group	Time Point	0	1	2	3	0	1	2	3	Total
	$0\,h^-$	9	-	-	-	9	-	-	-	9
	$0\,h^+$	4	5	-	-	4	5	-	-	9
2.2 mm	1 d	6	-	-	-	6	-	-	-	6
	2 d	3	-	-	-	3	-	-	-	3
	3 d	3	-	-	-	3	-	-	-	3
	$0\,h^-$	9	-	-	-	9	-	-	-	9
	$0\,h^+$	-	4	3	2	-	3	3	3	9
3.0 mm	1 d	5	1	-	-	5	1	-	-	6
	2 d	3	-	-	-	3	-	-	-	3
	3 d	3	-	-	-	3	-	-	-	3
	$0\,h^-$	9	-	-	-	9	-	-	-	9
	$0\,h^+$	2	5	2	-	2	4	3	-	9
4.2 mm	1 d	6	-	-	-	6	-	-	-	6
	2 d	3	-	-	-	3	-	-	-	3
	3 d	3	-	-	-	3	-	-	-	3

Table 9.1: Grading of gross anatomy immediately before LGS therapy and the following three day observation period. Nd:YAG laser fluence used was 770.2 mJ, with spot sizes 2.2, 3.0, and 4.2 mm. Gradings were performed based on standards outlined in fig.9.1 and fig.9.2. Sample size at each time point is given in the total column.

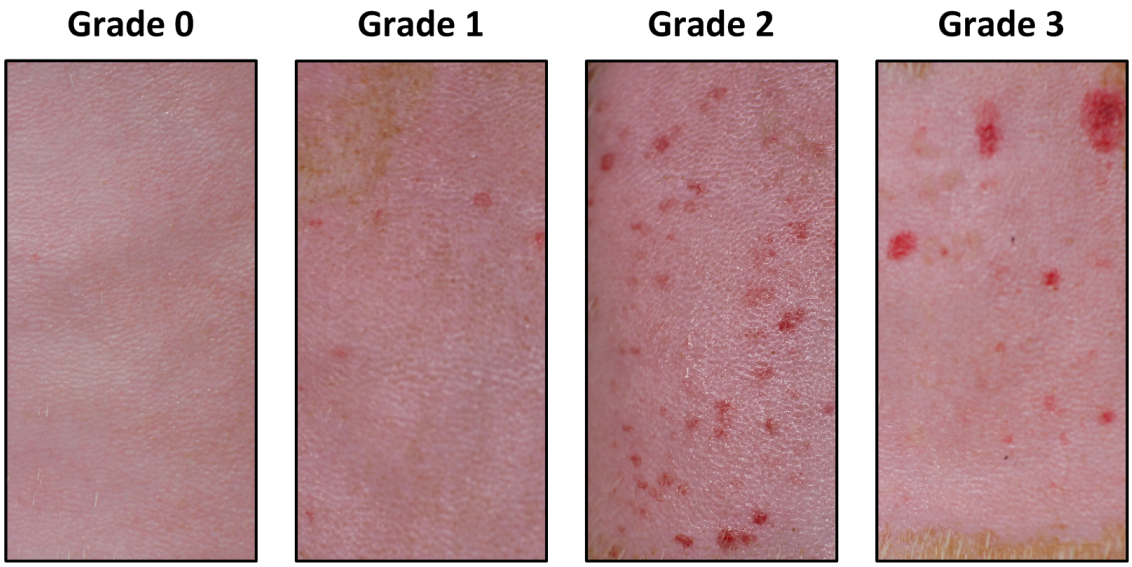

Figure 9.1: Grading standards for size of erythemas in rodents after treatment with LGS therapy. Each window is $4 \times 6\,\mathrm{cm}^2$.

The remaining 5 animals had minor erythemas, in terms of size and prevalence (Grade 1's). Treatments using a 3.0 mm spot size resulted in more extensive damages, where all animals displayed some level of damage to the skin, immediately after treatment. Two of the nine animals developed large erythemas ($\sim 0.5\,\mathrm{cm}^2$)(grade 3), with medium prevalence (grade 2). Another two animals exhibited medium sized erythemas (grade 2), with high prevalence (grade 3). For 4.2 mm spot size, the damages observed were less extensive than those observed when a 3.0 mm spot size was used, but more extensive than those observed in the 2.2 mm case. This corroborates well with the peak pressure measurements obtained in sec. 6.3.2, with the highest pressures measured at 3.0 mm, next highest pressure at 4.2 mm, and the lowest pressure at 2.2 mm.

In nearly all cases, the erythemas were completely resolved after 24 h, while only one animal still exhibited minor damage one day after treatment (Grade 1's). This animal was treated with a 3.0 mm spot size and was originally graded a 2 in both erythemas size and prevalence, at $0\,\mathrm{h}^+$. Unfortunately, one of two animals with the most extensive damages after treatment (3.0 mm spot, grade 3 erythemas size and grade 2 erythemas prevalence) was euthanized for histology at 1 hour post-treatment, so progression of its injuries wasn't recorded. The remaining animal with high initial erythemas grads fully resolved its injuries

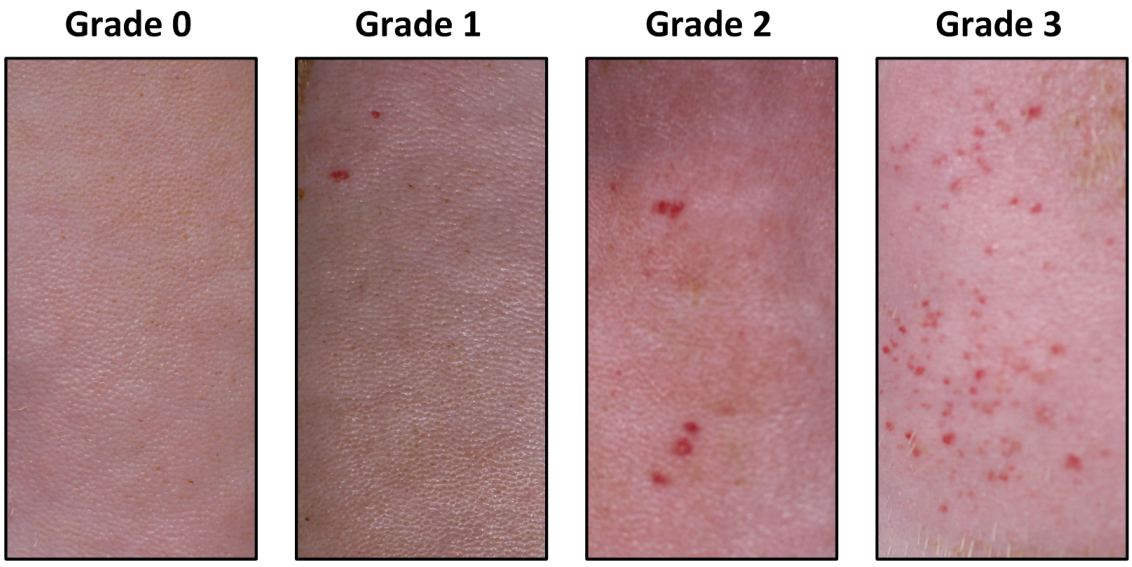

Figure 9.2: Grading standards for number of erythemas in rodents after treatment with LGS therapy. Each window is $4 \times 6\,\mathrm{cm}^2$.

after 24 hours under gross observations, suggesting that even high initial grades can be resolved quickly.

A multiple comparison statistical test, Dunn's Test, was performed on $0\,\mathrm{h}^+$ data against the negative control for both erythemas size and erythemas prevalence gradings. The critical Q was found to be 2.3940 for both, which represents the threshold that the Q-score needs to be higher to be considered significant with $\alpha = 0.05$. The Q-scores for the erythemas size gradings were found to be: 1.7423, 4.4458, and 2.8958 for 2.2, 3.0, and 4.2 mm, respectively, when compared against negative control, $0\,\mathrm{h}^-$. The Q-scores for erythemas size prevalence gradings were found to be: 1.6042, 4.4918, and 2.8876 for 2.2, 3.0, and 4.2 mm, respectively, when compared against negative control, $0\,\mathrm{h}^-$. In both instances, the damages observed after treatment with spot size 3.0 and 4.2 mm at laser fluence, 770.2 mJ, were found to be statistically significant.

9.3.2 Histological Analysis of Tissue after LGS Treatment

Three skin biopsies were harvested from the treatment area and four H&E stained sections were prepared for each sample for a total of 12 sections for each animal. Sections of each

Group	Time Point	Loss of Whole Thickness of Epidermis	Epidermis Necrosis	Hyper-eosinphilia	Superficial Dermal Inflammation	Blister	Total
2.2 mm	1 h	-	1	1	1	2	3
	1 d	-	-	-	-	-	3
	3 d	-	1	-	1	-	3
3.0 mm	1 h	1	2	1	1	1	3
	1 d	2	2	3	3	1	3
	3 d	-	2	1	2	-	3
4.2 mm	1 h	-	3	1	3	1	3
	1 d	-	-	-	-	-	3
	3 d	-	1	1	1	-	3

Table 9.2: Frequency of rats with the observed histological features after treatment with LGS. Examples of each feature is displayed in fig. 9.3.

animal were reviewed for notable features. Examples of common features observed can be seen in fig. 9.3. Frequency of animals that displayed each feature are summarized in table 9.2.

2.2 mm Spot Size

Nine rodents were treated with LGS using a Nd:YAG spot size of 2.2 mm. Three animals were euthanized at each time point: 1 h (animals 1, 2, and 3), 1 d (animals 4, 5, and 6), and 3 d (animals, 7, 8, and 9). Skin biopsies were collected after euthanasia and H&E sections were prepared.

For tissues harvested 1 h after LGS treatment, Animal 1 showed no signs of damage or inflammation in the epidermis and dermis for all its sections. Animal 2 had signs of surface necrosis, displayed as hypereosinophilia of tissue, or localized intra-cellular edema of the basal layer of the epidermis with mild inflammation in the superficial dermis directly inferior to the injury. Small blisters were also seen in the biopsies from animal 2. Subcorneal blisters with no cell infiltration were seen in animals 2 and 3.

For tissues harvested 1 d after LGS treatment, all biopsies from animals 4, 5, and 6 had intact epidermis and dermis and no signs of damage or inflammation.

Finally for tissues harvested 3 d after treatment with LGS, all animals (7, 8, and 9) had sections that exhibited localized epidermal necrosis, displayed as intra-cellular edema of the epidermal basal layer, along with mild inflammation in the superficial dermis directly inferior to the edema. Animal 9 also had minor intraepidermal blisters.

3.0 mm Spot size

Nine rodents were treated with LGS using a Nd:YAG spot size of 3.0 mm.Three animals were euthanized at each time point: 1 h (animals 1, 2, and 3), 1 d (animals 4, 5, and 6), and 3 d (animals, 7, 8, and 9). Skin biopsies were collected after euthanasia and H&E sections were prepared.

For animals euthanized 1 h after LGS treatment, animal 1, had tissue samples that exhibited larger portions of the epidermis exhibiting hypereosinphilia than were seen in the samples from treated with the 2.2 mm spot size, smaller portions had an intact underlying epidermis, while in larger portions the whole thickness epidermal necrosis was seen. In animal 2 and 3, localized epidermis necrosis, displayed as intra-cellular edema of the basal layer of the epidermis were seen, but no inflammations were observed.

For biopsies harvested 1 d after LGS treatment hypereosinphilia of tissues were seen in all animals (4, 5, and 6). Animals 4 and 5 exhibited whole thickness necrosis of the epidermis directly below the hypereosinphilia. Localized intra-cellular edema of the basal layer of the epidermis with inflammation in the superficial dermis were also observed in all animals (4, 5, and 6). The

For biopsies obtained 3 d after LGS treatment, animals 7 and 8 had sections that exhibited surface necrosis and inflammation in the dermis directly inferior to the injury. Inflammatory response was on par with those seen in samples treated with 2.2 mm spot size. Animal 8 also had sections that exhibited hypereosinphilia. No damages or injuries were seen in the sections for animal 9.

4.2 mm Spot Size

Nine rodents were treated with LGS using a Nd:YAG spot size of 4.2 mm. Three animals were euthanized at each time point: 1 h (animals 1, 2, and 3), 1 d (animals 4, 5, and 6), and 3 d (animals, 7, 8, and 9). Skin biopsies were collected after euthanasia and H&E sections were prepared.

All histological sections of skin biopsies harvested 1 h after LGS treatment, animals 1 and 3 showed: localized surface necrosis, displayed as intra-cellular edema in the basal layer of the epidermis with mild inflammation in the superficial dermis directly inferior to the necrosis (animals 1 and 3), hypereosinphilia of tissue(animal 1), and subcorneal blisters with no cell infiltration (animal 3). Extent of damage and inflammatory response was on par with those seen in samples treated with 2.2 mm spot size. Animal 2 showed no signs of damage or inflammation in the epidermis and dermis.

All skin biopsies harvested 1 d and 3 d after LGS treatment, showed no signs of damage or inflammation in the epidermis and dermis (animals 4, 5, 6, 7, 8, and 9).

Histological sections corroborate with the severity of damage seen in the gross images. Only samples treated with 3.0 mm spot size exhibited large portions of hypereosinphilis of tissues, with whole thickness epidermal necrosis. Samples treated with either 2.2 and 4.2 mm spot sizes also exhibited hypereosinphilia of tissue, but were smaller and in all cases the epidermis remained intact. More analysis will be needed to understand why intra-cellular edema of the epidermis is occurring post-LGS treatment. However, it is important to note that in all cases the damage is localized to the epidermis and superficial dermis and is not expected to hinder the healing of wounds. The quick rate of healing, also signifies the low severity of the injuries, as many of inflammatory response observed immediately post-LGS treatment were resolved within 3 days.

9.4 Discussion

The low severity of the injuries, even at the highest peak pressure of 295.7 ± 35.4 MPa when using a 3 mm spot size, demonstrate that LGS is well tolerated by cutaneous tissue. As the injuries generally heal within 24 hours, we do not expect them to hinder the healing process of wounds and most likely are not relevant in a clinical setting. Therefore, the maximum safety threshold is at least 295.7 ± 35.4 MPa. It is very likely that the maximum safety threshold can be even higher, as injuries are still minor. However, as we have reached the maximum possible setting in our system, we were not able to test this hypothesis.

As mentioned in ch 6, uniformity of peak pressures arriving at the tissue is very dependent on the uniformity of thickness of the ultrasound gel. Therefore, the animals with a grade 3 in erythema size and a grade 2 in erythema prevalence may be an example of the ultrasound gel being too thin on one side, while the reverse may be a case where the gel is more uniform. This effect may explain why the larger erythema were localized primarily to one side in the grade 3 example in fig. 9.1, while the spots were smaller but more evenly distributed in the grade 3 example in fig. 9.2. However, more testing is needed to quantify the variability in gel thickness that will be seen in pre-clinical and clinical settings.

The gross anatomy gradings and histology data also corroborate well with the results seen in the peak pressure measurements in sec. 6.3.1. This gives further credence to the original hypothesis that the peak pressure measurements are accurate and we have not reached a maximum on our shockwave characterizing setup. This gives further credence that the shockwave is dispersing, due to the spot size and while the overall shockwave peak pressure may be higher, the dispersion from the smaller spot size is attenuating the peak pressure too much.

Finally, damages observed in the histology, in treatment groups, were predominantly in the epidermis with some inflammation in the superficial dermis. This corroborates well with previous measurements in sec.6.3.1, where the shockwaves were found to attenuate rapidly after traveling through 2 mm of ultrasound gel. This further strengthens the safety of LGS when treating infected wounds, as the bacteria will be localized near the surface, where

the peak pressures are the highest. The larger damage in the epidermis may also be sign of an impedance mismatch between the epidermis and dermis, causing a reflection of the shockwave at the interface and exposing the epidermis to a tensile wave.

One limitation in this study is the model used is on intact skin. In the case of a healing wound, the newly created collagen and tissue may be weaker than healthy cutaneous tissue, as the wound may not have had the time to restructure the initial extra-cellular matrix to strengthen the tissue. We will investigate this in the following chapter. Finally, as to why no damages were seen in previous *ex vivo* experiments in ch. 3, the dermis was never exposed to outside environment, as an open wound. In fact, the few histological sections where the whole epidermis were missing, the hypereosinphilic tissue still completely covered the wounds.

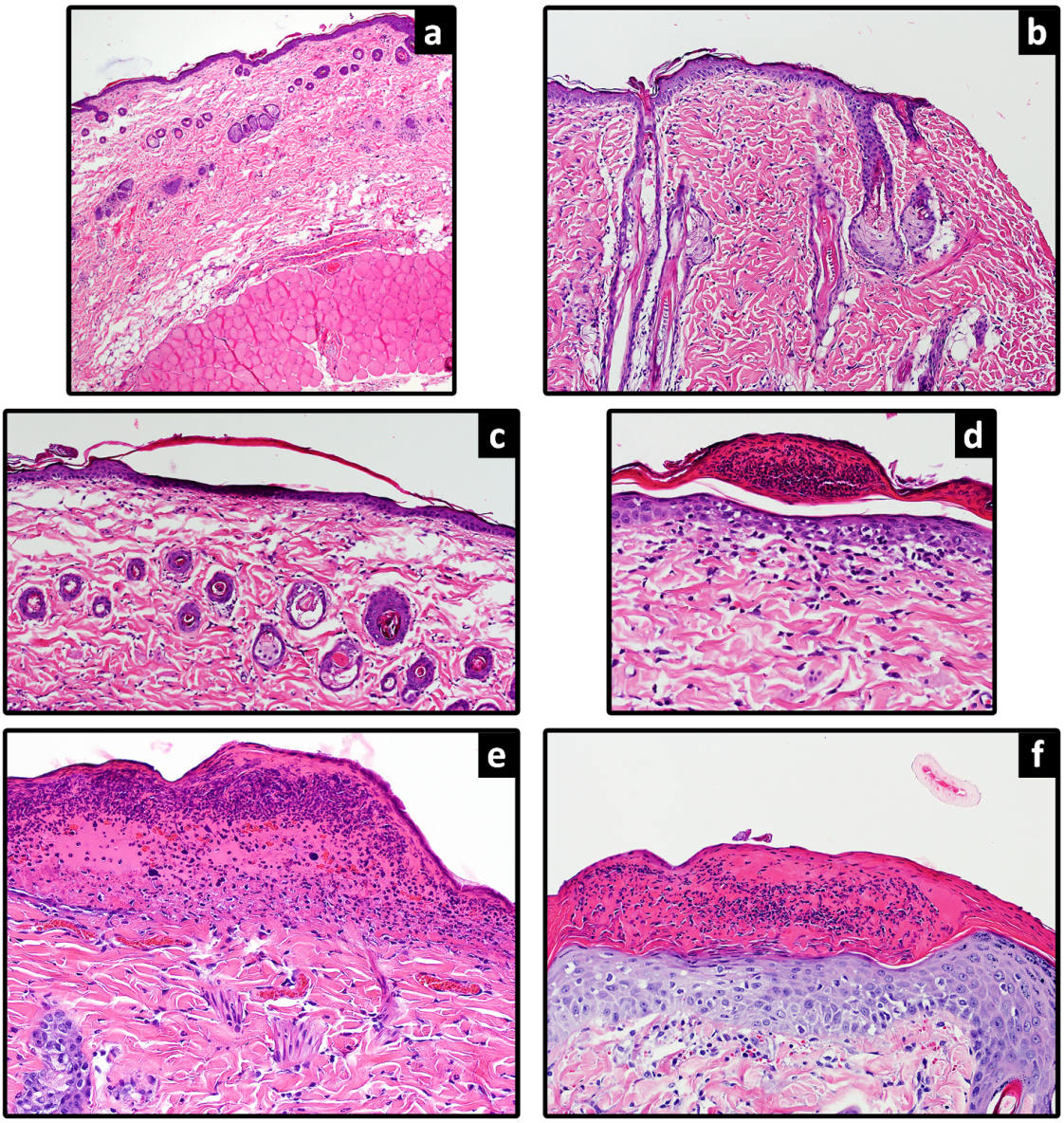

Figure 9.3: Examples of histology features seen after treatment with LGS in rodents. a) Negative Control 40×, b) Negative Control 100×, c) Sub corneal blister with no cell infiltration (blister), 2.2 mm 1 h post LGS 200×, d) Hypereosinphilia of tissue (hypereosinphilia) with surface necrosis displayed as intra-cellular edema and inflammation in dermis 2.2 mm 1 h 200×, e) Large hypereosinphilia of tissue with whole thickness epidermal necrosis (loss of whole thickness of epidermis) and inflammation, 3.0 mm 1 h 200×, f) Large hypereosinphilia feature with epidermis present, 3.0 mm 3 d 200×

CHAPTER 10

Efficacy of LGS Treatment against *S. epidermidis* Wound Infection in a Rodent Skin Model

10.1 Introduction

In this last chapter, we strive to lay the groundwork for future studies. The next step in translating LGS technology to a usable clinical device is to demonstrate the efficacy of LGS therapy in treating bacterial biofilms in a small animal infected wound model. To facilitate this, we strive to answer these two questions in the work presented in this chapter: 1. Is *S. epidermidis* a suitable bacterial biofilm model for the investigation of infected wounds and 2. Are pressures generated, with a Nd:YAG spot size of 3.0 mm and energy fluence 777.9 mJ, safe to use on damaged tissue, as previously hypothesized? To accomplish this, a preliminary study on the efficacy of LGS and LGS + topical gentamicin combinatory therapy against a cutaneous *S. epidermidis* biofilm infection in a rodent model, was carried out.

10.2 Methods

All animal and bacterial work were done with UCLA Animal Research Committee and Institutional Biosafety Committee.

10.2.1 Preparation of Cutaneous Wound Infection in a Rodent Skin Model

Twenty male rodents, between 270 to 300 g, were used to investigate the efficacy of LGS and LGS + gentamicin against a *S. epidermidis* cutaneous wound infection. The animals

were evenly divided into five groups with four animals per group: 1. non-infected wound (negative control), 2. infected wound with no treatment (positive control), 3. infected wound with topical gentamicin treatment (gentamicin only), 4. infected wound with LGS treatment (LGS only), and 5. infected wound with LGS + gentamicin treatment (LGS + gentamicin) . A full thickness wound was first created on the dorsal side of the ribs on each animal. The procedures were as follow. Each animal was first induced with anesthesia in an induction chamber with 5% isofluorane with O_2 flow rate of 0.9 l/min. The animal was then fitted with a nose cone and anesthesia was maintain with 1.5% and the same O_2 flow rate. Buprenorphine at 0.5 mg/kg and carprofen at 5.0 mg/kg, hereafter simply referenced as analgesics for brevity, were administered subcutaneously, as an analgesic. A $4 \times 4\,\mathrm{cm}^2$ area on the anterodorsal side was then prepped by first shaving with an electric buzzer and followed by a cold wax, as described in section 9.2.1. The prepped area was then sanitize with 70% isopropanol wipes. Finally, an 8 mm diameter full thickness wound was created, using a sterile 8 mm biopsy punch. The animal was then placed on an imaging platform, which consisted of a pivoting platform for positioning the animal, along with a XYZ stage to position the camera. An EF-EOS M Canon camera, with an EF-100 mm f/2.8L Macro lens was mounted to the XYZ stage and used to image the newly created wound. A ruler is included in each photographer to provide a scale for later measurements. Sterile Tegaderm™ (3M™, MN, USA) was applied to the negative control group before returning them to their cages.

The four remaining treatment groups were inoculated with 0.5 ml overnight *S. epidermidis* solution diluted with Tryptic Soy Broth (TSB) to OD_{600} 1.0. *S. epidermidis* solution was prepared, as described in section 7.2.1. A sterile Tegaderm™ transparent film dressing (3M™, MN, USA) was applied on each wound after inoculation and the animals were returned to their cages.

After 24 hours, the animals were anesthetized with isofluorane and the Tegaderm™ dressing was removed before the wounds of each animal was imaged, using the imaging platform described earlier. Fresh Tegaderm™ was then applied to the wounds and another dose of the aforementioned analgesics was administered subcutaneously.

10.2.2 Treatment of *S. epidermidis* Infected Wounds

Forty-eight hours after the initial inoculation, the wound infections were considered established and the animals were treated according to their treatment group. In all treatments, the animals were first anesthetized with isofluorane and fitted with a nose cone and placed on the imaging platform, as described in section 10.2.1. Each animal received another injection of analgesics and the Tegaderm™ dressing was removed. The area around the wound sites were cleaned with 70% isopropanol to remove any dried blood and exudate. The wounds were then surgically debrided and any eschar was removed. The wounds were imaged before proceeding with the assigned treatments.

For the LGS treatment only group, the wounds were treated with LGS, as described in section 9.2.2 and summarized here. 0.0254 mm thick polyimide, sputtered coated with 500 nm Ti, was used as the LGS substrate, due to its flexibility and opacity at 1064 nm wavelength light. A thin film (0.5 µm) of waterglass was manually applied to the Ti side of the Ti-coated polyimide film and allowed to dry. An 1 mm layer thick ultrasound gel was applied on the polyimide side of Ti-coated polyimide and placed on the wound. Care was taken to ensure no air was trapped between the layers. The portable LGS system was used to raster scan the Nd:YAG laser at 110.1 mJ/mm^2 and spot size of 3 mm. The film was removed and the ultrasound gel was wiped away with sterile gauze. To ascertain the degree of *Staphylococci* infection, the wound was swabbed for cultures, whose procedures are given in section 10.2.4. The wound was imaged again and fresh Tegaderm™ dressing was applied to the wound and the animal was returned to its cage. This was repeated for all animals in the LGS treatment only group.

For the LGS + topical gentamicin treatment group, the wounds were treated with LGS, as described above. However, the ultrasound gel was replaced with a 1 mm thick layer of 0.1% gentamicin ointment to investigate if LGS can similarly potentiate gentamicin as seen in *in vitro* studies. After LGS treatment, the polyimide film was removed and the gentamicin ointment was wiped away with sterile gauze. The wound was then swabbed for cultures and the wound was imaged. A small pea size amount ($\sim$ 250 µl) of topical 0.1% gentamicin

ointment was applied to the wound before a fresh Tegaderm™ dressing was used to cover the wound. This was repeated for all animals in the LGS + gentamicin treatment group.

For the positive control and gentamicin only treatment groups, the wounds were swabbed for cultures and fresh Tegaderm™ dressings were applied on the positive control group. For gentamicin only group, a small pea size amount ($\sim 250\,\mu l$) of topical 0.1% gentamicin ointment was applied to each wound before a fresh Tegaderm™ dressing was used. Finally, for the negative control group, the wounds of each animal were also swabbed for cultures and fresh Tegaderm™ dressings were applied.

To prevent cross contamination of the wounds between the animals, all equipment (e.g induction chamber, photography mount, nose cone) were sanitized with AccelTB (Contec™, SC, USA) between each animal.

10.2.3 Followup on Wound Healing Progression after Treatment

All wounds were monitored daily, over a nine day observation period following treatment. Each day, the animals were anesthetized and analgesics were administered. The Tegaderm™ dressing were removed and the area around the wound was cleaned with 70% isopropanol wipes. Each wound was photographed for later analysis to quantify wound healing, via changes in wound size. Fresh Tegaderm™ dressings were used to cover the wounds before returning the animals to the cages. Use of Tegaderm™ dressing was halted once the wound bed is fully dried, which occurred around 4 to 5 days after treatment.

For time points: 1 d, 3 d, and 7 d post-treatment, the wounds were assessed for *Staphylococci* bioburden before fresh Tegaderm™ dressing was applied. Each wound was surgically debrided and any eschar was removed. Each wound was then swabbed and analyzed for CFU counts, as described in section 10.1.

10.2.4 Analysis of Wound Bioburden via CFU Counts of Wound Swabs

Cotton tip swabs were used for the collection of wound exudate, which was then cultured to determine the extent of bacterial bioburden on the wounds. This was performed on all

groups at one day (1 d), three days (3 d), and seven days (7 d) post-treatment. An additional swab was also performed immediately before treatment ($0\,h^-$) for treatment groups: negative control, positive control, and 0.1% gentamicin only to establish the initial bioburden. Conversely, an additional swab was performed immediately after LGS-treatment ($0\,h^+$) for treatment groups: LGS treatment only and LGS + gentamicin to determine if LGS decreases initial bioburden in wounds.

The swabs were first placed in a sterilization pouch (Jorgensen Laboratories, Inc., CO, USA) and autoclave sterilized at 121 °C for 15 min. Immediately before wound swabs were taken, the pouch was opened in a biosafety cabinet and care was taken to not allow the cotton tip to touch anything other than the wound. The cotton tip was pressed on the wound until exudate was seen and the swab was turned three times clockwise and then three times counterclockwise. The swab was then placed in a 14 ml culture tube containing 2 ml of 4 °C autoclave-sterilized phosphate buffered saline (PBS) buffer. The tube was capped and placed on ice. This was repeated with all wound swabs, placing each swab in a separate 14 ml capped culture tube containing PBS. All tubes were stored on ice until ready for further analysis.

Once all swabs were collected for a time point, the tubes were transferred to a separate lab for CFU counting, using the Miles and Misra method[90]. Each tube was vortexed for 20 s to dislodge the bacteria from the swab. 1 ml of the suspended bacteria solution from each tube was transferred to a separate 1.5 ml micro-centrifuge tube. These solutions were then serially diluted, in tenfold increments with 4 °C sterile PBS buffer, to a final dilution factor of 10^{-5}.

Mannitol salt agar plates were used for plating of the bacteria solution to determine the extent of *Staphylococci* infection. Each Mannitol salt agar plate was first divided into four quadrant. Three 20 µl drops of the 10^{-5} dilution were placed in the first quadrant. This was repeated with 10^{-4}, 10^{-3}, and 10^{-2} dilutions. This was done in triplicate for all swabs, for a total of 60 plates per time points (3 plates per animal per time point). After the drops were placed on the plate, the drops were allowed to naturally spread and absorb into the agar. The plates were then incubated at 37 °C for 24 hours in a dry incubator. Plates were

counted for colonies and the initial concentration of the bacteria extracted from the swab in PBS was calculated in Excel (Microsoft, WA, USA).

Wound cultures were not collected for negative control at time points 1 d and 7 d.

10.2.5 Wound Area Measurement using ImageJ

Areas of each wound were measured on ImageJ (Ver. 1.47, NIH, USA), using the photographs obtained over the nine day observation period. Using the the ruler in each photograph, the pixel/mm was determined for each photograph. Next, the outside edge of the wound was traced using the freehand tool in ImageJ and the area was determined, using the measure function. Both measurements were entered into Excel (Microsoft, WA, USA) and this was repeated for all wound images from all treatment groups.

The areas were then converted from pixels to mm^2 and relative wound area was calculated by normalizing the wound area of each animal by the wound area on 0 d. The average and standard deviation of the area of each time point for each treatment group were calculated and plotted.

10.3 Results

10.3.1 Bacterial Bioburden of Wounds following treatment

As seen in fig. 10.1, *Staphylococcus aureus* was isolated in all samples, including the negative control. This suggests that normal skin flora is a major issue when creating consistent wounds that can be studied, as the bacterial model used will need to out-complete the resident bacteria. The bacterial model used in this study, *S. epidermidis* does not seem to meet this criteria. While *S. epidermidis* was isolated in samples previously inoculated with the bacteria, they do not appear in significant concentrations, when compared to the *S. aureus*. This calls into doubt if *S. epidermidis* was able to infect the wound, rather than simply colonizing it, especially in the case of the postive control. Therefore, future studies would need to use a more virulent bacteria to ensure proper infection of the wound. Possible bacteria

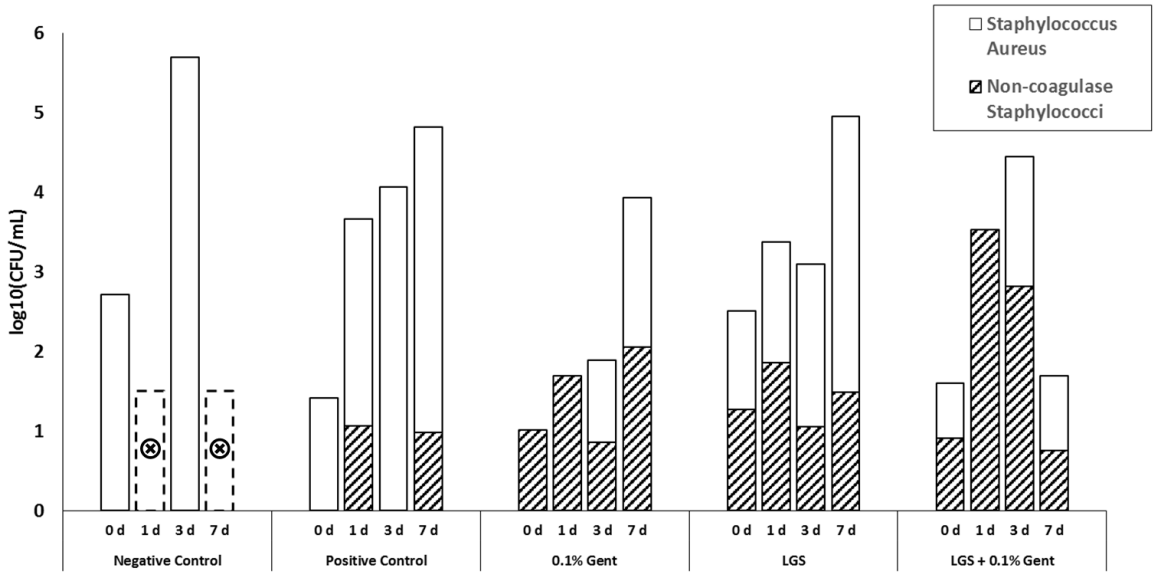

Figure 10.1: Bacterial bioburden of wounds at 0, 1, 3, and 7 d after treatment. Mannitol salt agar was used to quantify bacterial concentration from wound swabs. *Staphylococcus aureus* was seen in all sample groups, while non-coagulase *Staphylococci* was only seen in samples previously inoculated with *Staphylococcus epidermidis*.

for this purpose can be: *Staphylococcus aureus*[102] and *Pseudomonas aeruginosa*[50].

10.3.2 Wound Measurements

As seen in fig. 10.2, the healing rates of each sample group (n=4) were not statistically different from one another. All groups took roughly 9 days to reduce their average wound size by more than 90%. This has two major implications. The first is *S. epidermidis* infected wound model in a rodent is not a good model for studies in infected wounds, as the positive control (no treatment) was not much different than the negative control (no infection). In fact, the positive control healed slightly faster than the negative control. As seen in fig. 10.1, this may be a result of higher colonization of community acquired *S. aureus* in the negative controls than the other samples. The other major implication is that since LGS treated animals were not much different than those that did not receive the LGS treatment, this further supports the hypothesis that the injuries previously seen in animal safety study would not slow wound healing. This further demonstrates the safety of LGS therapy.

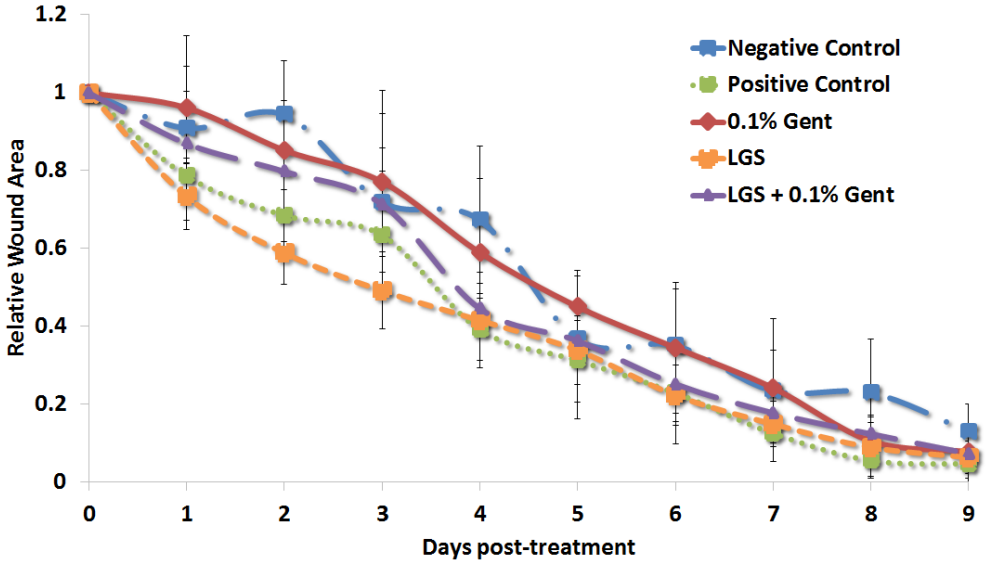

Figure 10.2: Relative area of wounds over the 9 day observation period. All wound areas were normalized to the area measured on 0 d. Each data point has a sample size of 4. All wounds were more than 90% healed after 9 days.

10.4 Discussion

The goal of this preliminary study was to lay the groundwork for future efficacy studies, by striving to answer the following questions: 1. Is *S. epidermidis* a suitable bacterial biofilm model for the investigation of infected wounds and 2. Are pressures generated with a Nd:YAG spot size of 3.0 mm with energy fluence 777.9 mJ safe to use on damaged tissue, as previously hypothesized? As seen in the results, *S. epidermidis* is not a suitable bacterial biofilm model for the investigation of infected wounds. It seems that we have reached the limit for this bacterial model and will need to change the infected wound model in future studies. As mentioned before *Staphylococcus aureus*[102] and *Pseudomonas aeruginosa*[50] are two potential candidates, as they both readily form biofilm and are often found in infected wounds. As for the second question, it appears that the pressures generated with a 3.0 mm spot size and energy fluence 777.9 mJ does not cause significant injuries that impede wound healing. Therefore, these laser parameters would be a good starting place for future efficacy studies. However, it remains to see if this continues to be the case if more LGS therapy is applied more than once. As it may be possible, that the damage can accumulate if more treatments were delivered.

CHAPTER 11

Recommendations for Future Work and Final Conclusions

11.1 Recommendations for Future Work

While we have made significant strides towards the understanding of the effects of LGS therapy and the translation of the technology to pre-clinical, there are still much work that can be done to build upon what was presented here. The most immediate study that can further LGS technology to clinical is to investigate the efficacy of LGS therapy in a more relevant wound model. The minimum would be to use a different bacterial model that can more easily establish an infection than *S. epidermidis*. Two possibilities are the gram positive bacteria: *Staphylococcus aureus* and the gram negative bacteria: *Pseudomonas aeruginosa*. Both readily form biofilms in wounds and have been used for wound studies[103, 104]. However a better study would be one that utilizes a polymicrobial biofilm wound infection model[105], as this better represents the complexity of infections often found in patients. Another area of focus can be in the investigations of the effects of multiple LGS treatments either all at the same time or spaced over the course of the observation period. It is currently unknown, how the effects of LGS against bacteria scales with increased treatments. This would also necessitate further studies into the safety of repeated LGS treatments to determine if tissue can handle repeated and/or sustained LGS treatments.

Since the research on LGS technology, as a treatment methodology for bacterial biofilms, is still relatively unexplored, there is still much basic science that can be done to deepen the understanding of LGS. As biofilms found outside the lab environment are often not growing in static conditions and are rarely composed of single species, a good follow up experiment

would be to grow the biofilm under different conditions and explore if the effects of LGS treatment are different. Another investigation can look into if LGS can improve the efficacy of different classes of antibiotics. The antibiotic used in this study was an aminoglycoside class antibiotic, whose mechanism depends on its ability to penetrate the cell membranes. Therefore a suitable follow up study would be to investigate a class of antibiotics whose mechanism does not depend on its ability to penetrate the cell membrane, such as β-lactams, whom attack the cell walls of the bacteria.

Finally, one improvement for the raster scanning system would be to increase the precision of the system, possibly to micron range. This can be done by the calibration of motor movements, specifically the polynomial curve fits. Despite a lot of care was taken in mounting the mirrors to the mirror mounts and in mounting the camera to the scanning head, there are deviations between the motor axis and the camera axis. In other words, the movements in the beam contributed by the x motor contains both x and y components. Furthermore, the movements of the laser beam by the x motor are not completely orthongonal to the movements contributed by the y motor, once again due to the small inaccuracies when mounting the mirror. Therefore, a better solution would be to create a fitting equation that can take into account of both the x and y movement for each motor. This may be accomplished by using a non-linear optimization fit. However, this is a non-trivial problem, as this optimization fit would have to be done each time when generating a new list of motor positions, which could greatly increase the pre-processing time. Currently, the y axis movement in the x motor and the x axis movement in the y motor are ignored. This can contribute to an error of spot placement by up to 1 mm. However, in return we were able to keep pre-processing time to under a second, as the software only needed to solve a simple polynomial equation for each spot.

11.2 Final Conclusions

The work presented in this thesis sought to 1. determine the efficacy of laser generated shockwave (LGS) therapy against bacterial biofilm and cells and if LGS can be used as an

adjunct therapy with standard antibiotic treatment and 2. translate the LGS technology to pre-clinical by developing a raster scanner for LGS and determining a maximum safety threshold for LGS. In the first aim, we have for the first time demonstrated the efficacy of LGS in the removal of *S. epidermidis* biofilm both *ex vivo* and *in vitro*, a result that standard antibiotic therapy is not able to achieve. We were also able to demonstrate the increase in gentamicin efficacy against *S. epidermidis* biofilm following LGS treatment. In the second aim, we have developed a portable robust raster scanner capable of delivering LGS treatment accurately and in a short time. In doing so, we have overcome one of the major hurdles in bringing LGS technology to clinical, by greatly increasing the size of the treatment area, while maintaining high reliability. Previously, LGS treatments were limited to the size of the spot size, but now we are able to accurately treat an area of $> 2 \times 4\,\mathrm{cm}^2$. We have also demonstrated that LGS to be safe and well tolerated by healthy tissue. This safety is further highlighted by histological data, demonstrating that the shockwaves are limited to the top 2 mm of the tissue, where we expect to find the highest concentration of bacteria in an infection.

The physical nature of LGS therapy is one of its many selling points, as it allows LGS therapy to be non-specific and broad spectrum, a key attribute in treating biofilm infections. As biofilms are often a host to a wide varitey of pathogens[106], whom all can produce different compounds and can show different activities against chemical treatments, biofilms are incredibly heterogeneous between different biofilms and within itself. Therefore, a physical treatment, whose effects does not depend on the type of bacteria present, will have less trouble treating biofilm infections. Further, as its mechanism for LGS is different than antibiotics, LGS may be used as an adjunct therapy to antibiotics.

Finally, LGS therapy is considered to be a low cost methodology for the treatment of bacterial biofilm infections. It does not need a specialized room for treatment or storage and can be wheeled into any clinician's office. Outside of the one time purchase of the system, LGS is very low cost. The only recurring cost would be the ultrasound gel and the LGS substrate, which, at its simplest, is a plastic film with a metallic coating. This, at manufacturing scale, can be made for pennies. Sterilization costs is low, as the disposable

LGS substrate is the only thing that would touch the patient, meaning there would be minimal cleaning required at the end of the procedure. Therefore, LGS has the potential to be a novel, effective, and low cost therapy for the treatment of biofilm infected cutaneous wounds.

References

[1] J W Costerton, K J Cheng, G G Geesey, T I Ladd, J C Nickel, M Dasgupta, and T J Marrie. Bacterial biofilms in nature and disease. *Annual review of microbiology*, 41:435–464, 1987.

[2] P. S. Stewart and J. W. Costerton. Antibiotic resistance of bacteria in biofilms. *Lancet*, 358(9276):135–8, 2001.

[3] Thomas Bjarnsholt. The role of bacterial biofilms in chronic infections. *APMIS. Supplementum*, pages 1–51, May 2013.

[4] Artemio Navarro. Laser-generated shockwaves for the disruption of bacterial biofilms, 2013.

[5] Vidyunmala Ramaprasad, Artemio Navarro, Shahzad Patel, Vikash Patel, Bryan N Nowroozi, Zach D Taylor, William Yong, Vijay Gupta, and Warren S Grundfest. Effect of laser generated shockwaves 1 on ex-vivo pigskin. *Lasers in surgery and medicine*, 46:620–627, October 2014.

[6] JW Costerton, Z Lewandowski, D DeBeer, D Caldwell, D Korber, and G James. Biofilms, the customized microniche. *Journal of bacteriology*, 176(8):2137, 1994.

[7] J William Costerton, Zbigniew Lewandowski, Douglas E Caldwell, Darren R Korber, and Hilary M Lappin-Scott. Microbial biofilms. *Annual Reviews in Microbiology*, 49(1):711–745, 1995.

[8] Mary Ellen Davey and George A O'toole. Microbial biofilms: from ecology to molecular genetics. *Microbiology and molecular biology reviews*, 64(4):847–867, 2000.

[9] Joanna Rayner, Richard Veeh, and Janine Flood. Prevalence of microbial biofilms on selected fresh produce and household surfaces. *International journal of food microbiology*, 95:29–39, August 2004.

[10] I Douterelo, S Husband, V Loza, and J Boxall. Dynamics of biofilm regrowth in drinking water distribution systems. *Applied and environmental microbiology*, 82:4155–4168, July 2016.

[11] Enea Gino Di Domenico, Ilaria Farulla, Grazia Prignano, Maria Teresa Gallo, Matteo Vespaziani, Ilaria Cavallo, Isabella Sperduti, Martina Pontone, Valentina Bordignon, Laura Cilli, Alessandra De Santis, Fabiola Di Salvo, Fulvia Pimpinelli, Ilaria Lesnoni La Parola, Luigi Toma, and Fabrizio Ensoli. Biofilm is a major virulence determinant in bacterial colonization of chronic skin ulcers independently from the multidrug resistant phenotype. *International journal of molecular sciences*, 18, May 2017.

[12] Christine Heilmann, Oliver Schweitzer, Christiane Gerke, Nongnuch Vanittanakom, Dietrich Mack, and Friedrich Götz. Molecular basis of intercellular adhesion in the biofilm-forming staphylococcus epidermidis. *Molecular microbiology*, 20(5):1083–1091, 1996.

[13] Dietrich Mack, Petra Becker, Indranil Chatterjee, Sabine Dobinsky, Johannes K-M Knobloch, Georg Peters, Holger Rohde, and Mathias Herrmann. Mechanisms of biofilm formation in staphylococcus epidermidis and staphylococcus aureus: functional molecules, regulatory circuits, and adaptive responses. *International Journal of Medical Microbiology*, 294(2):203–212, 2004.

[14] A E Khoury, K Lam, B Ellis, and J W Costerton. Prevention and control of bacterial infections associated with medical devices. *ASAIO journal (American Society for Artificial Internal Organs : 1992)*, 38:M174–M178, 1992.

[15] R N Jones. Resistance patterns among nosocomial pathogens: trends over the past few years. *Chest*, 119:397S–404S, February 2001.

[16] Mark E Jones, James A Karlowsky, Deborah C Draghi, Clyde Thornsberry, Daniel F Sahm, and Dilip Nathwani. Epidemiology and antibiotic susceptibility of bacteria causing skin and soft tissue infections in the usa and europe: a guide to appropriate antimicrobial therapy. *International journal of antimicrobial agents*, 22:406–419, October 2003.

[17] Brad Spellberg, Robert Guidos, David Gilbert, John Bradley, Helen W Boucher, W Michael Scheld, John G Bartlett, John Edwards, and Infectious Diseases Society of America. The epidemic of antibiotic-resistant infections: a call to action for the medical community from the infectious diseases society of america. *Clinical infectious diseases : an official publication of the Infectious Diseases Society of America*, 46:155–164, January 2008.

[18] David M Livermore. Introduction: the challenge of multiresistance. *International journal of antimicrobial agents*, 29 Suppl 3:S1–S7, May 2007.

[19] Berenike Maier and Gerard CL Wong. How bacteria use type iv pili machinery on surfaces. *Trends in microbiology*, 23(12):775–788, 2015.

[20] R. H. Eng, F. T. Padberg, S. M. Smith, E. N. Tan, and C. E. Cherubin. Bactericidal effects of antibiotics on slowly growing and nongrowing bacteria. *Antimicrob Agents Chemother*, 35(9):1824–8, 1991.

[21] R R Roth and W D James. Microbiology of the skin: resident flora, ecology, infection. *Journal of the American Academy of Dermatology*, 20:367–390, March 1989.

[22] Keith F Cutting. Wound exudate: composition and functions. *British journal of community nursing*, 8:suppl 4–suppl 9, 2003.

[23] Garth A James, Ellen Swogger, Randall Wolcott, Elinor deLancey Pulcini, Patrick Secor, Jennifer Sestrich, John W Costerton, and Philip S Stewart. Biofilms in chronic wounds. *Wound repair and regeneration : official publication of the Wound Healing Society [and] the European Tissue Repair Society*, 16:37–44, 2008.

[24] J Hurlow and P G Bowler. Potential implications of biofilm in chronic wounds: a case series. *Journal of wound care*, 21:109–10, 112, 114 passim, March 2012.

[25] A I Adler, E J Boyko, J H Ahroni, and D G Smith. Lower-extremity amputation in diabetes. the independent effects of peripheral vascular disease, sensory neuropathy, and foot ulcers. *Diabetes care*, 22:1029–1035, July 1999.

[26] M. A. Fonder, G. S. Lazarus, D. A. Cowan, B. Aronson-Cook, A. R. Kohli, and A. J. Mamelak. Treating the chronic wound: A practical approach to the care of nonhealing wounds and wound care dressings. *J Am Acad Dermatol*, 58(2):185–206, 2008.

[27] Sara E Cosgrove. The relationship between antimicrobial resistance and patient outcomes: mortality, length of hospital stay, and health care costs. *Clinical infectious diseases : an official publication of the Infectious Diseases Society of America*, 42 Suppl 2:S82–S89, January 2006.

[28] J.H. Merritt, D. E. Kadouri, and G. A. O'Toole. Wound care market by type (traditional (wound closure, anti infective), basic (films, cleansing), advanced (hydrogels, hydrocolloids, alginate, collagen), active (artificial skin & skin substitutes), pressure relief devices, npwt). Report MD 2611, Markets and Markets, 2014.

[29] Markets for advanced wound management technologies. Serial, Wellesley, MA, 2014.

[30] Thien-Fah Mah. Biofilm-specific antibiotic resistance. *Future microbiology*, 7:1061–1072, September 2012.

[31] Clayton W Hall and Thien-Fah Mah. Molecular mechanisms of biofilm-based antibiotic resistance and tolerance in pathogenic bacteria. *FEMS microbiology reviews*, 41:276–301, May 2017.

[32] Heesemann J. [mechanisms of resistance to beta-lactam antibiotics]. *Infection*, 1993.

[33] Rachel J Gordon, Maria Miragaia, Alan D Weinberg, Caroline J Lee, Joana Rolo, Julie C Giacalone, Mark S Slaughter, Pat Pappas, Yoshifumi Naka, Alfred J Tector, Herminia de Lencastre, and Franklin D Lowy. Staphylococcus epidermidis colonization is highly clonal across us cardiac centers. *The Journal of infectious diseases*, 205:1391–1398, May 2012.

[34] Curtis E Jones and John P Kennedy. Treatment options to manage wound biofilm. *Advances in wound care*, 1:120–126, June 2012.

[35] Rebecca S Howell-Jones, Patricia E Price, Anthony J Howard, and David W Thomas. Antibiotic prescribing for chronic skin wounds in primary care. *Wound repair and regeneration : official publication of the Wound Healing Society [and] the European Tissue Repair Society*, 14:387–393, 2006.

[36] R S Howell-Jones, M J Wilson, K E Hill, A J Howard, P E Price, and D W Thomas. A review of the microbiology, antibiotic usage and resistance in chronic skin wounds. *The Journal of antimicrobial chemotherapy*, 55:143–149, February 2005.

[37] Jack Norman Pendleton and Brendan F Gilmore. The antimicrobial potential of ionic liquids: A source of chemical diversity for infection and biofilm control. *International journal of antimicrobial agents*, 46:131–139, August 2015.

[38] Gilles Brackman, Ulrik Hillaert, Serge Van Calenbergh, Hans J Nelis, and Tom Coenye. Use of quorum sensing inhibitors to interfere with biofilm formation and development in burkholderia multivorans and burkholderia cenocepacia. *Research in microbiology*, 160:144–151, March 2009.

[39] Gilles Brackman and Tom Coenye. Quorum sensing inhibitors as anti-biofilm agents. *Current pharmaceutical design*, 21:5–11, 2015.

[40] J G Dahlgren, E T Anderson, and W L Hewitt. Gentamicin blood levels: a guide to nephrotoxicity. *Antimicrobial agents and chemotherapy*, 8:58–62, July 1975.

[41] G Stringel, R Bawdon, M Savrich, L Guertin, and J Horton. Topical and systemic antibiotics in the prevention of wound infection. *Journal of pediatric surgery*, 24:1003–1006, October 1989.

[42] Ellappan Kalaiarasan, Kottha Thirumalaswamy, Belgode Narasimha Harish, Vasuki Gnanasambandam, Veeresh Kumar Sali, and James John. Inhibition of quorum sensing-controlled biofilm formation in pseudomonas aeruginosa by quorum-sensing inhibitors. *Microbial pathogenesis*, 111:99–107, October 2017.

[43] M Dyson. Non-thermal cellular effects of ultrasound. *The British journal of cancer. Supplement*, 5:165–171, March 1982.

[44] S.R. Young and M. Dyson. The effect of therapeutic ultrasound on angiogenesis. *Ultrasound in Medicine & Biology*, 16(3):261–269, jan 1990.

[45] M C Fyfe and L A Chahl. Mast cell degranulation and increased vascular permeability induced by 'therapeutic' ultrasound in the rat ankle joint. *British journal of experimental pathology*, 65:671–676, December 1984.

[46] N N Byl, A L McKenzie, J M West, J D Whitney, T K Hunt, and H A Scheuenstuhl. Low-dose ultrasound effects on wound healing: a controlled study with yucatan pigs. *Archives of physical medicine and rehabilitation*, 73:656–664, July 1992.

[47] Nancy N. Byl, Alison McKenzie, Theresa Wong, Judith West, and Thomas K. Hunt. Incisional wound healing: A controlled study of low and high dose ultrasound. *Journal of Orthopaedic & Sports Physical Therapy*, 18(5):619–628, nov 1993.

[48] A M Rediske, B L Roeder, J L Nelson, R L Robison, G B Schaalje, R A Robison, and W G Pitt. Pulsed ultrasound enhances the killing of escherichia coli biofilms by aminoglycoside antibiotics in vivo. *Antimicrobial agents and chemotherapy*, 44:771–772, March 2000.

[49] W.G. Pitt and S.A. Ross. Ultrasound increases the rate of bacterial cell growth. *Biotechnology Progress*, 19(3):1038–1044, jun 2003.

[50] Keith H Turner, Jake Everett, Urvish Trivedi, Kendra P Rumbaugh, and Marvin Whiteley. Requirements for pseudomonas aeruginosa acute burn and chronic surgical wound infection. *PLoS genetics*, 10:e1004518, July 2014.

[51] Philipp Mller, Bernhard Guggenheim, Thomas Attin, Ernst Marlinghaus, and Patrick R Schmidlin. Potential of shock waves to remove calculus and biofilm. *Clinical oral investigations*, 15:959–965, December 2011.

[52] Xiaojie Li, Mengshi Chen, Lei Li, Hai Qing, and Zhimin Zhu. Extracorporeal shock wave therapy: a potential adjuvant treatment for peri-implantitis. *Medical hypotheses*, 74:120–122, January 2010.

[53] Mustafa Erkan Inanmaz, Mustafa Uslu, Cengiz Isik, Ertugrul Kaya, Tekin Tas, and Recep Bayram. Extracorporeal shockwave increases the effectiveness of systemic antibiotic treatment in implant-related chronic osteomyelitis: Experimental study in a rat model. *Journal of Orthopaedic Research*, 32(6):752–756, feb 2014.

[54] Andrew J. Coleman, John E. Saunders, Lawrence A. Crum, and Mary Dyson. Acoustic cavitation generated by an extracorporeal shockwave lithotripter. *Ultrasound in Medicine & Biology*, 13(2):69–76, feb 1987.

[55] Ilhan Gecit, Servet Kavak, Elif Kaval Oguz, Necip Pirincci, Mustafa Gnes, Mikail Kara, Kadir Ceylan, Mehmet Kaba, and Serhat Tank. Tissue damage in kidney, adrenal glands and diaphragm following extracorporeal shock wave lithotripsy. *Toxicology and industrial health*, 30:845–850, October 2014.

[56] James A. McAteer and Andrew P. Evan. The acute and long-term adverse effects of shock wave lithotripsy. *Seminars in Nephrology*, 28(2):200–213, mar 2008.

[57] Janet Ramundo and Mikel Gray. Enzymatic wound debridement. *Journal of Wound, Ostomy and Continence Nursing*, 35(3):273–280, may 2008.

[58] M. Knig, W. Vanscheidt, M. Augustin, and H. Kapp. Enzymatic versus autolytic debridement of chronic leg ulcers: a prospective randomised trial. *Journal of Wound Care*, 14(7):320–323, jul 2005.

[59] M Cambal, P Labas, M Kozanek, P Takac, and Z Krumpalova. Maggot debridement therapy. *Bratislavske lekarske listy*, 107:442–444, 2006.

[60] Philip G Bowler. Wound pathophysiology, infection and therapeutic options. *Annals of medicine*, 34:419–427, 2002.

[61] Simona Vittorini and Simona Storti. *Molecular Medicine*, 13(1-2):1, 2007.

[62] A S Halim, T L Khoo, and A Z Mat Saad. Wound bed preparation from a clinical perspective. *Indian journal of plastic surgery : official publication of the Association of Plastic Surgeons of India*, 45:193–202, May 2012.

[63] L G Ovington. Hanging wet-to-dry dressings out to dry. *Home healthcare nurse*, 19:477–83; quiz 484, August 2001.

[64] Thomas and Stephen Thomas. *Wound Management and Dressings*. Pharmaceutical Press, 1990.

[65] B. R. Matlaga, J. A. McAteer, B. A. Connors, R. K. Handa, A. P. Evan, J. C. Williams, J. E. Lingeman, and L. R. Willis. Potential for cavitation-mediated tissue damage in shockwave lithotripsy. *J Endourol*, 22(1):121–6, 2008.

[66] A. P. Evan, L. R. Willis, J. E. Lingeman, and J. A. McAteer. Renal trauma and the risk of long-term complications in shock wave lithotripsy. *Nephron*, 78(1):1–8, 1998.

[67] J. Yuan and V. Gupta. Measurement of interface strength by the modified laser spallation technique. i. experiment and simulation of the spallation process. *Journal of Applied Physics*, 74(4):2388–2396, aug 1993.

[68] V. Gupta, A.S. Argon, D.M. Parks, and J.A. Cornie. Measurement of interface strength by a laser spallation technique. *Journal of the Mechanics and Physics of Solids*, 40(1):141–180, jan 1992.

[69] Vijay Gupta, Vassili Kireev, Jun Tian, Hiroshi Yoshida, and Haruo Akahoshi. Glass-modified stress waves for adhesion measurement of ultra thin films for device applications. *Journal of the Mechanics and Physics of Solids*, 51(8):1395–1412, aug 2003.

[70] V. Gupta and J. Yuan. Measurement of interface strength by the modified laser spallation technique. II. applications to metal/ceramic interfaces. *Journal of Applied Physics*, 74(4):2397–2404, aug 1993.

[71] J. Yuan, V. Gupta, and A. Pronin. Measurement of interface strength by the modified laser spallation technique. III. experimental optimization of the stress pulse. *Journal of Applied Physics*, 74(4):2405–2410, aug 1993.

[72] G. R. Nigri, S. Tsai, S. Kossodo, P. Waterman, P. Fungaloi, D. C. Hooper, A. G. Doukas, and G. M. LaMuraglia. Laser-induced shock waves enhance sterilization of infected vascular prosthetic grafts. *Lasers Surg Med*, 29(5):448–54, 2001.

[73] Y. P. Krespi, P. Stoodley, and L. Hall-Stoodley. Laser disruption of biofilm. *Laryngoscope*, 118(7):1168–73, 2008.

[74] Z. D. Taylor, A. Navarro, C. P. Kealey, D. Beenhouwer, D. A. Haake, W. S. Grundfest, and V. Gupta. Bacterial biofilm disruption using laser generated shockwaves. In *Engineering in Medicine and Biology Society (EMBC), 2010 Annual International Conference of the IEEE*, pages 1028–1032, 2010.

[75] Artemio Navarro, Zachary D. Taylor, Anthony Z. Matolek, Ahuva Weltman, Vidyunmala Ramaprasad, Sean Huang, David O. Beenhouwer, David A. Haake, Vijay Gupta, and Warren S. Grundfest. Bacterial biofilm disruption using laser-generated shockwaves. In *Infect Drug Resist*, volume 8214, pages 82141H–82141H–8, 2010. 10.1117/12.908661.

[76] N. C. Francis, I. Kassam, B. Nowroozi, W. S. Grundfest, and Z. D. Taylor. Analysis of flexible substrates for clinical translation of laser-generated shockwave therapy. *Biomed Opt Express*, 6(3):827–37, 2015.

[77] Eric Birkenhauer, Suresh Neethirajan, and J Scott Weese. Collagen and hyaluronan at wound sites influence early polymicrobial biofilm adhesive events. *BMC microbiology*, 14:191, July 2014.

[78] Sabine Debeer, Jean-Benot Le Luduec, Dominique Kaiserlian, Philippe Laurent, Jean-Franois Nicolas, Bertrand Dubois, and Jean Kanitakis. Comparative histology and immunohistochemistry of porcine versus human skin. *European journal of dermatology : EJD*, 23:456–466, 2013.

[79] N. C. Francis, W. Yao, W. S. Grundfest, and Z. D. Taylor. Laser-generated shockwaves as a treatment to reduce bacterial load and disrupt biofilm. *IEEE Trans Biomed Eng*, 2016.

[80] Brian M Peters, Mary Ann Jabra-Rizk, Graeme A O'May, J William Costerton, and Mark E Shirtliff. Polymicrobial interactions: impact on pathogenesis and human disease. *Clinical microbiology reviews*, 25:193–213, January 2012.

[81] 5704 series stepper motor — nema 23 — 0.45 — lin engineering, 2017.

[82] Broadband dielectric mirrors, 2017.

[83] B. F. Farber, M. H. Kaplan, and A. G. Clogston. Staphylococcus epidermidis extracted slime inhibits the antimicrobial action of glycopeptide antibiotics. *J Infect Dis*, 161(1):37–40, 1990.

[84] J G Dahlgren, E T Anderson, and W L Hewitt. Gentamicin blood levels: a guide to nephrotoxicity. *Antimicrobial agents and chemotherapy*, 8:58–62, July 1975.

[85] S H Powell, W L Thompson, M A Luthe, R C Stern, D A Grossniklaus, D D Bloxham, D L Groden, M R Jacobs, A O DiScenna, H A Cash, and J D Klinger. Once-daily vs. continuous aminoglycoside dosing: efficacy and toxicity in animal and clinical studies of gentamicin, netilmicin, and tobramycin. *The Journal of infectious diseases*, 147:918–932, May 1983.

[86] Gentamicin sulfate information from drugs.com, 2017.

[87] Garry Laverty, Mahmoud Y. Alkawareek, and Brendan F. Gilmore. The in vitro susceptibility of biofilm forming medical device related pathogens to conventional antibiotics. *Dataset Papers in Science*, 2014:10, 2014.

[88] D. Bakkiyaraj and S. K. Pandian. In vitro and in vivo antibiofilm activity of a coral associated actinomycete against drug resistant staphylococcus aureus biofilms. *Biofouling*, 26(6):711–7, 2010.

[89] J. H. Merritt, D. E. Kadouri, and G. A. O'Toole. Growing and analyzing static biofilms. *Curr Protoc Microbiol*, Chapter 1:Unit 1B 1, 2005.

[90] A. A. Miles, S. S. Misra, and J. O. Irwin. The estimation of the bactericidal power of the blood. *J Hyg (Lond)*, 38(6):732–49, 1938.

[91] J. Curtin, M. Cormican, G. Fleming, J. Keelehan, and E. Colleran. Linezolid compared with eperezolid, vancomycin, and gentamicin in an in vitro model of antimicrobial lock therapy for staphylococcus epidermidis central venous catheter-related biofilm infections. *Antimicrob Agents Chemother*, 47(10):3145–8, 2003.

[92] Ernest L Madsen, Maritza A Hobson, Hairong Shi, Tomy Varghese, and Gary R Frank. Tissue-mimicking agar/gelatin materials for use in heterogeneous elastography phantoms. *Physics in medicine and biology*, 50:5597–5618, December 2005.

[93] Adrian F Prokop, Shahram Vaezy, Misty L Noble, Peter J Kaczkowski, Roy W Martin, and Lawrence A Crum. Polyacrylamide gel as an acoustic coupling medium for focused ultrasound therapy. *Ultrasound in medicine & biology*, 29:1351–1358, September 2003.

[94] Nicholas J Dudley, Nicholas M Gibson, Mark J Fleckney, and Peter D Clark. The effect of speed of sound in ultrasound test objects on lateral resolution. *Ultrasound in medicine & biology*, 28:1561–1564, 2002.

[95] Rok Hrovatin and Janez Možina. Effect of plasma shielding in laser ultrasonics: Optoacoustic characterization. *Journal of applied physics*, 75(12):8207–8209, 1994.

[96] JM Vadillo, JM Fernandez Romero, C Rodriguez, and JJ Laserna. Effect of plasma shielding on laser ablation rate of pure metals at reduced pressure. *Surface and interface analysis*, 27(11):1009–1015, 1999.

[97] Raffi Karshafian, Peter D. Bevan, Ross Williams, Sanya Samac, and Peter N. Burns. Sonoporation by ultrasound-activated microbubble contrast agents: Effect of acoustic exposure parameters on cell membrane permeability and cell viability. *Ultrasound in Medicine & Biology*, 35(5):847–860, may 2009.

[98] H R Guzmn, D X Nguyen, S Khan, and M R Prausnitz. Ultrasound-mediated disruption of cell membranes. i. quantification of molecular uptake and cell viability. *The Journal of the Acoustical Society of America*, 110:588–596, July 2001.

[99] H R Guzmn, D X Nguyen, S Khan, and M R Prausnitz. Ultrasound-mediated disruption of cell membranes. ii. heterogeneous effects on cells. *The Journal of the Acoustical Society of America*, 110:597–606, July 2001.

[100] Molecular Probes. *LIVE/DEAD® BacLight™Bacterial Viability and Counting Kit (L34856)*, 2004.

[101] S Lee, N Kollias, D J McAuliffe, T J Flotte, and A G Doukas. Topical drug delivery in humans with a single photomechanical wave. *Pharmaceutical research*, 16:1717–1721, November 1999.

[102] E. Kugelberg, T. Norstrom, T. K. Petersen, T. Duvold, D. I. Andersson, and D. Hughes. Establishment of a superficial skin infection model in mice by using staphylococcus aureus and streptococcus pyogenes. *Antimicrobial Agents and Chemotherapy*, 49(8):3435–3441, jul 2005.

[103] Clark F. Schierle, Mauricio De la Garza, Thomas A. Mustoe, and Robert D. Galiano. Staphylococcal biofilms impair wound healing by delaying reepithelialization in a murine cutaneous wound model. *Wound Repair and Regeneration*, 17(3):354–359, may 2009.

[104] Somprakas Basu, Manav Agarwal, Satyanam Kumar Bhartiya, Gopal Nath, and Vijay Kumar Shukla. An in vivo wound model utilizing bacteriophage therapy of pseudomonas aeruginosa biofilms. *Ostomy/wound management*, 61:16–23, August 2015.

[105] Trevor Dalton, Scot E. Dowd, Randall D. Wolcott, Yan Sun, Chase Watters, John A. Griswold, and Kendra P. Rumbaugh. An in vivo polymicrobial biofilm wound infection model to study interspecies interactions. *PLoS ONE*, 6(11):e27317, nov 2011.

[106] Scot E. Dowd, Randall D. Wolcott, Yan Sun, Trevor McKeehan, Ethan Smith, and Daniel Rhoads. Polymicrobial nature of chronic diabetic foot ulcer biofilm infections determined using bacterial tag encoded FLX amplicon pyrosequencing (bTEFAP). *PLoS ONE*, 3(10):e3326, oct 2008.